DEVELOPMENT OF HIGH CONTRAST COHERENT ANTI-STOKES RAMAN SCATTERING (CARS) AND MULTIPHOTON MICROSCOPY FOR LABEL-FREE BIOMOLECULAR IMAGING

LU FAKE

NATIONAL UNIVERSITY OF SINGAPORE

2010

DEVELOPMENT OF HIGH CONTRAST COHERENT ANTI-STOKES RAMAN SCATTERING (CARS) AND MULTIPHOTON MICROSCOPY FOR LABEL-FREE BIOMOLECULAR IMAGING **LU FAKE** **2010**

DEVELOPMENT OF HIGH CONTRAST COHERENT ANTI-STOKES RAMAN SCATTERING (CARS) AND MULTIPHOTON MICROSCOPY FOR LABEL-FREE BIOMOLECULAR IMAGING

LU FAKE

A THESIS SUBMITTED

FOR THE DEGREE OF DOCTOR OF PHILOSOPHY

DIVISION OF BIOENGINEERING

NATIONAL UNIVERSITY OF SINGAPORE

2010

Acknowledgements

The work presented in this thesis was primarily conducted in Optical Bioimaging Laboratory in the Division of Bioengineering at the National University of Singapore during the period from January 2006 to January 2010. In the past four years, I met many nice people who gave me big encouragement and kindly help. Here I would like to thank them sincerely:

First and foremost, I would like to express my sincere appreciation to my advisor Assistant Professor Huang Zhiwei, who offered me the opportunity in the very beginning to pursue the PhD degree in his group. I am indebted to Dr Huang for his professional advice, guidance, and patience throughout my studies. His fully financial support on my experiments boosted the overall progress greatly. I believe and appreciate that Prof Huang has an extraordinary impact on my future research career.

I greatly appreciate the generous support and guidance from Professor Colin Sheppard, who is a very nice person as a great scientist in Optics. His equations and scientific discussions gave me deep impression and positive affection. I would like to thank Assistant Professor Chen Nanguang, who helped me a lot throughout my studentship. Great appreciation and respect to Professor Dietmar W. Hutmacher and Professor Hanry Yu and their group members, who taught me useful knowledge on biology and biomedicine research and offered me cellular and tissue samples for my study.

I would also like to acknowledge my coworkers and team members in Optical Bioimaging Laboratory: Dr Zheng Wei, Dr Liu Cheng, Dr Yuen Clement, Dr Yew Yan Seng Elijah, Mo Jianhua, Teh Seng Knoon, Shao Xiaozhuo, Lin Kan, Lin Jian for their kind discussions, suggestions and guidance on my research work.

I wish to thank my dear parents, darling wife, close brother and all my lovely classmates and friends, with whom I kept walking through these hardworking days.

Last but not least, I would like to acknowledge the financial support from the Ministry of Education of Singapore, the President Graduate Fellowship (PGF) of National University of Singapore (NUS) for my research at NUS.

Table of Contents

Abstract

Coherent anti-Stokes Raman scattering (CARS) microscopy has received much interest for imaging cells and tissues due to its outstanding capabilities of biochemical selectivity using molecular vibrations, high sensitivity, as well as intrinsic three-dimensional optical sectioning ability. In this thesis, the polarization effects in CARS microscopy have been comprehensively studied and thereby several novel CARS microscopic techniques for high contrast vibrational imaging and high sensitive molecular orientation detection have been reported. An advanced interferometric polarization CARS imaging technique was developed to effectively suppress the nonresonant background, while greatly enhance the weak resonant signals of low concentration biochemicals for high contrast and high sensitive biomolecular imaging. To further reduce the excitation power for minimizing the photodamage to the specimens, a unique heterodyne-detected polarization CARS technique by utilizing interference of the relatively intense local oscillator CARS signal and the weak resonant CARS signal generated simultaneously within the focal volume of the sample was also developed for high sensitive CARS imaging. In addition, employing an elliptically polarized pump field combined with a linearly polarized Stokes field, intrinsic background-free CARS imaging was realized with much higher resonant signal intensities to be detected as compared to conventional polarization CARS. To facilitate the three dimensional molecular orientation sensing, a radial polarization CARS microscope was demonstrated for improving the detection of longitudinally oriented molecules in the samples. Further, an integrated CARS and multiphoton microscopy technique by implementing a dual 4-f configured paired-gratings spectral filtering module on a dual-color femtosecond laser source has also been successfully developed for biomolecular imaging. It was demonstrated that high contrast CARS and high quality multiphoton microscopy imaging could be acquired in tandem on the same platform for quantitative assessment of biomolecular changes associated with liver disease transformations (e.g., fatty/fibrotic liver). This research indicated the great applicable potential of the integrated CARS microscopy and multiphoton microscopy for label-free biomolecular imaging in biological and biomedical systems.

List of Figures

List of Abbreviations

BDL	=	Bile duct ligation
CARS	=	Coherent anti-Stokes Raman scattering
C-CARS	=	Counter propagation CARS
DIC	=	Differential inference contrast
E-CARS	=	Epi-detected CARS
EP-CARS	=	Elliptically polarized CARS
F-CARS	=	Forward-detected CARS
FDTD	=	Finite-difference time-domain
FWHM	=	Full width at half maximum
fs	=	Femtosecond
HP-CARS	=	Heterodyne polarization CARS
IP-CARS	=	Interferometric polarization CARS
LP-CARS	=	Linearly polarized CARS
M-CARS	=	Multiplex CARS
NLO	=	Nonlinear optics
NA	=	Numerical aperture
NAFLD	=	Nonalcoholic fatty liver disease
NIR	=	Near infrared
OCT	=	Optical coherent tomography
OPO	=	Optical parametric oscillator
PCF	=	Photonics crystal fiber
ps	=	Picosecond
P-CARS	=	Polarization CARS
PMT	=	Photomultiplier tube
RP-CARS	=	Radially polarized CARS
SERS	=	Surface enhanced Raman scattering
SHG	=	Second harmonic generation
SFG	=	Sum frequency generation
THG	=	Third harmonic generation
TPEF	=	Two photon excited fluorescence

Chapter 1 Introduction

1.1 Background

Laser-scanning confocal fluorescence microscopy has been widely used in material and life sciences for submicron level investigations through a fast imaging approach, allowing the specific visualization of microscopic structures of the stained molecular composition with both chemical specificity and three-dimensional sectioning capability [1]. However, for biomolecular species and cellular components that cannot tolerate fluorescence staining, other complementary contrast mechanisms with noninvasive characterization are needed. Phase contrast and differential interference contrast (DIC) microscopy [2, 3] rely on the minor differences of the refractive index across the label-free sample to highlight the small particles and interfaces with index mismatch. From this view, both of them are index-sensitive, not chemical-selective. Vibrational microscopies, such as infrared spectroscopy and Raman spectroscopy [4-6], have been used for chemically-selective imaging. Unfortunately, infrared absorption microscopy suffers from low spatial resolution due to the long excitation wavelength (diffraction limitation), while the sensitivity of Raman spectroscopy is limited by the inherently very weak Raman scattering mixed with the strong fluorescence background. Surface enhanced Raman scattering (SERS) detection schemes can be sensitive enough for single molecule detection, due to the enhancement of Raman scattering by molecules attached on rough metal surfaces, but the additional requirement of a tedious preparation of substrates with nano-level metal structures makes it hard to be used for most biological applications in vivo [7].

The technical achievements on femtosecond or picosecond pulsed laser sources triggered the rapid development of nonlinear optical (NLO) microscopy for life science applications [8]. The most commonly used and well developed nonlinear modalities include two-photon excitation fluorescence (TPEF) [9-11], second harmonic generation (SHG) [12-14], and third harmonic generation (THG) [15, 16]. The label-free biological application of TPEF imaging is hindered by the limited endogenous fluorophores, while exogenous labeling also suffers from the drawback that staining may alter the physiological environment of the biological/biomedical systems. SHG imaging requires the local break of inversion symmetry in the molecules and is only sensitive to few biochemicals, such as collagens. THG can work based on the differences of third-order nonlinear susceptibility or refractive index, both of which are nonresonant processes.

Recently, coherent anti-Stokes Raman scattering (CARS) imaging has been developed as a useful complementary technique for video-rate vibrational imaging based on the coherently enhanced Raman-active vibrations [17-19]. CARS as a typical third-order nonlinear process, was first reported in 1965 by Maker and Terhune at the Ford Motor Company [20]. Thereafter CARS spectroscopy has been widely used as a viable means for chemical analysis in both gas and liquids [21-23]. In 1982, Ducan et al. reported the first CARS microscope using a non-collinear configuration of pump and Stokes beams to image onion cells with chemical specificity [24]. In that experiment, the visible light excitation resulted in relatively larger nonresonant background due to two-photon electronic resonance. On the other hand, the

non-collinear excitation geometry lowered down the spatial resolution and also made the system unsuitable for microscopy applications. Until 1999, Zumbusch et al. demonstrated the first CARS microscopy with collinear beam geometry for unstained live bacteria and cell imaging [18]. Soon after, it was proved that in CARS microscopy the interaction length is only several micrometers or less under tightly focusing condition using large NA microscope objectives, thus the phase-mismatching condition can be relaxed within the large cone angle with collinear beam geometry. Collinear beam geometry is considered to be the key simplification strategy on CARS implementation for its successful revival in the last decade [25].

The advantages of CARS microscopy has been concluded as follows [26-28]: (i) Natural or artificial fluorescence probes are usually unnecessary in CARS imaging, since its contrast mechanism is based on molecular vibrations that are intrinsic to the samples. (ii) CARS signal is orders of magnitude more sensitive than Raman signal, which yields much higher sensitivity with relatively lower average excitation power. (iii) The third-order nonlinear signal generation dependence leads to inherent 3D sectioning capability. (iv) CARS signal is blue-shifted from both pump and Stokes frequencies, and can thus be easily detected avoiding the fluorescence background. (v) The use of near-infrared (NIR) wavelength excitation minimizes the photodamage (mainly water absorption) to the sample and also provides a large penetration depth for thick samples or tissues. However, despite all its advantages, one major drawback of CARS microscopy is the existence of the nonresonant background due to the electronic contributions to the third-order nonlinear susceptibility from both the sample and the

solvent environment, which is independent of the resonant Raman scattering [23, 29]. The nonresonant background seriously destroys the vibrational contrast and sometimes even overwhelms the weak resonant signals. Various methods have been developed for suppression of the nonresonant background to improve the detection sensitivity and spectral specificity in CARS imaging. These works will be comprehensively reviewed in Chapter 2.

1.2 Motivations

The motivations of the study in this thesis are summarized as follows:

1) Although many techniques have been developed to suppress the nonresonant background for high contrast CARS imaging, these methods either make the system too complex or attenuate the resonant CARS signals seriously, limiting the wide applications of CARS microscopy for imaging of low-concentration biocompounds. It is highly desirable to develop robust and easy-to-operate CARS microscopic techniques with high vibrational contrast for biological and biomedical applications.

2) CARS radiation shows strong polarization sensitivity depending on both the polarization direction of excitation (pump and Stokes) beams and the orientation of the molecules under investigation. Polarization-sensitive CARS imaging has been demonstrated. However, the comprehensive mechanism and its applicable potential of polarization-encoded techniques for high sensitive CARS imaging, such as elliptical polarization and radial polarization, has not been fully understood.

3) Femtosecond (fs) pulse lasers have been widely used for multiphoton microscopy. In contrast, picosecond (ps) pulse lasers are ideal for CARS imaging. In a multimodal nonlinear optical (NLO) microscopy integrating CARS, TPEF, SHG, THG, or SFG, both fs and ps laser sources are involved to make the technique very costly and inconvenient for operation, especially in biological laboratories. To facilitate the applications of multimodal NLO microscopy in biological and biomedical systems, it is very necessary to simplify the technique by only employing one fs laser source, while still being accessible to different nonlinear optical microscopy imaging modalities for tissue imaging.

4) For liver disease diagnosis, the current available noninvasive tests lack sensitivity and specificity and have limited utility in general. They are far not enough for acute disease staging or grading for the establishment of a stable scoring system. Thus, liver biopsy remains the only reliable way for screening and diagnosing of liver diseases. There is an urgent need to develop and validate simple, reproducible, noninvasive tools that accurately distinguish NASH from NAFLD and determine the stage or grade of the diseases. Multimodal nonlinear optical microscopy modality provides label-free imaging and quantitative assessment of different biochemical compounds in tissue samples. It could be a very powerful tool for liver disease (fibrosis and steatosis) diagnosis, especially for early stage detection. Moreover, recent study has shown that liver fibrosis or even cirrhosis is reversible, indicating that early disease diagnosis would be very important from the clinical view.

1.3 Research Objectives

The main aims of this research are (1) to study the polarization effects in CARS and investigate their applications for effective suppression of the nonresonant background and facilitation of molecular orientation sensing, and (2) to establish a fs/ps swappable multimodal nonlinear optical microscopy platform for high sensitive label-free liver disease diagnosis at tissue level.

The specific objectives of this research are as follows:

1) To develop a novel interferometric polarization CARS (IP-CARS) imaging technique to effectively suppress the nonresonant background, while greatly enhance the weak resonant signals from low concentration biochemicals for high contrast and high sensitive CARS imaging.
2) To propose a phase-controlled polarization CARS approach to avoid the use of fast phase modulation for heterodyne detection in IP-CRAS by direct subtraction between in-phase and out-of-phase images, providing a simple method to realize background-free CARS imaging.
3) To propose a simplified heterodyne polarization (HP-) CARS scheme only using single pump-Stokes beam to further reduce the excitation power for minimal photodamage to the specimens, which utilizes interference of the relatively intense idle CARS signal and the weak resonant CARS signal generated simultaneously within the focal volume of the sample of conventional P-CARS for heterodyne detection.

4) To explore the unique polarization effects in CARS with elliptically polarized light and develop its potential application for intrinsic background-free CARS imaging for the first time.

5) To investigate CARS microscopy with radial polarization illumination, a novel annular aperture detection scheme was proposed in radially polarized (RP-) CARS to significantly remove the nonresonant background for high contrast vibrational imaging through finite-difference time-domain (FDTD) simulations. On the other hand, since tightly focusing of radially polarized light generates strong longitudinal electric fields within the focal volume, it would be interesting to investigate experimentally RP-CARS imaging for facilitating longitudinally oriented molecule detections and sensing.

6) To apply a unique implementation of a dual 4-f configured paired-gratings spectral filtering of a femtosecond (fs) laser source to realize high contrast CARS and high quality multiphoton microscopy on the same platform for label-free biomolecular imaging through in tandem swapping the 4-f grating filtering between the ps mode and fs mode.

7) To apply the integrated CARS and multiphoton imaging system for qualitative and quantitative assessment of hepatic fats, aggregated collagens and hepatocyte morphology in diseased liver tissues induced by bile duct ligation (BDL) in a rat model.

1.4 Thesis Organization

The thesis is organized as follows: Chapter 1 introduces the background, motivations

and research objectives of this thesis. Chapter 2 firstly generalizes the fundamental theory and instrumentation for CARS microscopy, and then reviews the major technical aspects for suppression of the nonresonant background in CARS, followed by reviewing the biological and biomedical applications of CARS imaging. Finally, a brief review about liver steatosis and liver fibrosis diseases and their diagnosis approaches is presented. Chapter 3 reports on the development of polarization-encoded techniques in CARS for high contrast and high sensitive cellular imaging. In Chapter 4, CARS microscopy using radially polarized (RP-) light illumination is reported, and the potential using RP-CARS microscopy for high sensitive molecular orientations sensing is discussed and demonstrated. Chapter 5 presents the development of an integrated CARS and multiphoton microscopy platform and its application for quantitative assessment of fibrotic liver tissue samples for the purpose of liver disease diagnosis. Final conclusions and future directions are summarized in Chapter 6.

Chapter 2 Literature Review

2.1 Basic Theory

2.1.1 Rationale of Raman spectroscopy

Raman scattering is an inelastic scattering process of incident light photons interacting with materials. It was first discovered by C. V. Raman in 1928 [30]. The classical theory of light scattering from molecules describes the electric field of the scattered radiation, E_{sc}, as the result of an oscillating dipole induced on the molecule by the presence of an incident field, E_{in}. The dipole moment, μ, can be generally described by the following equation [31],

$$\mu(t) = \alpha(t)E_{in}(t), \tag{2.1}$$

where $\alpha(t)$ is the polarizability tensor with time-dependence. Because there are beat patterns between E_{in} and α, μ will contain a number of frequency components. The component of μ at v_{sc}=v_{in}, which is responsible for Rayleigh scattering, corresponding to the linear component (elastic) of the polarizability tensor. On the other hand, Raman scattering is due to the nonlinear harmonic terms (inelastic) in the molecule's polarizability.

Another theoretical explanation for light scattering is semi-phenomenological quantum mechanics, in which the incident electric field is treated as a perturbation to the eigenstates of a molecule, producing time-dependent virtual states as shown in Fig. 2.1 [31]. Since Raman scattering results from a transition between two stationary states of the molecules, the difference in energy between the vibrational levels is carried off

by the scattered photons, and the frequency shift can be observed. Using perturbation theory and the time-dependent Schrödinger equation, it is predicted that Raman scattering is weaker than Rayleigh scattering by about three orders of magnitude. In addition, from the Boltzmann distribution, most of the molecules are initially in the lowest vibrational state, and therefore Stokes Raman scattering is usually stronger than anti-Stokes scattering.

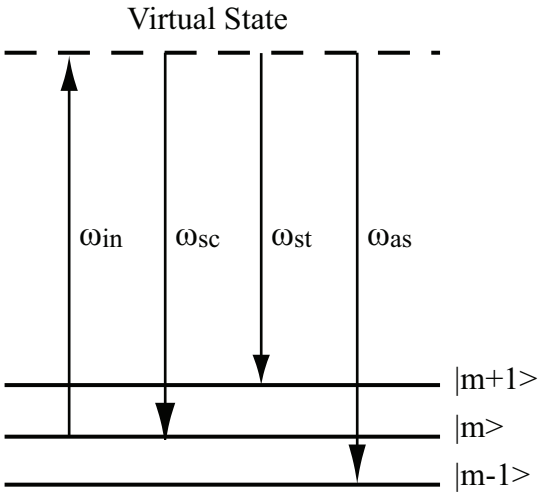

Fig. 2.1 Energy diagram of light scattering. When the initial and final stationary states are the same ($\omega_{sc} = \omega_{in}$), Rayleigh (elastic) scattering occurs. Stokes Raman scattering ($\omega_{st} < \omega_{in}$) is a result of molecule vibration transition to a higher energy level (|m+1>), while anti-Stokes Raman scattering ($\omega_{as} > \omega_{in}$) is due to a decrease in quantum number, |m> to |m-1>.

Raman spectroscopy has been developed as a powerful tool for chemical measurements of molecular species [4, 32-35]. It can be used to analyze different kinds of materials such as gases, vapors, aerosols, liquids and solids. Clinical applications of Raman spectroscopy and microscopy have been widely demonstrated [36-39], but they are limited not only by the difficulty in acquiring the inherently weak tissue Raman signals interacting with a strong fluorescence background, but also by the relatively too long spectral and imaging acquisition time. Enhancement on weak Raman signals

by several orders of magnitude can be realized by coherent Raman technique, of which coherent anti-Stokes Raman scattering (CARS) is the most popular.

2.1.2 Fundamental theory of CARS

Coherent anti-Stokes Raman scattering (CARS) is a well-known four-wave mixing process involving a pump, a Stokes and a probe field with frequencies of ω_p, ω_S, and ω_{pr}, respectively, interacting with matter to induce a third-order nonlinear polarization $P^{(3)}$ at the anti-Stokes frequency of $\omega_{as} = \omega_p - \omega_S + \omega_{pr}$ [8, 27]. Generally, experiments are often performed in a frequency-degenerated manner for simplicity, that is, the pump and probe beams come from the same laser source ($\omega_p = \omega_{pr}$), so that $\omega_{as} = 2\omega_p - \omega_S$. Fig. 2.2(a) shows the energy diagram of the CARS process [40].

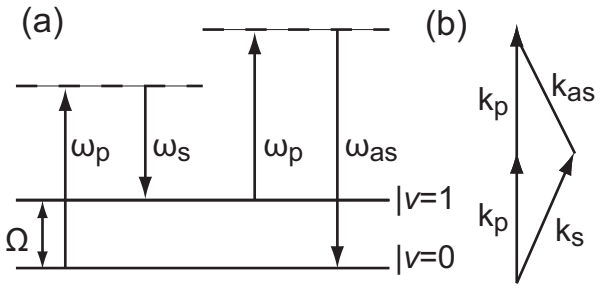

Fig. 2.2 (a) Energy diagram of CARS process, and (b) Phase matching condition in CARS radiation.

The anti-Stokes field (E_{as}) is related with the third-order nonlinear polarization ($P^{(3)}$) by the wave equation (assuming an isotropic medium) derived from the Maxwell's relations [41],

$$\left[\nabla^2 + \frac{\omega_{as}}{c^2}\varepsilon_{as}(\omega_{as})\right]E_{as} = -\frac{4\pi\omega_{as}^2}{c^2}P^{(3)}. \qquad (2.2)$$

Here ε_{as} is the dielectric constant, c is the light speed in vacuum and $P^{(3)}$ can be described by

$$P^{(3)} = \chi^{(3)} E_p E_p E_S^* = (\chi^{(3)r} + \chi^{(3)nr}) E_p E_p E_S^*, \tag{2.3}$$

where E_p and E_S are the amplitudes of the pump and Stokes fields, respectively; $\chi^{(3)}$ is the third-order nonlinear susceptibility, which comprises a resonant part, $\chi^{(3)r}$, and a nonresonant part, $\chi^{(3)nr}$. The resonant part $\chi^{(3)r}$ is a complex quantity and represents the Raman response of the molecular vibrations. It is expressed as

$$\chi^{(3)r} = \frac{A}{(\omega_p - \omega_S - \Omega) + i\Gamma}, \tag{2.4}$$

where A is a constant related to the mode density and the Raman cross-section, Ω is the vibrational frequency, and 2Γ is the Raman linewidth.

The intensity of the CARS signal, I_{as}, is written as,

$$I_{as} = \frac{2\pi\omega_{as}^2}{c\varepsilon_{as}} \left|\chi^{(3)r} + \chi^{(3)nr}\right|^2 \left|E_p\right|^4 \left|E_S\right|^2 \frac{\sin^2(\Delta kl/2)}{(\Delta kl/2)^2}, \tag{2.5}$$

The last factor $\mathrm{sinc}^2(\Delta kl/2)$ in Eq. (2.5) is maximized when the wave vectors of the pump, the Stokes and the CARS fields, k_p, k_S, k_{as}, respectively, satisfy the phase-matching condition, $\Delta k \cdot l < \pi$, where l is the coherent interaction length and $\Delta k = 2k_p - k_S - k_{as}$ is the wave vector mismatch. Because of the strictly-defined phase relationship, CARS signal can only be coherently generated in a certain direction, as shown in Fig. 2.2(b). From Eq. (2.5), obviously, the overall CARS signal is proportional to $\left|\chi^{(3)r} + \chi^{(3)nr}\right|^2$, and the resonant CARS signal can be greatly enhanced

when the resonant condition of $\omega_p - \omega_S = \Omega$ holds. The nonresonant part $\chi^{(3)nr}$ is a real quantity and is essentially independent of the excitation frequencies. It is important to realize that the concurrent $\chi^{(3)nr}$ is the source of the nonresonant background limiting the contrast and sensitivity of resonant CARS detection.

The third-order nonlinear susceptibility ($\chi^{(3)}$) is actually a four-rank tensor containing 81 elements, of which only a few are independent in a symmetrical system. In the most commonly used frequency-degenerated CARS, the components of induced third-order nonlinear polarization at $\omega_{as} = 2\omega_p - \omega_S$ by the pump and Stokes fields at ω_p and ω_S, respectively, can be written as

$$P_\alpha^{(3)}(\omega_{as}) = 3\sum_{\beta\gamma\delta} \chi_{\alpha\beta\gamma\delta}^{(3)}(-\omega_{as}, \omega_p, \omega_p, -\omega_S) \times E_\beta(\omega_p) E_\gamma(\omega_p) E_\delta^*(\omega_S). \tag{2.6}$$

The subscripts $\alpha\beta\gamma\delta$ refer to the Cartesian axis labels and define the polarization directions of the induced polarization (CARS), the pump, probe and Stokes fields, respectively. Considering the macroscopic symmetry properties of the medium, the number of terms in Eq. (2.6) can be further reduced. For isotropic media such as liquids and gases, it has been shown by symmetry arguments that only three susceptibility terms are independent with the following relationship:

$$\chi_{1111}^{(3)} = \chi_{1122}^{(3)} + \chi_{1212}^{(3)} + \chi_{1221}^{(3)}. \tag{2.7}$$

Here, supposing the beams propagate along the z-axis, and “1” and “2” indicate the x- and y-axis, respectively.

The ratio between the susceptibility components $\chi_{1221}^{(3)}$ and $\chi_{1111}^{(3)}$ is defined as

the CARS depolarization ratio,

$$\rho_{nr} = \frac{\chi^{(3)nr}_{1221}}{\chi^{(3)nr}_{1111}} \quad \text{and} \quad \rho_{r} = \frac{\chi^{(3)r}_{1221}}{\chi^{(3)r}_{1111}} \tag{2.8}$$

Here, ρ_{nr} and ρ_{r} are the nonresonant and resonant CARS depolarization ratios, respectively. Far from any resonance of the system, according to Kleinman's symmetry conjecture [42], $\chi^{(3)nr}_{1122} = \chi^{(3)nr}_{1212} = \chi^{(3)nr}_{1221} = \chi^{(3)nr}_{1111}/3$ holds, and $\rho_{nr} \approx 1/3$.

2.2 Experimental Instrumentations of CARS Microscopy

CARS imaging provides a new approach to generate chemically selective contrast based on molecular vibrations, and therefore it has become an attractive technique for a broad variety of biological and biomedical applications. To establish a robust CARS microscope, several aspects of strategies should be considered, including the selection of ultrafast laser sources, excitation geometry and detection schemes, and methods for nonresonant background suppression.

2.2.1 Laser sources for CARS microscopy

To choose the ideal laser sources for CARS microscopy, several parameters should be remarked. First is the wavelength range. It has been found that CARS with UV/VIS wavelength excitation results in large nonresonant background due to the two-photon resonant interactions [24]. In contrast, NIR excitation minimizes the nonresonant signals because they are far away from the two-photon resonance [8, 18]. Another advantage of NIR excitation is the low absorption and therefore small photodamge to the samples [43]. In addition, NIR light can penetrate deeper than UV/VIS light in

highly scattering samples, which is important for CARS clinical applications. Secondly, pulsed laser excitation is necessary because CARS signal generation is cubically dependent on the power of the incident light intensities [41]. The pulse width is another important parameter that affects the resonant signal to nonresonant background ratio in CARS imaging. It has been proved that the bandwidth of a several-picosecond (2~5ps) pulse can match well with the linewidth of most of the Raman resonant vibration bands (10~20 cm^{-1}) for optimizing the CARS signal excitation with improved spectral resolution and minimized nonresonant background [44].

In the first CARS microscopy built by Ducan and coworkers [24], two synchronously pumped mode-lock pulsed dye lasers were used. Zumbusch et al. [18, 26] used a regeneratively amplified Ti:sapphire laser pumped optical parametric amplifier system (Coherent, RegA/OPA). After that, two electronically synchronized mode-locked Ti:sapphire oscillators with high repetition rate (~80 MHz) and several ps temporal bandwidth significantly improved the spectral resolution and sensitivity in CARS microscopy [45]. As a simple and economic approach, one Ti:sapphire fs/ps laser source and one OPO system can also be used [46]. However, the limitation of this scheme is that it can only cover the Raman shift above ~2000 cm^{-1}. As the latest CARS source, Ganikhanov et al. used the signal and idler output from an optical parametric oscillator (OPO) as the pump and Stokes beam, respectively, for CARS microscopy and the most recently design can maintain the pump and Stokes pulse trains are temporally synchronized and spatially overlapped at the output of the OPO [47, 48]. Besides, fiber laser sources have the potential to develop low cost and portable CARS

systems helpful for clinical studies [49-51]. It is believed that the new advances on ultrafast laser sources will further boost the developments of CARS microscopy.

2.2.2 Laser scanning CARS microscope

Fig. 2.3 shows the schematic of a typical laser-scanning CARS microscope. The synchronized pump and Stokes beam through an optical delay line are collinearly combined on a dichroic mirror and introduced into a customized laser scanning confocal microscope. The incident laser beams are tightly focused onto the sample by high numerical aperture microscope objective. Imaging is realized by scanning the beams through a two-dimensional galvanometer mirror unit. Based on the phase matching condition shown in Fig. 2.2(b), most of the generated CARS signals are radiated in the forward detection and can be detected by the photomultiplier tube (PMT1) through a short pass filter set.

In addition to the forward CARS generation, it has been demonstrated theoretically and experimentally that the epi-detection CARS (E-CARS) signal is also present and can be used to reveal small intracellular features that may be overwhelmed by the strong CARS signal from the bulky medium as in forward CARS detection [25, 52]. The meaning of E-CARS was further validated by the experiments in thick tissue imaging, in which the E-CARS signal will be enhanced due to the multi-scattering and back reflection of the forward CARS signals. In the experimental setup shown in Fig. 2.3, two epi-detection channel are provided, a non-descan channel (PMT2) and a descan channel (PMT3). The major advantage of the non-descan channel is its relatively larger signal level but with loss of sectioning ability. Moreover, the

developing of CARS endoscopy for tissue imaging and disease diagnostics is ongoing, for which E-CARS detection scheme would be the best choice.

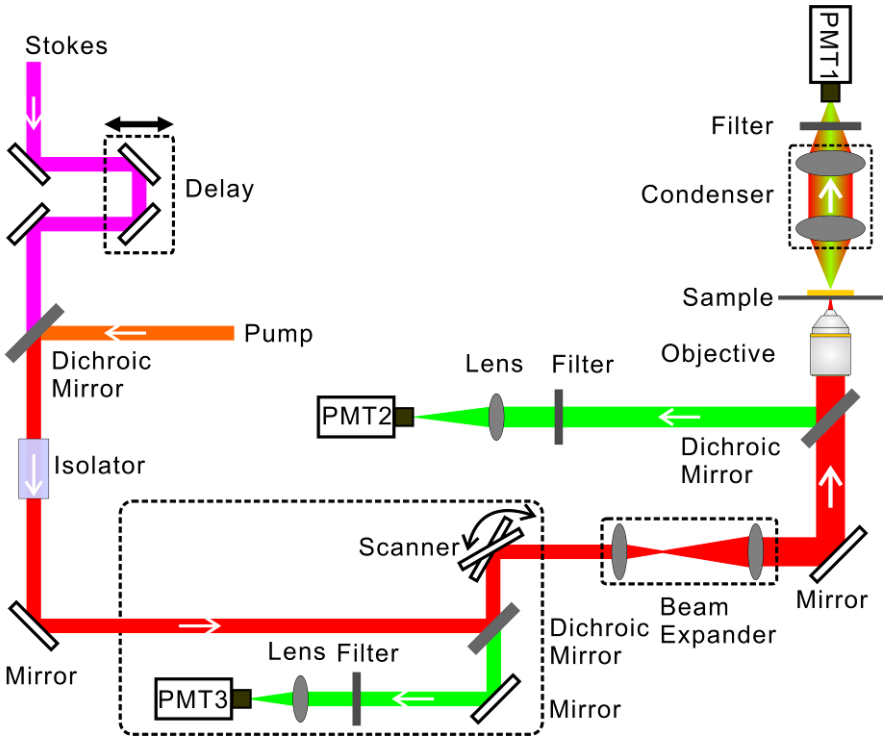

Fig. 2.3 Schematic of a laser-scanning CARS microscope with a collinear excitation geometry, and forward and backward (epi-) detection fashions.

2.2.3 Multiplex CARS microspectroscopy

While CARS microscopy provides specific molecular distributions by fast mapping with chemical specificity, multiplex CARS (M-CARS) microspectroscopy allows simultaneous detection over a wide range of Raman shift of the molecular vibrations with high sensitivity. The first multiplex CARS spectroscopy was demonstrated by Akhmanov and colleagues with fast data acquisition capacity [53]. In M-CARS experiment, a narrow band pump beam and a broadband Stokes beam are used to excite the sample and the CARS radiations over a significant range of the vibrational spectra are measured by a spectrometer or CCD system. Raman spectroscopy has been developed over a wide range of Raman shift for biological and biomedical applications

(400 cm^{-1} to 4000 cm^{-1}). But it suffers from low signal level mixing with the large fluorescent background, resulting in too high excitation power and extremely long acquisition time, while multiplex CARS spectroscopy increases the spectral sensitivity coherently by several orders of magnitude with blue-shifted emission for easy filtering and detection.

In the previous work of M-CARS spectroscopy, a narrow band picosecond dye laser and a broadband pulsed dye laser were used as the pump and Stoke beam, respectively [54-57]. Recently, M-CARS has been developed with picosecond Ti:sapphire laser and femtosecond laser in NIR range with high repetition rate [58, 59]; however, this fashion limited the bandwidth of the vibrational sensitivity in M-CARS due to relatively narrow bandwidth of the Stokes beam. Very recently, the developments on the supercontinuum generation by photonic crystal fibers (PCF) offer a promising broadband pulsed laser source as the Stokes beam. The M-CARS spectral bandwidth can be up to 2500 cm^{-1} with this new developed light source [60-76]. Unfortunately, the robustness and stability of PCF-based supercontinuum light source is still remained to be a challenge.

Due to the existence of the nonresonant background mainly from the two-photon resonant transition, the CARS spectrum may suffer from a distortion compared with the pure resonant Raman spectrum. Polarization-sensitive detection is widely used in M-CARS for pure resonant CARS signal measurements. Voroshilov and colleagues utilized polarization-sensitive CARS to study proteins (bovine albumin) in D_2O [55]; Murpel et al. imaged multilamellar lipid vesicles formed by DSPC [77, 78]. Another

approach for resonant detection is to use a least-square fit of the theoretical expression for the CARS spectrum to the experimental data [79], but this method is based on sufficient starting information about the vibrational spectrum of the chemical compounds in the samples. Recently, it has also been demonstrated that the imaginary part of the CARS spectrum, which is proportional to the Raman spectrum, can also be discriminated from the nonresonant backgrounds [80].

To conclude, M-CARS microspectroscopy combining both a point CARS spectroscopy over a wide range of Raman shift and laser-scanning imaging based on one or a few Raman peaks offers a very promising tool for both chemical analysis and chemically-selective mapping in biological and biomedical applications.

2.3 Suppression of Nonresonant Background in CARS Microscopy

From the theory of the CARS process (Section 1.2.2), the major drawback of CARS microscopy is the existence of the nonresonant background. The strong nonresonant signal mainly arising from the electronic contributions of surrounding solvent and other media in biological samples degrades the vibrational contrast and chemical specificity in CARS imaging. There are three straightforward approaches to suppress the nonresonant background: One is to use NIR excitation instead of UV/VIS light sources, since NIR excitation gives rise to relatively low nonresonant signals. Another way is to use picosecond rather than femtosecond pulses since the spectral bandwidth of several picosecond pulses match well with the bandwidth of most of the Raman lines (~10-20 cm^{-1}), which minimizes the generation of the nonresonant backgrounds.

Finally, as a simple but effective method to remove the nonresonant background is to directly subtract the off-resonance CARS image at the dip position of the CARS spectrum from the on-resonance CARS image [48]. Duncan et al. used this method for the first time to image deuterated liposomes [81]. However, this process omits the coherent mixing of the resonant and nonresonant signals, resulting in a distortion on the pure resonant information.

To further suppress the nonresonant background and improve the chemical specificity, a few techniques have been developed, including backward (epi-) detection [25, 52, 82], counter-propagating excitation [28], polarization-sensitive detection [22, 29, 83-90], time-resolved detection [58, 91-101], pulse-shaping technique [102, 103], focus-engineered technique [104, 105], interferometric technique [46, 106-112]. These methods are summarized as follows.

2.3.1 Backward (Epi-) detection CARS [25, 52, 82]

In isotropic and homogenous bulky samples, the CARS signal radiates in the forward direction following the phase matching condition. However, in complex and heterogeneous specimens, the small scatters with much smaller size compared with the excitation wavelengths and the discontinuity interfaces of $\chi^{(3)}$ result in the destruction of the phase matching condition, and therefore backward (epi-) signal reflection. Based on its mechanism, epi-detection CARS (E-CARS) avoids the large CARS signals from the bulky medium and provides a simple means to detect small objects and specific details embedded in the medium. But because E-CARS filters the signal based on the size of scatters, rather than the real resonant vibrations, the spectral sensitivity of

E-CARS is still limited and distorted by the nonresonant background from the small objects and the discontinuity interfaces. It should also be outlined that E-CARS is the most reasonable scheme for live animal imaging and in-vivo endoscopic detection because forward CARS signal cannot penetrate thick tissues.

2.3.2 Counter-propagating CARS [28]

In counter-propagating CARS (C-CARS), the pump and Stokes beams propagate collinearly but in the opposite direction. This fashion with large non-phase-matching condition avoids the signal generation from the bulky medium. In contrast, with the presence of small scatters and discontinuous interfaces, part of the non-phase-matching incident excitation will be brought into phase-matching condition for CARS signal generation. Similar to E-CARS, C-CARS is also sensitive to small objects and details in the samples by suppressing the large signal from bulky medium of the samples. The drawbacks of this method include the complex experimental configuration and very weak signal level. Wide-field CARS imaging system was established and demonstrated based on this scheme [113, 114].

2.3.3 Polarization-sensitive CARS [22, 29, 83-90]

The polarization-sensitive detection CARS (P-CARS) is based on the different polarization properties of the resonant and nonresonant third-order nonlinear susceptibilities. The principle of P-CARS microscopy is briefly outlined in Fig. 2.4, in which the pump beam E_p is linearly polarized along the x-axis and the Stokes beam E_S is linearly polarized with an angle of ϕ relative to the x-axis. The x and y components of the nonresonant part P^{NR} of the third-order polarization can be

written as

$$P_x^{NR} = 3\chi_{1111}^{NR} E_P^2 E_S^* \cos\phi, \tag{2.9}$$

$$P_y^{NR} = 3\chi_{2112}^{NR} E_P^2 E_S^* \sin\phi\,. \tag{2.10}$$

Hence, the nonresonant part P^{NR} is linearly polarized with an angle of θ relative to the x axis,

$$\mathrm{P}^{\mathrm{NR}} = 3\chi_{1111}^{NR} E_P^2 E_S^* \cos\phi / \cos\theta\,. \tag{2.11}$$

Here, the angle θ is related with ϕ by $\tan\theta = \tan\phi \chi_{2112}^{NR} / \chi_{1111}^{NR} = \rho_{NR} \tan\phi$. ρ_{NR} is the depolarization ratio of the nonresonant third-order polarization, and can be estimated as a value of 1/3, following the Kleinman's symmetry assumption. Similarly, the x and y components of the resonant part P^R of the third-order polarization can be expressed as

$$P_x^R = 3\chi_{1111}^R E_P^2 E_S^* \cos\phi, \tag{2.12}$$

$$P_y^R = 3\chi_{2112}^R E_P^2 E_S^* \sin\phi. \tag{2.13}$$

As the nonlinear coefficients of the resonant component are different from those of nonresonant component, the resonant component of the induced polarization is polarized in the direction different from that of the nonresonant counterpart. Hence, by placing a polarization analyzer perpendicular to the nonresonant polarization component (Fig. 2.4), it is simple to determine the amplitude of the resonant signal as follows:

$$\mathrm{P}_{\perp} = 3\chi_{1111}^R E_p^2 E_s^* (\cos\phi \sin\theta - \rho_R \sin\phi \cos\theta)\,. \tag{2.14}$$

Here, ρ_R is the depolarization ratio of the resonant third-order polarization. In order to

get the maximum vibrational contrast, the angle ϕ should be set as 71.6°, and accordingly, θ has a value of approximately 45°.

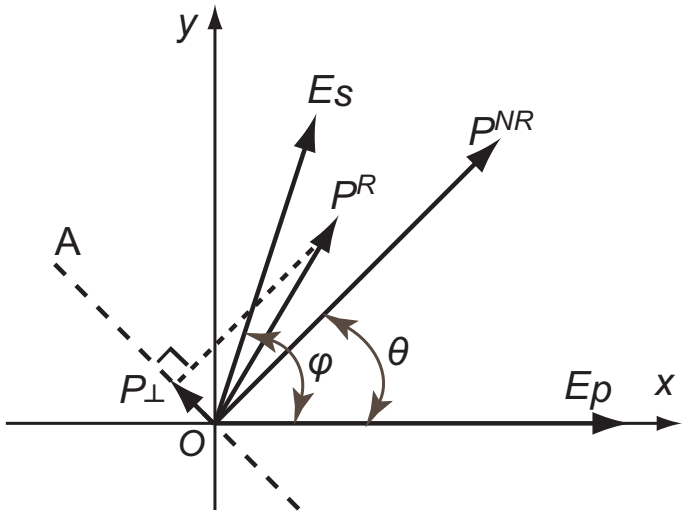

Fig. 2.4 Principle of polarization CARS. Vectors of the pump and Stokes fields, the generated resonant and nonresonant CARS signals, and the analyzer orientation (A) for polarization CARS.

P-CARS detection has been successfully applied for background-free CARS spectrum acquisition and resonant CARS imaging. Cheng et al. reported the P-CARS spectrum of N-methylacetamide at 1652 cm^{-1} (Amide I band) and the corresponding P-CARS image of unstained epithelial cells [29]. Nan et al. reported the P-CARS image of the lipid droplets in a differentiated 3T3-L1 cell at the Raman shift of 2845 cm^{-1} (aliphatic C-H vibration) with high vibrational contrast and high chemical specificity [115]. However, from Eq. (2.14), the background-free CARS signal of $P_{\perp}$ is only a very small fraction of the total resonant signal in intensity, thus P-CARS microscopy always suffers from a severe reduction on the resonant signals, which hinders its wide applications in detecting weak signals in real biological systems.

2.3.4 Time-resolved CARS [58, 91-101, 110]

Time-resolved detection makes use of the different temporal behavior of the resonant

and nonresonant CARS radiations. The nonresonant component of the signal shows an instantaneous response to the excitation fields and therefore holds very short decay time (several hundred femtosecond), while the resonant part involves a real vibrational Raman-active transition, which results in a longer decay time (on the order of several picoseconds). In experiments, the nonresonant background can be removed by introducing a suitably delayed probe beam relative to the pump and Stokes beams. In order to discriminate the time-resolved CARS signal from the overall radiation, the probe beam usually has a different wavelength from the pump beam, so-called three-color CARS [94]. For degenerated CARS, a perpendicularly polarized probe beam to the pump beam can be used to discriminate the time-resolved signal through a polarization analyzer [72]. One drawback of time-resolved CARS is that during the rejection of the nonresonant CARS signal, most part of the resonant signal is also been suppressed, resulting in very low detection sensitivity. Interference method has also been used for time-resolved resonant signal detection [110].

2.3.5 Pulse shaping in femtosecond excitation CARS [102, 103]

4-f configured paired-gratings filtering of a femtosecond (fs) laser source can be used to generate ps laser pulses for high contrast CARS imaging. Phase-shaping of the femtosecond pump and Stokes beams can also realize high spectral resolution by appropriately modulating the spectral phase of the pulse to selectively populate a given vibrational level [103].

2.3.6 Interferometric CARS [46, 106-112]

Different from fluorescence emission, CARS radiation is highly coherent, which

provides a potential approach for background-free CARS detection by interferometric method. Marks et al. reported a nonlinear interferometric vibrational imaging implementation, which measured the resonant radiation by obtaining the temporal anti-Stokes signal through nonlinear interferometry [110]. Evans and Potma and coworkers demonstrated a CARS heterodyne spectral interferometer to retrieve the real and imaginary components of the third-order nonlinear susceptibility and yielded amplified resonant signals that are linear to conventional P-CARS [107, 116].

In conclusion, researchers have tried to suppress the nonresonant background in CARS imaging through a wide variety of technical approaches. These methods can realize background-free imaging. However, they either make the system too complex or attenuate the resonant CARS signals seriously. It is highly desirable to develop a robust and easy-to-operate CARS microscopy with better spectral resolution and high sensitivity for biological and biomedical applications.

2.4 CARS Applications in Life Sciences

The rapid technical developments during the last decade have enabled CARS microscopy to be widely applied to the chemical, materials, biological and medical sciences. One major advantage of CARS compared with spontaneous Raman scattering is that in CARS process the inherently weak Raman-active molecular vibrations are greatly enhanced by several orders of magnitude, allowing fast imaging acquisition with high sensitivity. Further, the most unique property of CARS microscopy lies in its intrinsic chemical selectivity [8]. Fig. 2.5(a) shows the Raman spectrum of lipids droplets in water. The peak at 2870 cm^{-1} corresponds to the CH_2

vibrations from the lipid bodies, while the peak centered at 3300 cm^{-1} is from the OH bonds in water. CARS imaging with frequency difference between the pump and Stokes beams tuning at 2870 cm^{-1} yields bright lipid bodies with dark background of water as shown in Figs. 2.5(b, d). In contrast, tuning the excitation frequency difference to 3300 cm^{-1}, the lipid bodies become dark, while the water background turns to be brighter (Figs. 2.5(c, e)), demonstrating the intrinsic chemical selectivity in CARS imaging. In addition, saturated and unsaturated lipids could also be distinguished using a wide-field CARS imaging system [117]. In this section, recent applications of CARS microscopy for biology and biomedicine are comprehensively reviewed at both the cellular level and tissue level.

2.4.1 Cellular imaging

Water has a strong Raman-active vibration centered at 3300 cm^{-1} from OH bonds, which gives rise to intense resonant CARS signals. One of the very interesting CARS applications is the real time visualization of intracellular hydrodynamics in a single living cell [118, 119]. Cheng et al. further reported that the imaging contrast based the CARS signal from water molecules close to the phospholipid bilayer is dependent on the excitation field polarization [120]. Their results showed that water molecules between phospholipid bilayers were ordered with the symmetry axis along the direction normal to the bilayer.

CARS microscopy has been widely applied to lipid-related imaging. It has been proven to be particularly successful in imaging lipid membranes. The C-H bonds abundant in the aliphatic chains of the lipid bilayer generate strong CARS signals,

allowing CARS microscopy for the direct visualization of cellular phospholipid membranes under physiological conditions.

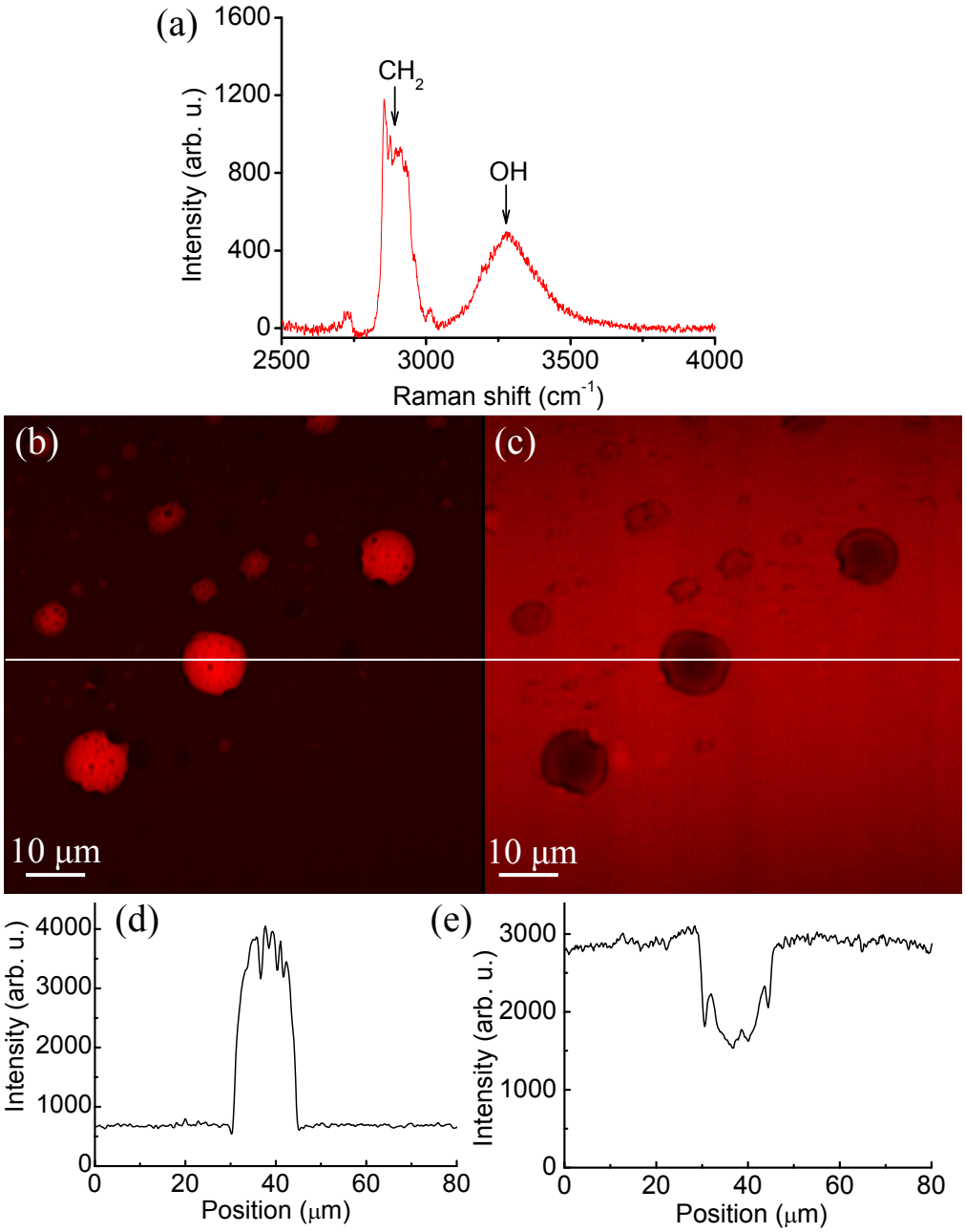

Fig. 2.5 (a) Raman spectra of lipid droplets and water. The peak position of lipids (CH_2 bonds) is at 2870 cm^{-1}, while the peak position of water (OH bonds) is at 3300 cm^{-1}. (b) and (c) are CARS images of lipid droplets in water with Raman shift tuning at 2870 cm^{-1} and 3300 cm^{-1}, respectively. The intensity profiles across the lines indicated in Figs. (b, c) are shown in Figs. (d, e).

CARS microscopy provides a new approach to view cellular structures and

intercellular and intracellular dynamic processes. For example, CARS imaging has been used to monitor the transportation and accumulation of lipid droplets in living cells [19, 115, 121-124]. Due to its high sensitivity to lipids, CARS microscopy was used to detect very small lipid vesicles with less than 300 nm dimensions in living cells without staining [115]. Fig. 2.6 shows the CARS image of unstained living normal and mutant yeast cells. In Fig. 2.6(b), one or several round lipid bodies in each cell were visualized clearly without fluorescence staining, while there were no lipid bodies in the normal yeast cells (Fig. 2.6(a)). Since CARS is a totally nonperturbative approach for cellular imaging, it allows long term investigation on the living cells without affecting and altering the chemical structures and functionality of the cellular organelles.

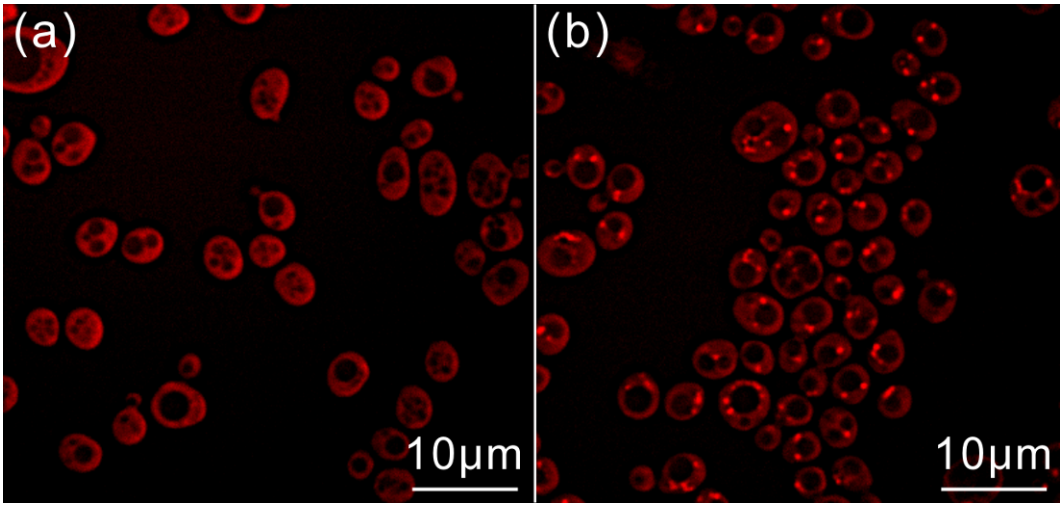

Fig. 2.6 CARS images of (a) normal, and (b) mutant yeast cells cultured with QKO, which lacks of neutral fat (triglyceride (TG) and steryl esters (SE)). The Raman shift was tuned to 2870 cm^{-1} corresponding to CH_2 stretching vibration. This model can be used for analyzing human lipid-associated diseases.

Another important application of CARS microscopy is the metabolic imaging on lipids [125]. In cell culturing with non deuterated Eicosapentaenoic acid (EPA, fish oil) and deuterated oleic acid (OA), Xie et al. found that the two fatty acids colocalized in

the lysosomes, the digestive organelles in cells, in the form of triglycerides. However, when EPA was absent, OA was not incorporated into the lysosomes [126]. This work provided an important assay towards the understanding of fish oil's health benefits at biological system levels, especially for the study of obesity-related diseases. In addition, CARS microscopy has also been used to investigate the changes in lipid metabolism caused by the hepatitis C virus [127].

Konorov and coworkers utilized CARS microscopy to identify the differentiated and undifferentiated mouse embryonic stem cells (ESC) based on selective observation of specific molecular vibrations as the intrinsic spectroscopic markers [128]. Very recently, Murugkar and colleagues reported the chemically selective imaging of cryptosporidium at the single oocyst level [129]. Their work demonstrated the potential of CARS microscopy to detect waterborne pathogens in a few seconds without the need for labeling.

2.4.2 Tissue imaging

Over the past few years, many biomedical applications of CARS microscopy have been reported for both in vivo and in situ investigations. The first CARS tissue imaging in vivo was demonstrated on the living animal skin by Evans and coworkers with a video-rate CARS imaging system [43]. It was demonstrated that CARS microscopy is able to visualize lipid-rich tissue structures in the skin of a living mouse, including sebaceous glands, corneocytes, and adipocytes with both intrinsic chemical specificity and subcellular resolution.

Myelin sheath is a lipid-rich plasma membrane wrapping around an axon and it is

important for neural impulse conduction, while demyelination, the loss of normal myelin sheath, accounts for long-term neurologic disability. Cheng's group has systematically investigated the demyelination disease using CARS microscopy by sensing the high-density CH_2 bonds in lipids [130-140]. Their results showed that the breakdown of myelin sheath was featured by decrease of CARS signal intensities and loss of polarization sensitivity and they also found that the paranodal myelin degradation may be a possible onset of demyelination in multiple sclerosis. It was demonstrated that exposure of white matter to glutamate resulted in paranodal myelin splitting and retraction.

Hellerer et al. applied CARS microscopy to quantitatively monitor the impact of genetic variations in metabolic pathways on lipid storage in 60 specimens of Caenorhabditis elegans [141]. Their work indicated that CARS microscopy allowed chemically specific and label-free imaging in living organism. Le et al. combined CARS microscopy with TPEF microscopy and Raman spectroscopy to visualize and analyze the coexistence of neutral and autofluorescent lipid species in live mutant C. elegans [142]. Their results indicated that complex genotype-phenotype relationship between lipid storage, peroxidation, and desaturation could be rapidly and quantitatively analyzed by multifunctional CARS microscopy.

Fatty liver may progress to liver steatohepatitis, cirrhosis, or even hepatocelluar carcinoma. Wu et al. using CARS microscopy demonstrated the specific imaging of fat droplets in intact liver tissue and extracted the hepatic fat content through imaging analysis without the need of tedious sample preparation required by traditional

histopathological examination [143]. Their results proved the capability of CARS microscopy for quantitative assessment of fat in intact tissues. Combing with the diverse animal models of diseases related to metabolic disordered of lipids, CARS microscopy would enable to acquire the important insight into the genetic or dietary factors affecting the uptake and accumulation of fat within tissues for a wide variety of obesity-related disease studies. CARS microscopy was also applied to investigate many other tissue samples including human hair [144], oral solid dosage [145], dogariu blood [146], and mouse brain [130, 147]. Lipid metabolism in cancer cells has also been preliminarily studied by CARS imaging [148].

Xu et al. applied CARS microscopy to monitor the intracellular drug delivery with unlabeled nanoparticles [149]. Kang et al. utilized CARS microscopy to examine paclitaxel distribution in various polymer films with submicron 3D resolution [150, 151]. Their results confirmed that CARS microscopy could be applied effectively for in situ imaging of native drug molecules in a delivery system with a label-free and noninvasive manner.

Metal oxide nanoparticles are being used for drug delivery vehicles, but their potential associated with health risks is still largely unknown. Moger et al. imaged 20-70 nm metal oxide nanoparticles in the fish gill and showed that CARS microscopy can provide localization of nanoparticles within biological structures at the cellular level [152]. Jung et al. demonstrated gold nanorods imaging by plasmon-resonance-enhanced four-wave-mixing [153]. Baltog and Lefrant et al. also demonstrated that large CARS signals can be acquired from single-walled carbon

nanotube due to the surface plasmon resonance enhancement [154-157]. It is predicated that CARS imaging would has great applicable potential on nano-material and related applications.

Deep tissue imaging is always an attractive advancing direction for optical bioimaging. Inserting miniature focusing optics into soft samples provides an effective approach to image deep tissue with minimal surgery. Wang et al. used a miniature objective lens to extend the penetration depth of CARS microscopy for rat spinal cord white matter imaging with a minimal requirement for surgery as deep as 5 mm from the surface [158]. Another method to realize deep tissue imaging is tissue clear process. Zimmerley et al. used SHG and CARS to follow the process of optical clearing in human skin [159]. Their experiment provided for a role of DMSO in compromising the structure of collagen fibers, associated with a reduction of the tissue's scattering properties.

Technical advances in the last decade have made CARS microscopy a state-of-the-art technique for biological and biomedical imaging. It has significantly contributed to biology and biomedicine with its unique label-free chemical selectivity.

2.5 Integrated CARS and Multiphoton Multimodal Nonlinear Optical Microscopy

CARS microscopy shows high sensitivity for lipid-rich biological compounds. However, the components of tissue samples usually are very complex. In order to study disease at tissue level with different chemical specificities, to combine several multiphoton modalities in one platform would be a viable means. A so-called

multimodal nonlinear optical (NLO) microscopy incorporating CARS, TPEF, SHG, THG, or SFG has been applied for several biological and biomedical applications. For example, multimodal NLO microscopy would be a potential approach for cardiovascular disease diagnosis. Wang et al. utilized multimodal NLO microscopy to image arterial cells and extracellular matrix [160]. CARS imaging allowed visualization of endothelial cells and smooth muscle cells of the arterial wall. The extracellular matrix organization was confirmed by TPEF signals arising from elastin's autofluorescence and SFG signals arising from collagen fibrils due to their non-centrosymmetric structure. The results suggested the potential application of multimodal NLO microscopy to monitor onset and progression of arterial diseases. Le et al. characterized the metabolic syndrome-induced cardiovascular plaques by multimodal NLO microscopy [161]. Wang et al. demonstrated the imaging and quantitative analysis of atherosclerotic lesions by multimodal NLO microscopy [162]. Foam cells, lipid deposits, matrices, and fibrous caps were visualized. Starting from the adaptive intimal thickening in the initial stage to the fibrous atheroma or mineralization in the advanced stages, lesions were visualized without labels. They have demonstrated the capability of multimodal NLO microscopy to interrogate different stages of lesion development with subcellular details to permit quantitative analysis of lipid and collagen contents. Mansfield et al. utilized multimodal NLO microscopy to investigate the elastin fiber network in healthy equine articular cartilage from the metacarpophalangeal joint [163]. The elastin fibers were identified using TPEF microscopy, the collagen matrix was revealed by SHG imaging, while CARS

was used to clearly delineate the cell boundaries. Pfeffer et al. reported multimodal NLO imaging of fascia, a rich collagen type I sheath around internal organs and muscle [164]. Their experiments demonstrated that multimodal NLO provided complementary information about the submicron architecture of collagen arrays.

Nonlinear optical (NLO) microscopy and spectroscopy has emerged as a viable means for three-dimensional molecular imaging and spectral analysis of cells, tissues or live animals [75, 159-161, 164]. There are several unique advantages using NLO microspectroscopy for tissue level disease analysis and diagnosis compared with current available techniques such as US, CT, MRI or MRS and Biopsy. First, NLO microscopy realizes label-free imaging with excellent intrinsic biochemical specificity and selectivity: Elastin, retina (NADH, FAD) radiate large two photon autofluorescence (TPF) signals; SHG is approved as an ideal imaging approach for collagen fibrils; THG microscopy is sensitive to the microstructures and interfaces in the specimens and can be used to resolve the internal structures of the collagen fibers; CARS microscopy has been successfully used for lipids imaging and fat-related dynamic monitoring in unstained live biological modals. Fig. 2.7 shows the multimodal imaging of a mouse skin sample. The collagen fibrils in dermis layer were brightened up by SHG imaging, while the fats in hypodermis layer were imaged by CARS. Multimodal imaging provided the information of the coexistence of different chemical compounds in the same sample with 3-D optical sectioning capability. Second, multimodal microscopic platform yields sub-micron spatial resolution, which could be used to image and monitor the intracellular microstructures and cellular

organs and functions. Third, compared with Biopsy, which is invasive and generally results in great pain to the patients, optical diagnosis performs noninvasively. Due to the high sensitivity and specificity of the multimodal NLO system, it can be a very powerful tool for disease diagnosis, especially for early stage detection in a label-free manner.

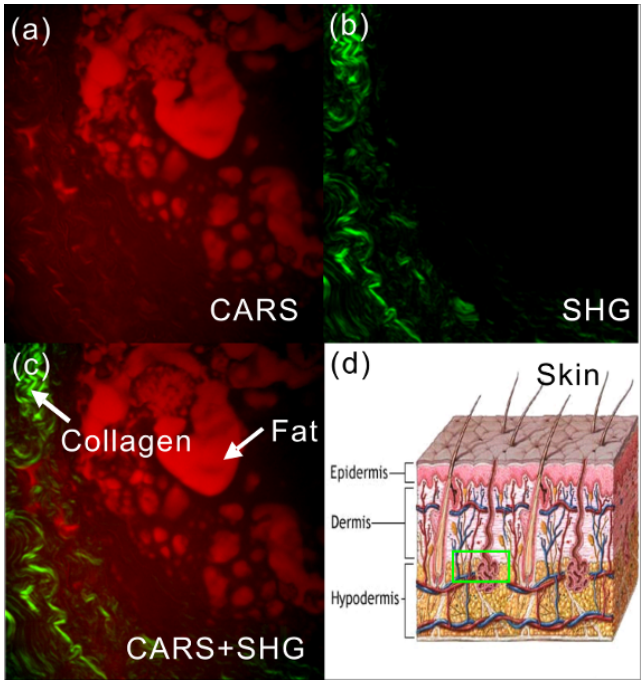

Fig. 2.7 (a) CARS image of fats in mouse skin hypodermis layer and (b) SHG image of collagen fibrils in dermis layer. (c) The merged image of collagen and fats distribution in the mouse skin tissue. (d) Schematic of skin with epidermis, dermis and hypodermis. The Raman shift of CARS is tuned to be 2840 cm^{-1} for CH_2 vibrations in lipids. The excitation beam for SHG is at 835nm.

Femtosecond (fs) pulsed lasers have been widely used for multiphoton microscopy imaging, due to the high peak power of fs lasers for the efficient generation of nonlinear signal radiation [8]. On the other hand, it is well known that picosecond (ps) pulsed lasers are ideal for CARS imaging because their spectral bandwidths match well with the Raman linewidth (~10 cm^{-1}) of biomolecules for optimizing the CARS excitation with improved spectral resolution and minimized nonresonant background

[46]. Therefore, the multimodal imaging technique usually involves in using both fs and ps laser sources which makes the technique very costly and inconvenient for operation, especially in biological laboratories [161]. To facilitate the wide applications of multimodal nonlinear optical microscopy in biological and biomedical systems, it is highly desirable to simplify the technique by only employing one fs laser source while still being able to access to different nonlinear optical microscopy imaging modalities. One of the simplistic ways to convert fs laser pulses (broad spectral bandwidth, FWHM of 100-150 cm^{-1}) into narrow spectral bandwidth ps pulses (FWHM of 5-15 cm^{-1}) is to use interference filters or narrow band-pass filters [165]; but the filters with coatings usually suffer from low damage threshold, low transmission rate, and the lack of wavelengths tunability. Light dispersion components such as prisms and gratings could be used for fs laser pulse shaping [166].

2.6 Liver Steatosis and Liver Fibrosis

2.6.1 Liver steatosis

Nonalcoholic fatty liver disease (NAFLD) is the consequence of excess triglyceride accumulation in hepatocytes without significant alcohol consumption, and therefore induces injury to hepatocytes and eventually alters liver functions [167-169]. NAFLD may develop from simple steatosis into steatohepatitis, liver fibrosis, and eventually liver cirrhosis. Nonalcoholic steatohepatitis (NASH) is a potentially serious condition associated with a significant increase in overall and liver-related morbidity and mortality.

NAFLD usually associates with obesity, type 2 diabetes mellitus, and

hyperlipidemia [170-174]. The prevalence of nonalcoholic fatty liver disease increases by 4.6-factor in obese people. The presence of type 2 diabetes mellitus significantly increases the risk and severity of NAFLD. About half of patients with hyperlipidemia were found to have NAFLD in one study. NAFLD is the most common cause of abnormal liver-test results among adults in the United States and it affects 10-24% of the general population in various countries. The prevalence increases to 57.5-74% in obese persons. NAFLD affects 2.6% children and 22.5-52.8% of obese children [173].

2.6.2 Liver fibrosis

Liver fibrosis is the excessive accumulation of extracellular matrix proteins such as collagen that occurs in most types of chronic liver diseases [175-177]. Advanced liver fibrosis results in cirrhosis, liver failure, and portal hypertension. Liver fibrosis and cirrhosis represent the consequences of a sustained wound healing response to chronic liver injury from a variety of causes including viral, autoimmune, drug induced, cholestatic, metabolic diseases and steatohepatitis [178]. Liver fibrosis appears to be one of the most important prognostic factor in patients with NAFLD because the presence of fibrosis indicates a more advanced and severe liver injury.

In liver fibrosis, the abnormal increase in collagen fibers causes the dearrangement of liver architecture, hampers intrahepatic blood flow, and subsequently causes persistent and progressive hepatic dysfunctions [179]. Cirrhosis affects hundreds of millions of patient worldwide. For example, in US, cirrhosis is estimated at 360 per 100,000 population. It is the most common non-neoplastic cause of death among hepatobility and digestive disease, accounting for approximately 30,000 deaths per

year [176].

2.6.3 Relationship between liver steatosis and liver fibrosis

NAFLD or NASH has been recognized as a major cause of liver fibrosis. However, currently there is no sufficient prospective information about natural history, risk factors for fibrosis, and rate of fibrosis progression in NASH. Steatosis is increasingly recognized as a determinant of hepatic fibrosis in both alcoholic liver disease and in NAHS [172]. In addition, it has been proved that both NAHS and liver fibrosis are reversible, which means that early disease diagnosis is very meaningful in clinics [170].

2.6.4 Diagnosis of liver diseases

Liver biopsy remains the best diagnostic tool as the gold standard for confirming liver steatosis and liver fibrosis, to be the most sensitive and specific means for providing prognostic information [180]. Liver biopsy provides important information regarding the degree of liver damage, changes in the overall liver architecture, as well as severity of inflammatory activity and fibrosis. It also provides useful information regarding prognosis and may impact clinical management. However, there are several important limitations of liver biopsy. First, as an invasive procedure with great pain to patients and significant complicated operations, biopsy is not a suitable screening test tool for regular examinations. Second, a needle liver biopsy that results in a very tiny tissue sample may be subject to significant sampling variability. Third, biopsy involves many complex procedures of sample preparation including dehydration, fixation, staining and sectioning and is laborious and time-consuming, and may also be influenced by

the skill and experience of the reading pathologists. Moreover, biopsy can only provide static data and not dynamic findings reflecting the ongoing development and does not sufficiently reveal underlying pathogenetic mechanisms.

Several imaging techniques have been advocated as noninvasive diagnostic tests for liver steatosis and fibrosis. Ultrasonography (US) can detect the diffuse increase induced by fatty infiltration or fibrogenesis in echogenicity of the liver parenchyma. Several studies demonstrated that the sensitivity, specificity, and positive predicative value of this technique to detect steatosis are as high as 80-100% [181]. However, US has very important limitations. First, it may be operator-dependent and subject to significant intra- and/or inter-observer variability. Second, accurate quantification of the degree of steatosis and fibrosis is not feasible with current US technique. Third, the sensitivity of US decreases sharply if the degree of fat or collagen infiltration is below 30% [127]. Fourth, in patients with morbid obesity, the sensitivity below 40% has been reported. Computerized tomography (CT) and magnetic resonance imaging (MRI) are more sensitive for quantification of steatosis and liver fibrosis [180]. Localized proton magnetic resonance spectroscopy (MRS) has been shown to be a noninvasive method that is highly accurate in measuring hepatic triglyceride content [182]. However, at current stage, these techniques are limited to the assessment of liver fat and fibrosis and none of these imaging techniques has sufficient sensitivity and specificity for staging the disease and cannot distinguish between fatty liver and NASH with or without fibrosis.

Chapter 3 Polarization-Encoded CARS for High Contrast Vibrational Imaging

In this chapter, both linear and elliptical polarization effects on CARS imaging were studied. Interference heterodyne detection method was applied for polarization-encoded CARS imaging of low concentration biochemical compounds in live cells with greatly improved vibrational contrast.

3.1 Linearly Polarized CARS with Heterodyne-Detection for Low Concentration Biomolecular Imaging

3.1.1 Interferometric polarization (IP-) CARS

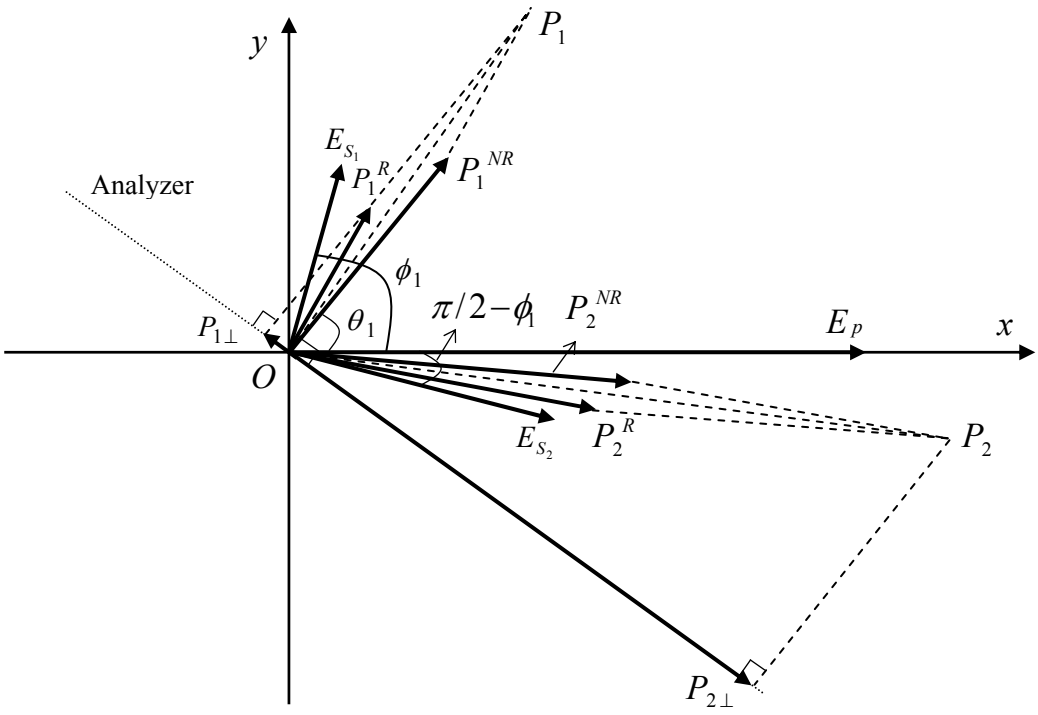

Fig. 3.1 Polarization vectors of the pump and the two Stokes fields, the generated resonant and nonresonant CARS signals, and the orientation of the analyzer (polarizer) for interferometric polarization CARS (IP-CARS) microscope.

3.1.1.1 Principle

Fig. 3.1 shows the principle of the IP-CARS microscopy, in which the pump beam E_p is linearly polarized along the x-axis and the Stokes beam E_{S_1} is linearly polarized with an angle ϕ_1, relative to the x-axis. The amplitude of the resonant signal projected on the polarization analyzer perpendicular to the nonresonant polarization component, $P_{1\perp}$, is given by [29]:

$$P_{1\perp} = 3\chi^R_{1111}E_p^2E^*_{S_1}(\cos\phi_1 \sin\theta_1 - \rho_R \sin\phi_1 \cos\theta_1)\,. \tag{3.1}$$

Here, ρ_R is the depolarization ratio of the resonant third-order nonlinear polarization. χ is the third-order nonlinear susceptibility. The angle, θ_1, is related with ϕ_1 by $\tan\theta_1 = \tan\phi_1 \chi^{NR}_{2112}/\chi^{NR}_{1111} = \rho_{NR}\tan\phi_1$, whereby ρ_{NR} is the depolarization ratio (~1/3) of the nonresonant third-order polarization, assuming the Kleinman's symmetry [42].

To overcome the limitation of low signal levels of conventional P-CARS, a second Stokes beam E_{S_2} with the polarization perpendicular to the first Stokes beam E_{S_1} to avoid their mutual interference was introduced. The projection of the third-order polarization P_2 generated by the second Stokes beam associated with the same pump beam on the analyzer, $P_{2\perp}$, can be written as

$$\begin{aligned} P_{2\perp} = {} & 3E_p^2E^*_{S_2}\chi^R_{1111}(\sin\phi_1 \sin\theta_1 + \rho_R \cos\phi_1 \cos\theta_1) \\ & + 3E_p^2E^*_{S_2}\chi^{NR}_{1111}(\sin\phi_1 \sin\theta_1 + \rho_{NR} \cos\phi_1 \cos\theta_1)\,. \end{aligned} \tag{3.2}$$

Obviously, $P_{2\perp}$ is much larger than the resonant signal $P_{1\perp}$, assuming $E_{S_1} = E_{S_2}$. The detected IP-CARS signal (P_{Det}) resulting from the interference between the two projections, $P_{1\perp}$ and $P_{2\perp}$, along the direction of the analyzer, is thus given by

$$\left|P_{Det}\right|^2 = \left|P_{1\perp}\right|^2 + \left|P_{2\perp}\right|^2 + 2\left|P_{1\perp}\right|\left|P_{2\perp}\right|\cos\varphi, \tag{3.3}$$

where the angle φ is the phase difference between the two CARS fields generated by

the two Stokes beams associated with the strong pump beam. The last term in Eq. (3.3), $2|P_{1\perp}||P_{2\perp}|\cos\varphi$, represents an interferometric mixing between the two CARS signals from the same sample. By changing the phase difference periodically between the two interference CARS signals, the detected signal from the interferometric term will be modulated in a cosine function. Hence, measuring the peak-to-peak intensity of this modulated interference signal will give the value of $4|P_{1\perp}||P_{2\perp}|$, which is also termed as interferometric polarization CARS (IP-CARS) signal. The advantages of this novel IP-CARS microscopy are that both the high signal level of the conventional CARS imaging and the high vibrational contrast of the conventional P-CARS imaging can be achieved for molecular vibrational imaging.

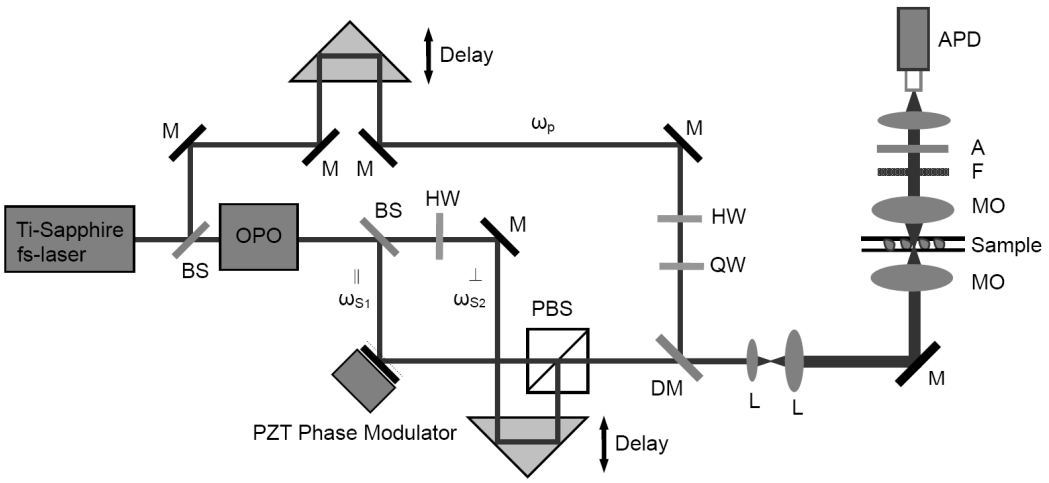

Fig. 3.2 Schematic of the interferometric polarization CARS (IP-CARS) microscope. The pump beam and the two perpendicularly polarized Stokes beams are collinearly focused onto the sample for generating two CARS signals simultaneously. ω_p, ω_{S1}, and ω_{S2} represent the pump field, the first and the second Stokes fields, respectively. The symbols "||" and "⊥" indicate parallel and perpendicular polarizations, respectively. BS, beam splitter; M, mirror; HW, half-wave plate; QW, quarter-wave plate; PBS, polarizing beam splitter; DM, dichroic mirror; L, lens; MO, microscope objective; A, polarization analyzer; F, filter set (combination of a short-pass filter cut-off at 700 nm and a band-pass filter centered at 660 nm with FWHM 80 nm); APD, avalanche photodiode.

3.1.1.2 Experiment

Fig. 3.2 shows the IP-CARS microscope system developed. The output of a femtosecond Ti:Sapphire laser (wavelengths tunable from 700 to 1000 nm; 120 fs pulses; a repetition rate of 76 MHz; horizontal polarization; Mira 900, Coherent Inc.) was divided into two parts by a beam splitter. One of the laser beams worked as the pump beam, and the other beam was used to pump an optical parametric oscillator (OPO) (wavelengths tunable from 1100 nm to 1600 nm, Coherent Inc.) to produce the Stokes beam for CARS microscopy. The Stokes beam from OPO was split into two equal beams (i.e., first and second Stokes beams) by a 50/50 beam splitter. To achieve the maximum vibrational contrast, the polarization directions of the pump and the second Stokes beams were rotated by 71.6^{o} and 90^{o} clockwise, respectively, relative to the horizontal polarization of the first Stokes beam using half-wave plates. The two perpendicularly polarized Stokes beams were combined together through a polarizing beam splitter, and then combined collinearly with the pump beam through a dichroic mirror. The three collinear laser beams were then focused onto the sample by a microscope objective (UPlanSApo 40×, N.A. 0.9, Olympus) for CARS generations. Temporal overlap between the three laser pulses at the sample was achieved by the two adjustable beam delay lines along the pump and Stokes light paths. Thus, two sets of CARS signals could be generated simultaneously from the same focal volume in the sample, including a relatively weak P-CARS signal $P_{1\perp}$ (resonant component), and a strong CARS signal $P_{2\perp}$ (including both resonant and nonresonant components). The CARS signals were collected by another objective (UPlanSApo 20×, N.A. 0.75, Olympus) and detected by an avalanche photodiode (SPCM-AQR-12, PerkinElmer)

through the filter set and the polarization analyzer. Along the polarization direction of the analyzer (Fig. 3.1), the two CARS signals arising from the same focal volume will interfere with each other. A homemade piezoelectric transducer (PZT) phase modulator was applied to apply an ~180^{o} phase modulation at 5 KHz to the first Stokes beam, hence the phase difference between the two interference CARS signals will also be modulated accordingly. Then complete constructive or destructive interference patterns of the two CARS signals was obtained. Measuring the peak-to-peak intensity ($4|P_{1\perp}||P_{2\perp}|$) of the periodically modulated interference CARS signal during the scanning of the sample, the background-free and intensity-amplified CARS images could be acquired.

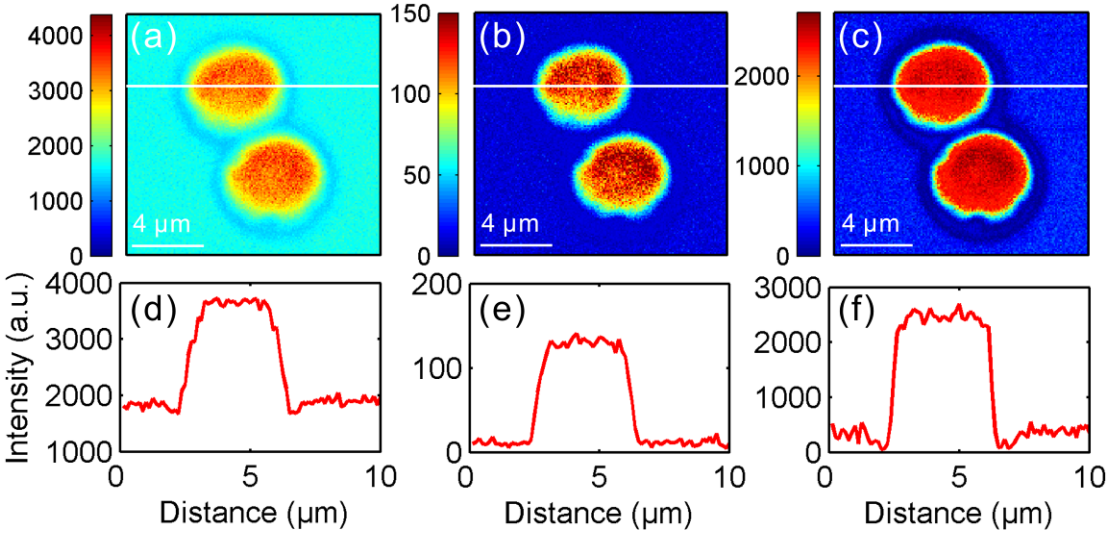

Fig. 3.3 Comparison of CARS images at vibrational frequency of 3054 cm^{-1} of 4.69-μm polystyrene beads immersed in water: (a) conventional CARS; (b) conventional P-CARS; and (c) IP-CARS. Figs. (d, e, f) are the corresponding intensity profiles across the lines indicated in the images (a, b, c), respectively. The average powers of the pump beam (835 nm) and Stokes beam (1121 nm) on the sample are 2 mW and 0.5 mW, respectively.

3.1.1.3 Results and Discussions

Fig. 3.3 shows the CARS images of 4.69-μm polystyrene beads immersed in water

from (a) conventional CARS, (b) conventional P-CARS, and (c) IP-CARS, respectively. The corresponding intensity profiles across the lines indicated in the CARS images (Figs. 3.3(a-c)) were shown in Figs. 3.3(d-f), respectively. Although the conventional CARS imaging provided a relatively intense signal (Figs. 3.3(d)), a large nonresonant background from the beads and the surrounding water was also present, resulting in a poorer signal-to-background image contrast (~2:1). The P-CARS image (Fig. 3.3(b)) shows a high signal-to-background ratio (~12:1), confirming its ability for effective suppression of nonresonant background. However, the P-CARS intensity was 25 times weaker than the conventional CARS, limiting its sensitivity in vibrational imaging. In contrast, the IP-CARS imaging (Fig. 3.3(c)) provided a high signal-to-background ratio (~11:1) by significantly suppressing the background signals while still remained a high vibrational contrast by amplifying the CARS signal of up to 20 times compared to the P-CARS.

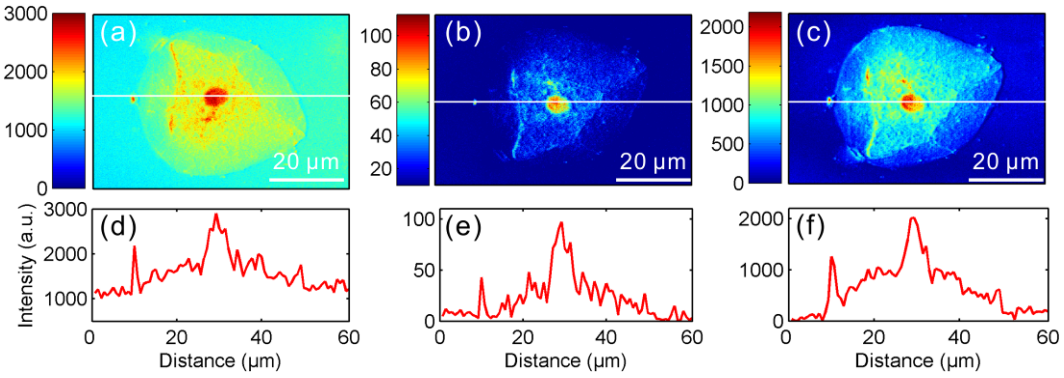

Fig. 3.4 CARS images (aliphatic C-H stretching vibration at 2870 cm^{-1}) of an unstained human epithelial cell in an aqueous environment: (a) conventional CARS; (b) P-CARS; and (c) IP-CARS. Figs. (d, e, f) are the corresponding intensity profiles across the lines indicated in the images (a, b, c), respectively. The average powers of the pump beam (835 nm) and Stokes beam (1098 nm) on the cell are 1.6 mW and 0.4 mW, respectively.

The capability of IP-CARS technique for cells imaging was also demonstrated. Fig. 3.4 shows an example of CARS images of an unstained human epithelial cell in aqueous environments for (a) conventional CARS, (b) P-CARS and (c) IP-CARS, respectively. The corresponding intensity profiles were displayed in Figs. 3.4(d-f). The conventional CARS image of epithelial cells (Fig. 3.4(a)) suffered from a poor vibrational contrast (~1.5:1) due to the relatively large nonresonant background from the aqueous environment (Fig. 3.4(d)). The P-CARS image (Fig. 3.4(b)) showed a high vibrational contrast (~11:1), but had a severe attenuation of resonant CARS signals. This led to a difficulty identifying some intracellular structures with weak CARS signals in P-CARS imaging (Fig. 3.4(e)). In contrast, the IP-CARS imaging (Fig. 3.4(c)) possessed not only a high vibrational contrast (~10:1), but also high signal levels (Fig. 3.4(f)) for revealing detailed biochemical distributions inside the intracellular structure of unstained epithelial cells with chemical specificity. Hence, the IP-CARS microscopy yielded an approximately 6-fold improvement in signal-to-background ratio compared to the conventional CARS microscopy, which was particularly useful for probing biomolecules at lower concentrations with high contrast.

One notes that since IP-CARS signal depends on the nonresonant signal that may be heterogeneous across the sample, the IP-CARS method has a limitation in direct quantitative analysis. However, this IP-CARS system developed has the ability of acquiring the above three different CARS images in tandem, the quantitative information of the samples thus can be readily recovered by processing the IP-CARS

($I_{IP\text{-}CARS}$) and conventional CARS images using the algorithm $I_{IP\text{-}CARS}^2/16|P_{2\perp}|^2$. In IP-CARS microscopy, since the interference CARS signal arises from exactly the same phase fronts of the mixing fields in the focal volume, the complete constructive or destructive interference of the two CARS fields may still be achievable even from highly scattering samples. On the other hand, applying the spectral shaping technique with gratings or prisms [183], the femtosecond laser pulses (broadband: ~100 cm^{-1}) used in this study can be stretched to the picosecond pulses of which the bandwidth matches with the Raman linewidth (~10 cm^{-1}) of biomolecules for optimizing the CARS signal excitation with improved spectral resolution and minimized nonresonant background (i.e., an improvement of resonant to nonresonant ratio of over 10 times) [25], it is anticipated that the picosecond-based IP-CARS can further improve the signal-to-background ratio up to 10 times compared to the current femtosecond-excited IP-CARS system.

3.1.1.4 Summary

An interferometric polarization CARS (IP-CARS) microscopy was developed that permitted effective suppression of the nonresonant background for high vibrational contrast imaging. The IP-CARS technique was applied for live cell imaging and it offered the potential for detecting weak signals of various biochemical species in biological systems for higher-contrast, molecular vibrational imaging.

3.1.2 Phase-controlled P-CARS

In the IP-CARS technique presented above, a fast phase modulator and lock-in heterodyne detection are necessarily involved. A simplified method sharing the similar

scheme with IP-CARS to avoid the use of phase modulator was proposed and demonstrated in this section to make the system low-cost and easy-to-operate. Based on the nonlinear interferometric technique, a phase-controlled polarization CARS microscopy for high sensitive and high contrast vibrational imaging was demonstrated. By changing the phase difference between the two CARS signals (i.e., a weak resonant CARS and a strong nonresonant CARS signal) simultaneously generated from the same focal volume of the sample, it was convenient to acquire the complete constructive (in-phase) and destructive (out of phase) interference CARS images of the sample. It was demonstrated that the nonresonant background could be effectively removed by digitally subtracting the destructive interference image from the constructive interference image.

3.1.2.1 Principle

In the phase-controlled P-CARS microscopy proposed, the pump field E_p is linearly polarized along the x-axis, while the Stokes field E_{S1} is linearly polarized with an angle φ relative to the pump field E_p. The x and y components ($P_{1x}^{(3)nr}$ and $P_{1y}^{(3)nr}$) of the nonresonant part ($P_1^{(3)nr}$) of the induced third-order nonlinear polarization can be written as [41]:

$$P_{1x}^{(3)nr} = 3\chi_{1111}^{(3)nr} E_P^2 E_{S1}^* \cos\varphi , \tag{3.4.1}$$

$$P_{1y}^{(3)nr} = 3\chi_{2112}^{(3)nr} E_P^2 E_{S1}^* \sin\varphi . \tag{3.4.2}$$

Hence, $P_1^{(3)nr}$ is linearly polarized with an angle, θ, relative to the x-axis,

$$\mathrm{P}_1^{(3)nr} = 3\chi_{1111}^{(3)nr} E_P^2 E_{S1}^* \cos\varphi / \cos\theta . \tag{3. 5}$$

Here, the angle θ is related with φ by

$$\tan\theta = \rho_{nr}\tan\varphi, \tag{3.6}$$

where $\rho_{nr} = \chi^{(3)nr}_{2112} \Big/ \chi^{(3)nr}_{1111}$ is defined as the nonresonant CARS depolarization ratio and assumed to be 1/3, followed by the Kleinman's symmetry assumption [42].

Similarly, the x and y components ($P^{(3)r}_{1x}$ and $P^{(3)r}_{1y}$) of the resonant part, $P^{(3)r}_{1}$, of the third-order nonlinear polarization are expressed as,

$$P^{(3)r}_{1x} = 3\chi^{(3)r}_{1111}E^2_P E^*_{S1}\cos\varphi, \tag{3.7.1}$$

$$P^{(3)r}_{1y} = 3\chi^{(3)r}_{2112}E^2_P E^*_{S1}\sin\varphi. \tag{3.7.2}$$

Due to the fact that the resonant component of the induced polarization is polarized in the direction different from that of the nonresonant counterpart, the nonresonant component can be readily removed by placing a polarization analyzer perpendicular to the nonresonant polarization component, and thus the amplitude of the resonant CARS field along the analyzer can be written as,

$$\mathrm{P}_{1\perp} = 3\chi^{(3)r}_{1111}E^2_p E^*_{S1}(\cos\varphi\sin\theta - \rho_r\sin\varphi\cos\theta). \tag{3.8}$$

Here, $\rho_r = \chi^{(3)r}_{2112} \Big/ \chi^{(3)r}_{1111}$ is the resonant CARS depolarization ratio. In order to achieve the maximum vibrational contrast, the angle φ should be set at 71.6°, and accordingly θ has a value of 45°. Obviously, the background-free CARS signal of $\mathrm{P}_{1\perp}$ is only a very small fraction of $\mathrm{P}^{(3)r}_{1}$ in intensity, thus the conventional P-CARS microscopy suffers from a severe reduction in intensity.

To tackle the P-CARS limitation in sensitivity, the nonlinear interferometric technique was employed to amplify the CARS signal for high sensitive and high contrast P-CARS imaging. For this purpose, a second Stokes field E_{S2} with the

polarization perpendicular to E_{S1} to avoid the mutual interference between them is introduced. The x and y components ($P_{2x}^{(3)}$ and $P_{2y}^{(3)}$) of the third-order nonlinear polarization $P_2^{(3)}$ (including both the resonant and nonresonant components) generated by the second Stokes field associated with the strong pump field E_p are given by

$$P_{2x}^{(3)} = 3(\chi_{1111}^{(3)r} + \chi_{1111}^{(3)nr})E_P^2 E_{S2}^* \sin\varphi, \tag{3.9.1}$$

$$P_{2y}^{(3)} = -3(\chi_{2112}^{(3)r} + \chi_{2112}^{(3)nr})E_P^2 E_{S2}^* \cos\varphi. \tag{3.9.2}$$

Hence, the projection of $P_2^{(3)}$ on the analyzer, $P_{2\perp}$, is written as

$$\begin{aligned} P_{2\perp} = {} & 3E_p^2 E_{S2}^* \chi_{1111}^{(3)r}(\sin\varphi\sin\theta + \rho_r \cos\varphi\cos\theta) \\ & + 3E_p^2 E_{S2}^* \chi_{1111}^{(3)nr}(\sin\varphi\sin\theta + \rho_{nr} \cos\varphi\cos\theta). \end{aligned} \tag{3.10}$$

Comparing Eqs. (3.8) and (3.10), it is evident that $P_{2\perp}$ is much larger than $P_{1\perp}$, assuming $E_{S1} = E_{S2}$. The detected CARS signal (I_{Det}) resulting from the interference between the two projections $P_{1\perp}$ and $P_{2\perp}$ along the polarization direction of the analyzer (Fig. 3.1) is thus given by Eq. (3.3). By controlling the phase difference ϕ between the two CARS fields ($P_{1\perp}$ and $P_{2\perp}$), the complete constructive interference (in-phase) CARS signal ($I_{\max}$), and the destructive interference (out of phase) CARS signal ($I_{\min}$) can be obtained, respectively,

$$I_{\max} = |P_{1\perp}|^2 + |P_{2\perp}|^2 + 2|P_{1\perp}||P_{2\perp}|, \tag{3.11.1}$$

$$I_{\min} = |P_{1\perp}|^2 + |P_{2\perp}|^2 - 2|P_{1\perp}||P_{2\perp}|. \tag{3.11.2}$$

By digital subtraction between the constructive and destructive interference images acquired, the phase-controlled P-CARS signal (I_{pc}) is thus equal to:

$$
\begin{aligned}
I_{pc} &= I_{\max} - I_{\min} = 4\left|P_{1\perp}\right\|P_{2\perp}\right| \\
&= 36\left|\chi_{1111}^{(3)r}E_p^2E_{S1}^*(\cos\varphi\sin\theta-\rho_r\sin\varphi\cos\theta)\right|\times \\
&\quad\left|E_p^2E_{S2}^*\chi_{1111}^{(3)r}(\sin\varphi\sin\theta+\rho_r\cos\varphi\cos\theta)+3E_p^2E_{S2}^*\chi_{1111}^{(3)nr}(\sin\varphi\sin\theta+\rho_{nr}\cos\varphi\cos\theta)\right|.
\end{aligned}
\tag{3.12}
$$

Hence, this novel phase-controlled P-CARS technique allows background-free detection with signal amplification. Both the advantages of the high signal level of conventional CARS imaging and the high vibrational contrast of P-CARS imaging can be attained using the phase-controlled P-CARS microscopy for molecular vibrational imaging.

3.1.2.2 Experiments

Fig. 3.5 shows the schematic of the phase-controlled P-CARS microscopy system. The output of a femtosecond Ti:sapphire laser (wavelengths tunable from 700 to 1000 nm; pulse duration of 120 fs; repetition rate of 76 MHz; horizontal polarization; Mira 900, Coherent Inc.) pumped by a Nd:YVO_4 laser (10 W Verdi, Coherent Inc.) was divided into two parts by a beam splitter [46]. One of the laser beams worked as the pump beam, and the other beam was used to pump an optical parametric oscillator (OPO) (wavelengths tunable from 1100 nm to 1600 nm, Coherent Inc.) to produce the Stokes beam for CARS microscopy. The Stokes beam from OPO was split into two equal beams (i.e., the first and the second Stokes beams) by a 50/50 beam splitter.

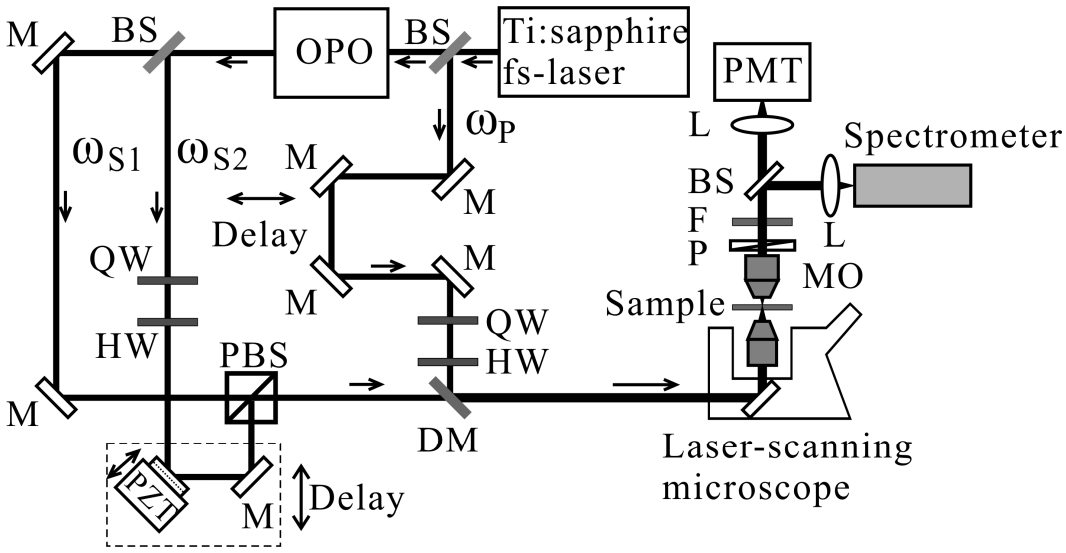

Fig. 3.5 Schematic of the phase-controlled polarization CARS microscope. Two perpendicularly polarized Stokes beams and the strong pump beam are combined collinearly and introduced into a laser-scanning confocal microscope for CARS imaging. ω_{S1}, ω_{S2} and ω_p stand for the central frequencies of the first and the second Stokes fields and the pump field, respectively. BS, beam splitter; HW, half-wave plate; QW, quarter-wave plate; PBS, polarizing beam splitter; DM, dichroic mirror; A, polarization analyzer; F, filter set (a short-pass filter cut-off at 700nm and a band pass filter centered at 650nm with FWHM 80nm); M, mirror; PMT, photomultiplier tube.

To achieve the maximum vibrational contrast, the polarization directions of the pump and the second Stokes beams were rotated by 71.6^o and 90^o clockwise, respectively, relative to the horizontal polarization of the first Stokes beam using half-wave plates. The two perpendicularly polarized Stokes beams were combined together through a polarizing beam splitter, and then combined collinearly with the pump beam through a dichroic mirror (LW-45-RU780-TU946, CVI). A quarter-wave plate was used to compensate the birefringent effect on the pump field introduced by the dichroic mirror. The three collinear laser beams were then coupled into a laser scanning confocal microscope (FV300, Olympus) and focused onto the sample by a microscope objective (UPlanSApo 40×, N.A. 0.9, Olympus) for CARS generations. Temporal overlap between the three laser pulses at the sample was achieved by the

adjustable beam delay lines along the pump light path. Thus, two sets of CARS signals could be generated simultaneously from the same focal volume in the sample, including a relatively weak P-CARS signal $P_{1\perp}$ (resonant component), and a strong CARS signal $P_{2\perp}$ (including both resonant and nonresonant components). The CARS signals were collected by a condenser (UPlanSApo 20×, N.A. 0.75, Olympus) and detected by photomultiplier tube (PMT) (R3896, Hamamatsu) through the filter set and the polarization analyzer. Another beam splitter was placed before the PMT to allow the simultaneously forward CARS imaging and the CARS spectra measurements by a spectrometer (HR4000, Ocean Optics Inc., Dunedin, FL). Along the polarization direction of the analyzer (Fig. 3.1), the two CARS signals arising from the same focal volume would interfere with each other. Digitally controlled voltages was applied to a homemade piezoelectric transducer (PZT) phase modulator to create an 0~180^{o} phase modulation to the first Stokes beam, and hence the phase difference between the two interference CARS signals would also be controlled accurately. Then the complete constructive (in-phase) or destructive (out of phase) interference images of the two CARS signals was obtained. The phase-controlled P-CARS technique by employing a rapid digital subtraction between the constructive and destructive interference CARS images permitted the background-free and intensity-amplified P-CARS imaging.

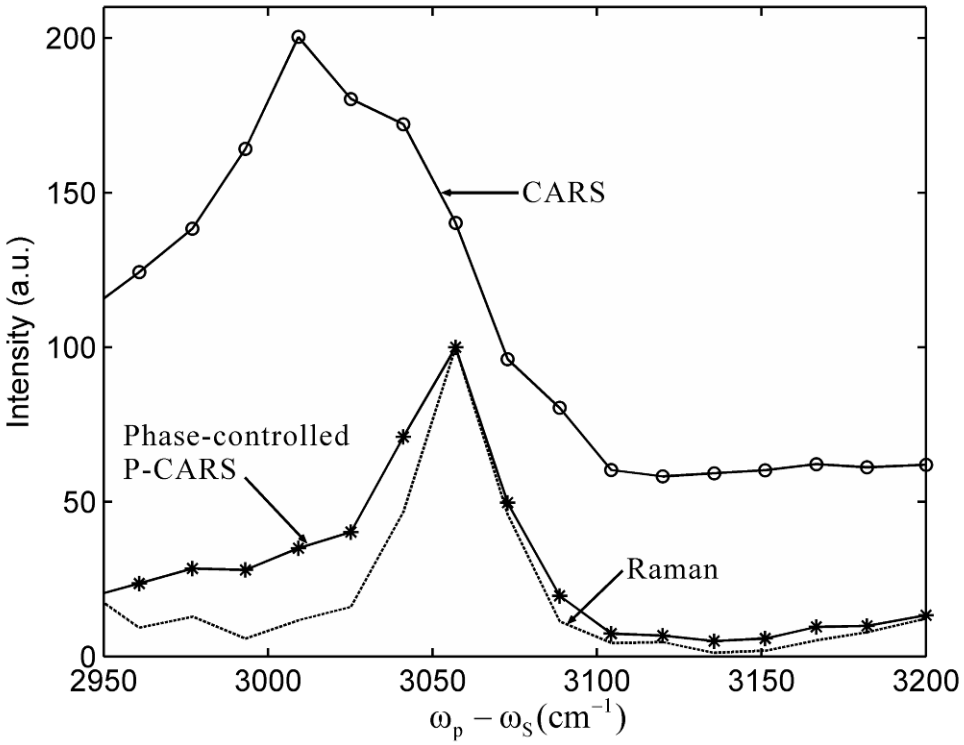

Fig. 3.6 Comparison of Raman spectrum and CARS spectra of a 1 μm polystyrene bead spin coated on a coverslip and covered in water, acquired under the conditions of conventional CARS and phase-controlled P-CARS, respectively. The pump frequency was fixed at 11933 cm^{-1}, while the Stokes frequency was tuned from 8733 to 8983cm^{-1}. The pump and Stokes powers on the sample were 2 and 0.5 mW, respectively. The Raman spectrum is recorded using a micro-Raman spectrometer system (inVia, Renishaw, UK).

3.1.2.3 Results and Discussion

Fig. 3.6 shows the Raman spectrum and CARS spectra of a 1 μm polystyrene bead immersed in water acquired from the conventional CARS and phase-controlled P-CARS, respectively. Compared with the Raman spectrum, the conventional CARS spectrum displayed a dispersive lineshape with an apparent frequency shift in the vibrational resonance that arises from the interference between the resonant and nonresonant signals. A large nonresonant background from water and the bead was also present in the conventional CARS signal, limiting the spectral selectivity for CARS imaging. In contrast, the phase-controlled CARS spectrum showed a similar

spectral lineshape to the Raman spectrum, and yielded a high signal-to-background ratio, illustrating its advantage for effective suppression of the nonresonant signal from the beads and water for high contrast vibrational imaging.

Fig. 3.7 shows the changes of the detected CARS signal (aromatic C-H stretching vibration at 3054 cm^{-1}) of a 1 μm polystyrene bead immersed in water against the voltage applied to the PZT. By increasing the PZT voltage (e.g., from 102 to 115 V), the phase difference between the two CARS signals for interference can be changed up to 360°. It is observed that the detected CARS signals followed a cosine function with a periodic appearance of maxima or minima in intensity by changing the phase difference (i.e., voltage). For instance, in the phase-controlled CARS microscope system, a maximum CARS signal I_{max} (i.e., constructive interference) and a minimal CARS signal I_{min} (i.e., destructive interference) could be obtained when applying the voltage to the PZT at 114 and 108 V, respectively,

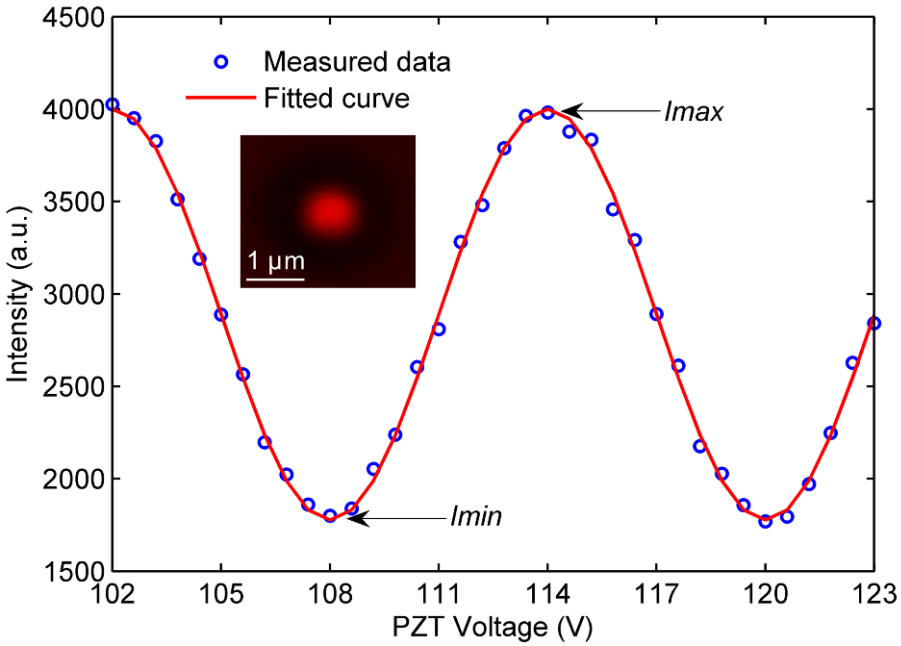

Fig. 3.7. The phase-controlled P-CARS signal of a 1 μm polystyrene bead as a function of voltages applied to the PZT.

Figure 3.8 shows the CARS images of 1 μm polystyrene beads immersed in water for (a) constructive interference, (b) destructive interference, (c) phase-controlled P-CARS, and (d) conventional P-CARS, respectively. The corresponding intensity profiles across the lines indicated in the CARS images (Figs. 3.8(a-d)) were shown in Figs. 3.8(e-h), respectively. The CARS intensities in the constructive interference image (Fig. 3.8(a)) were greatly enhanced (~4000 counts, Fig. 3.8(e)), while the CARS intensities in the destructive interference image (Fig. 3.8(b)) were much reduced (~1800 counts, Fig. 3.8(f)). With a simple digital subtraction between the constructive and destructive interference images, the nonresonant background contribution to the CARS signal could mostly be removed, as reflected in the phase-controlled CARS imaging (Figs. 3.8(c, g)). Compared to the P-CARS imaging (Fig. 3.8(d)), the phase-controlled CARS technique showed a similar higher vibrational contrast (signal-to-background ratio of 10-12:1), while providing an approximately 20-fold improvement in intensity for molecular imaging. Further studies showed that phase-controlled CARS method offered at least 5-fold improvements in imaging contrast compared with conventional CARS imaging (vibrational contrast of ~1.5-2:1). The above results confirmed the capability of the phase-controlled CARS technique for effective suppression of the nonresonant background while also significantly amplifying the resonant signal, thereby realizing high sensitive and high contrast vibrational imaging.

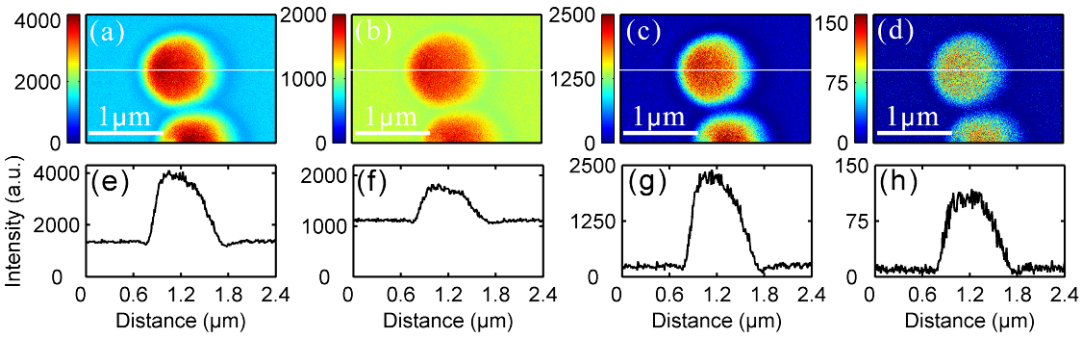

Fig. 3.8 Comparison of CARS images (aromatic C-H stretching vibration at 3054 cm^{-1}) of 1 μm polystyrene beads immersed in water for (a) constructive interference image, (b) destructive interference image, (c) difference between the images (a) and (b) (i.e., phase-controlled P-CARS image), and (d) conventional P-CARS image. Figs. (e, f, g, h) are the corresponding intensity profiles across the lines indicated in the images (a, b, c, d), respectively. The average powers of the pump beam (838 nm) and the Stokes beam (1126 nm) on the sample are 2 mW and 0.5 mW, respectively, at the repetition rate of 76 MHz.

The applicability of the phase-controlled P-CARS technique for cell imaging was also demonstrated. Fig. 3.9 shows an example of CARS images (aliphatic C-H stretching vibration at 2870 cm^{-1}) of unstained human epithelial cells in aqueous environments for (a) constructive interference, (b) destructive interference, (c) phase-controlled P-CARS, and (d) conventional P-CARS, respectively. The corresponding intensity profiles along the lines were displayed in Figs. 3.9(e-h). Clearly, the phase-controlled P-CARS imaging on epithelial cells gave a much higher signal-to-background ratio (of 10:1, similar to the P-CARS imaging (Figs. 3.9(d, h)) that was 5-fold higher than the conventional CARS (vibrational contrast of ~1.5-2:1, Figs. 3.10(a, c)). Again, there was an approximately 20-fold improvement in CARS intensity using the phase-controlled CARS microscopy compared with the P-CARS microscopy. Due to the much amplified CARS signals observed together with high signal-to-background ratios, phase-controlled P-CARS revealed more detailed

information about the biomolecular distributions in the cells (Figs. 3.9(c, g)), which were barely visible using conventional P-CARS (Figs. 3.9(d, h)). Hence, phase-controlled CARS method would be particularly useful for probing biomolecules of biological/biomedical systems at a lower concentration.

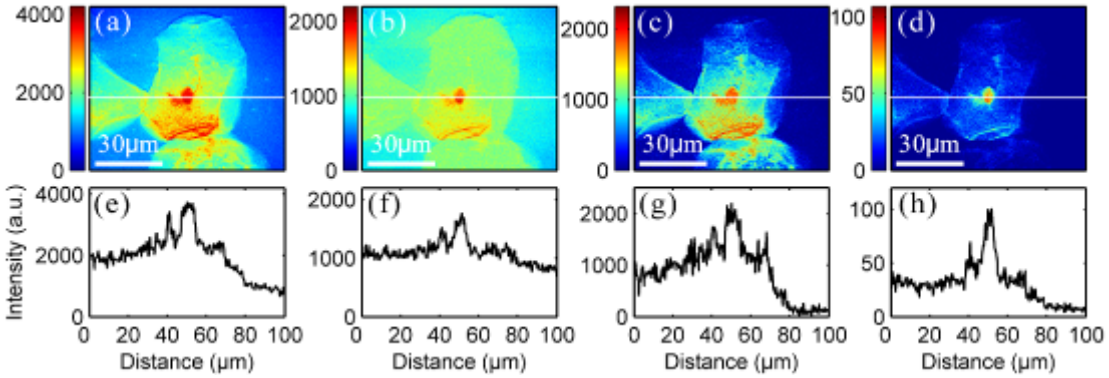

Fig. 3.9 CARS images (aliphatic C-H stretching vibration at 2870 cm^{-1}) of unstained human epithelial cells in aqueous environments: (a) constructive interference image, (b) destructive interference image, (c) phase-controlled P-CARS image, and (d) conventional P-CARS image. Figs. (e, f, g, h) are the corresponding intensity profiles across the lines indicated in the images (a, b, c, d), respectively. The average powers of the pump beam (838 nm) and the Stokes beam (1103 nm) on the sample are 1.8 mW and 0.4 mW, respectively, at the repetition rate of 76 MHz.

Since the phase-controlled P-CARS signal is dependent on the large nonresonant signal that may be heterogeneous across the sample, this method may have a limitation in direct quantitative analysis. However, the phase-controlled P-CARS microscope developed has ability of acquiring the constructive and destructive interference CARS images for rapid phase-controlled P-CARS imaging (Fig. 3.9(c)), the P-CARS (Fig. 3.9(d)), and the conventional CARS (Fig. 3.10(a)) in tandem, the vibrational modes quantification of the sample can be readily realized using the $I_{pc}^2/16P_{2\perp}^2$ as shown in Fig. 3.10(b). Clearly, the processed image shares the similar higher vibrational contrast (a signal-to-background ratio of 12:1) with P-CARS imaging (Fig. 3.9(d)).

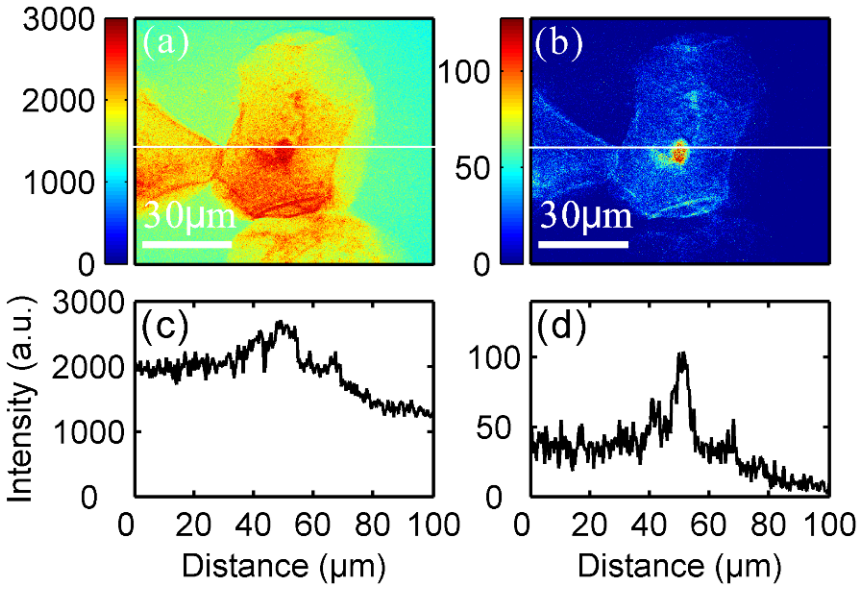

Fig. 3.10 CARS images (aliphatic C-H stretching vibration at 2870 cm^{-1}) of unstained human epithelial cells in aqueous environments: (a) the conventional CARS due to the induced polarization P_{2L}, and (b) the processed CARS image through calculation by dividing the square of the phase-controlled CARS image by the conventional CARS image for vibrational modes quantification. Figs. (c, d) are the corresponding intensity profiles across the lines indicated in the images (a, b), respectively.

Furthermore, in the phase-controlled P-CARS microscopy, the two interference CARS signals arise from exactly the same phase fronts of the mixing fields within the same excitation focal volume of the sample, and thus, the complete constructive or destructive interference of the two CARS fields may still be achievable even from highly scattering samples. A slight drop in the signal-to-background ratio of the phase-controlled P-CARS image compared with the conventional P-CARS is probably due to the fact that the nonresonant background in the P-CARS signal cannot be totally removed because of the limited extinction ratios of the excitation fields as well as the birefringence effect of the dichroic mirror on the polarized light fields, resulting in the leaked residual nonresonant background to be detected and amplified by the phase-controlled CARS microscope system. Note that similar to the P-CARS

microscopy, the ability of suppressing the nonresonant background using phase-controlled P-CARS microscopy is also affected by the depolarization effect of the samples investigated. Highly scattering turbid media (e.g., thick tissue) may limit the performance of background rejection by phase-controlled P-CARS technique.

3.1.2.4 Summary

A novel phase-controlled polarization CARS microscopy was developed that permitted effective removal of the nonresonant background while simultaneously remaining the detection sensitivity for molecular vibrational imaging. With the nature of nonlinear interferometry for generating greatly amplified resonant signals, the phase-controlled P-CARS technique could play a more active role than P-CARS microscopy in probing weak signals of certain biologically relevant molecules at lower concentrations in biological and biomedical systems.

3.1.3 Heterodyne polarization (HP-) CARS

3.1.3.1 Principle

Fig. 3.11 shows the principle of HP-CARS microscopy, in which the pump beam (E_p) is linearly polarized with an angle, ϕ_0, relative to the x-axis, and the Stokes beam (E_S) polarization is along with the angle, ϕ, with respect to the polarization direction of E_p. The projection components of the CARS signal (P), P_x and P_y, along the x- and y- axis, respectively, are written as

$$\begin{aligned} P_x = 3E_p^2 E_S^* [&\chi_{1111}^{nr}(\cos\phi\cos\phi_0 - \rho_{nr}\sin\phi\sin\phi_0) \\ &+ \chi_{1111}^{r}(\cos\phi\cos\phi_0 - \rho_r\sin\phi\sin\phi_0)], \end{aligned} \tag{3.13}$$

$$P_y = 3E_p^2 E_S^*[\chi_{1111}^{nr}(\cos\phi\sin\phi_0 + \rho_{nr}\sin\phi\cos\phi_0) + \chi_{1111}^{r}(\cos\phi\sin\phi_0 + \rho_r\sin\phi\cos\phi_0)]. \quad (3.14)$$

where χ_{1111}^{r} and χ_{1111}^{nr} are the resonant and nonresonant third-order nonlinear susceptibilities, respectively; ρ_r and ρ_{nr} are the resonant and nonresonant CARS depolarization ratios, respectively. In P-CARS microscope, ϕ is set to 71.6° for optimizing vibrational contrast, assumed that ρ_{nr} is 1/3 according to the Kleinman's symmetry condition.

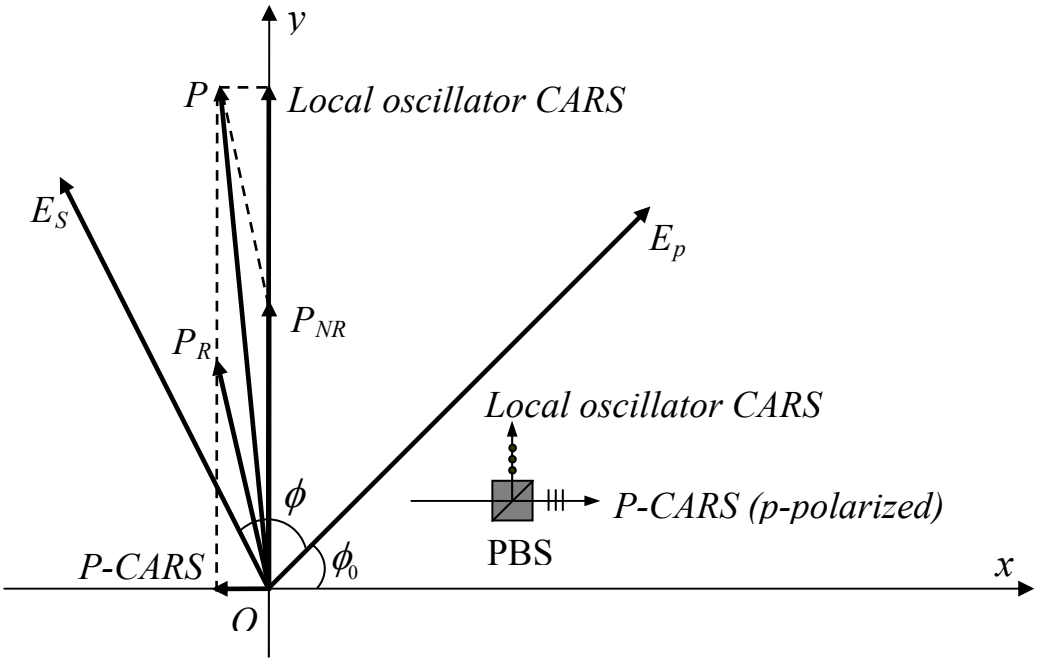

Fig. 3.11 Illustration of the polarization vectors for the pump (E_p) and Stokes (E_S) fields, and the CARS field (P) including the resonant (P_R) and nonresonant (P_{NR}) components in the heterodyne polarization (HP-CARS) microscope. The inset in the figure highlights the separation between the P-CARS and local oscillator-CARS fields by a polarizing beam splitter (PBS).

To make P_x as a pure resonant CARS field (P-CARS), the angle ϕ_0 is set at 45°, and thus, the P-CARS field is polarized in horizontal direction (x-axis) and can totally transmit through the polarizing beam splitter (PBS) as p-polarized component (Inset of Fig. 3.11). Concurrently, the perpendicularly polarized CARS field P_y (i.e., local

oscillator), which is composed of the total nonresonant and part of the resonant CARS signal, is reflected by the PBS to work as s-polarized component (inset of Fig 3.11). Using a half-wave plate, the polarization direction of the local oscillator field (P_y) is rotated by 90^o, and this local oscillator CARS is denoted as P_y' with polarization being parallel to the P-CARS. Hence, the intensity of the detected CARS signal, I_{Det}, resulting from the interference between the P-CARS (P_x) and the local oscillator (P_y'), is given by

$$I_{Det} = |P_x|^2 + |P_y'|^2 + 2|P_x||P_y'|\cos\varphi, \qquad (3.15)$$

where the angle, φ, is the phase difference between the P-CARS and local oscillator CARS fields. In Eq. (3.15), the first term, $|P_x|^2$, represents the P-CARS signal that can be used for vibration imaging with high contrast. However, the intensity of P-CARS usually is very weak due to the severe attenuation (Eq. (3.13)). The second term, $|P_y'|^2$, is the local oscillator CARS signal, which has much higher intensity than P-CARS, but this term contains the nonresonant background which is not suitable for high contrast imaging (Eq. (3.14)). The last term, $2|P_x||P_y'|\cos\varphi$, indicates an interferometric mixing between the two CARS fields. Since $|P_x|$ represents the pure resonant CARS field, while the local oscillator $|P_y'|$ has high amplitude, the product of $|P_x|$ and $|P_y'|$ thus can be used for vibration imaging with high contrast. By modulation of the phase difference between the two CARS fields, optical heterodyne detection on the interference CARS signal will give the value of $4|P_x||P_y'|$, which is also termed as heterodyne polarization CARS signal ($I_{HP\text{-}CARS}$). The implication for utilizing this novel HP-CARS microscopy is that both the advantages of high vibrational contrast of

the P-CARS method and high signal level of the local oscillator CARS can be achieved for molecular vibrational imaging.

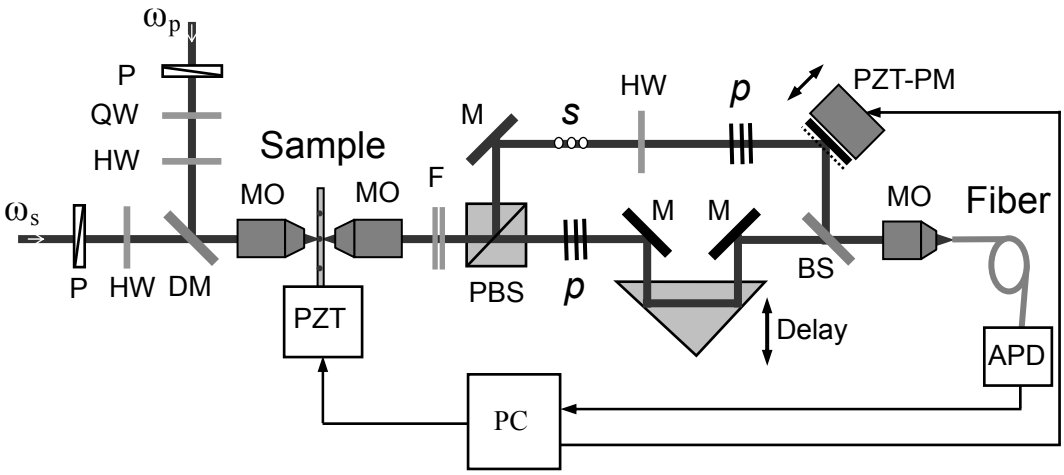

Fig. 3.12 Schematic of the HP-CARS microscope. The P-CARS and the local oscillator-CARS fields are separated by a PBS and introduced into a Mach-Zehnder interferometer for CARS interference. P, polarizer; QW, quarter-wave plate; HW, half-wave plate; DM, dichroic mirror; MO, microscope objective; F, filter sets; M, mirrors; PBS, polarizing beam splitter; PZT-PM, PZT-based phase modulator; APD, avalanche photodiode.

3.1.3.2 Experiment

Fig. 3.12 shows the schematic of the HP-CARS microscope developed. The output of a femtosecond Ti:Sapphire laser (wavelengths tunable from 700 to 1000 nm; pulse duration of 120 fs and spectral linewidth (FWHM) of ~8 nm; repetition rate of 76 MHz; horizontal polarization; Mira 900, Coherent Inc.) pumped by a Nd:YVO_4 laser (10-W Verdi, Coherent Inc.) was divided into two parts by a beam splitter [184]. One of the beams worked as the pump beam, and the other was used to pump an optical parametric oscillator (OPO) (wavelengths tunable 1100~1600 nm, Coherent Inc.) to produce the Stokes beam. The polarization directions of the pump and Stokes beams were rotated by 45^o and 116.6^o anticlockwise, respectively, using half-wave plates. The

quarter-wave plate positioned in the pump path was employed to compensate the birefringent effect introduced by the dichroic mirror. The extinction ratios of polarizations for both the pump and Stokes beams after passing through the two objectives and the sample were ~200:1, which had been proved to be sufficient for P-CARS detection. The pump and Stokes beams were combined collinearly on the dichroic mirror and then are focused by a microscope objective (UPlanSApo 40×, N.A. 0.9, Olympus) onto the sample for CARS generation. The generated CARS signal was collected and collimated by another microscope objective (UPlanSApo 20×, N.A. 0.75, Olympus) and then passed through a filter set (a short-pass filter, cut-off at 700 nm; and a band-pass filter centered at 660 nm with FWHM ~80 nm). The CARS signal generated from the sample was then split into two parts by a polarizing beam splitter (PBSH-450-1300-100, CVI). The local oscillator signal ($|P_y|^2$) (i.e., s-polarized component) was reflected, while the P-CARS ($|P_x|^2$) signal (i.e., p-polarized component) transmitted by the PBS. The two CARS signals were then sent into a Mach-Zehnder-type interferometer for interference, in which the local oscillator CARS polarization was rotated by 90^o using a half-wave plate such that its polarization was parallel to the P-CARS. Temporal overlap between the two CARS fields for interference was achieved by using an adjustable beam delay line along the P-CARS beam, while the phase difference between the two CARS fields was realized using a home-made PZT phase modulator that applies a ~180^o phase modulation to the local oscillator-CARS field. The two CARS beams were collinearly combined on a 50/50 beam splitter and picked up by a microscope objective (Plan N, 10×, N.A. 0.25,

Olympus), and then coupled into a 100-μm fiber for optical heterodyne detection using an avalanche photodiode (SPCM-AQR-12, PerkinElmer) associated with a signal processing system performed with LabView programming (Labview 8.0, N.I.). By modulating the phase difference between the local oscillator CARS and resonant CARS fields, complete constructive and destructive interference patterns of the two CARS fields could be observed. Measuring the heterodyne term ($4|P_x||P_y'|$) during the scanning of the sample, it was easy to acquire background-free but intensity-amplified CARS images.

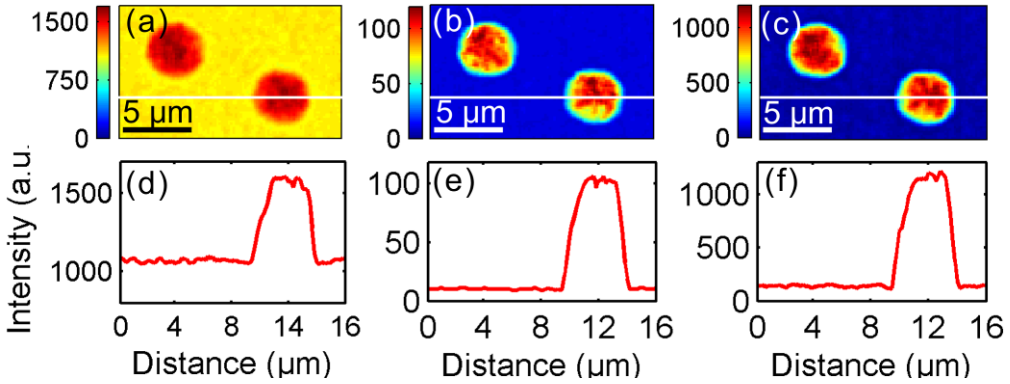

Fig. 3.13 Comparison of CARS images (aromatic C-H stretching vibration at 3054 cm^{-1}) of 4.69-μm polystyrene beads immersed in water for (a) local oscillator-CARS, (b) P-CARS, and (c) HP-CARS. Figs. (d, e, f) are the corresponding intensity profiles across the lines indicated in the images (a, b, c), respectively. The average powers of the pump beam (835 nm) and Stokes beam (1121 nm) on the sample are 0.6 mW, and 0.3 mW, respectively.

3.1.3.3 Results and Discussions

Fig. 3.13 shows the comparison of CARS images of 4.69-μm polystyrene beads immersed in water for (a) local oscillator-CARS, (b) P-CARS, and (c) HP-CARS. The corresponding intensity profiles across the lines indicated in the CARS images (Figs. 3.13(a-c)) were shown in Figs. 3.13(d-f), respectively. The local oscillator-CARS (Fig. 3.13(a)) suffered from a poor signal-to-background contrast (~1.5:1) due to a large

nonresonant background interference (~1050 counts in intensity), although it showed a relatively intense signal level (~1600 counts in intensity). The P-CARS image (Fig. 3.13(b)) gave a high vibrational contrast (~12:1), confirming its ability for effective suppression of nonresonant background (Fig. 3.13(e)). However, the P-CARS intensity was approximately 15 times weaker than the local oscillator-CARS, limiting its sensitivity in vibrational imaging. In contrast, the HP-CARS image (Fig. 3.13(c)) provided a high signal-to-background ratio (~11:1) by significantly suppressing the nonresonant background (~110 counts in intensity), while still remained a high signal intensity level (~1200 counts in intensity) by amplifying the CARS signal of up to 12 times compared to the P-CARS.

The utility of HP-CARS technique for better vibrational imaging of biological samples was also demonstrated. Fig. 3.14 shows an example of CARS images of an unstained human epithelial cell in aqueous environments for (a) local oscillator-CARS, (b) P-CARS and (c) HP-CARS, respectively. The corresponding intensity profiles were displayed in Figs. 3.14(d-f). Again, large nonresonant signals from the aqueous background and cells were present in local oscillator-CARS imaging (Fig. 3.14(a)), resulting in a poor image contrast (~1.5:1) (Fig. 3.14(d)). The P-CARS imaging (Fig. 3.14(b)) showed a high vibrational contrast (~11:1), but a severe attenuation of resonant CARS signal led to a difficulty in identifying some intracellular structures with weak signal responses (Fig. 3.14(e)). On the other hand, HP-CARS imaging (Fig. 3.14(c)) possessed not only a high vibrational contrast (~10:1), but also high signal levels for revealing more detailed intracellular structures of unstained epithelial cells

(Fig. 3.14(f)). Therefore, the HP-CARS microscopy offered an approximately 7-fold improvement in signal-to-background ratio compared to the local oscillator-CARS imaging, which was particularly useful for probing biomolecules at lower concentrations with high vibrational contrast.

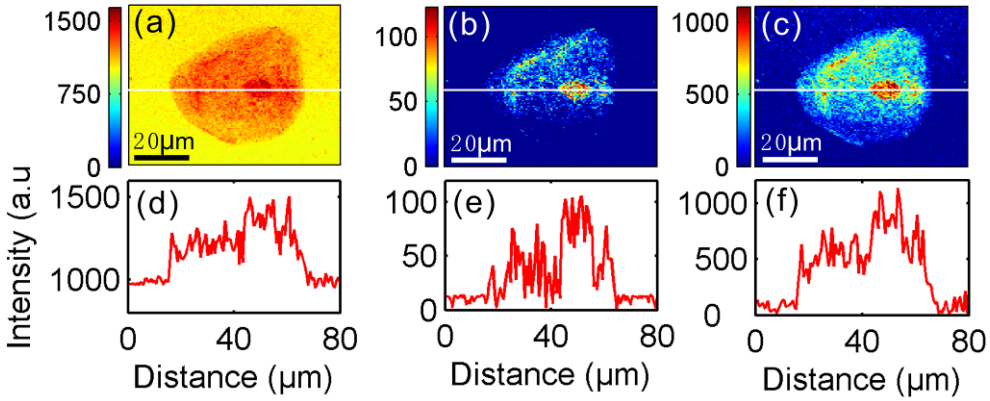

Fig. 3.14 CARS images of an unstained human epithelial cell (aliphatic C-H stretching vibration at 2870 cm^{-1}) in aqueous environments: (a) local oscillator-CARS, (b) P-CARS, and (c) HP-CARS. Figs. (d, e, f) are the corresponding intensity profiles across the lines indicated in the images (a, b, c), respectively. The average powers of the pump beam (835 nm) and Stokes beam (1098 nm) on the sample are 0.5 mW, and 0.3 mW, respectively.

Since the interference CARS signal arises from exactly the same phase fronts of the mixing fields within the same focal excitation volume, the complete constructive or destructive interference of the two CARS fields may still be achievable even from highly scattering samples in HP-CARS microscopy. One notes that HP-CARS signal is dependent on the nonresonant signal that may be heterogeneous across the sample. Therefore, the HP-CARS method has a limitation in direct quantitative analysis. However, the HP-CARS system developed has the ability of acquiring the three different CARS images (P-CARS, local oscillator-CARS, HP-CARS) in tandem, the quantitative information of the samples can be readily recovered using the algorithm $I_{HP\text{-}CARS}^2/16|P_y'|^2$). On the other hand, using the spectral shaping technique with

gratings or prisms, the femtosecond laser pulses (bandwidth: ~100 cm^{-1}) can be stretched to the picosecond pulses of which the bandwidth matches with the Raman linewidth (~10 cm^{-1}) of biomolecules for optimizing the CARS signal excitation with improved spectral resolution and minimized nonresonant background. Also, in terms of improvement of resonant to nonresonant ratio of over 10 times from femtosecond to picosecond pulses used in conventional CARS imaging, it is anticipated that the picosecond-based HP-CARS can further improve the signal-to-background ratio of up to 10 times compared to the current femtosecond-excited HP-CARS system.

3.1.3.4 Summary

In conclusion, a heterodyne-detected polarization CARS (HP-CARS) microscopy was demonstrated that permitted efficient suppression of nonresonant background while significantly improved the detection intensity level for high contrast vibrational imaging. HP-CARS microscopy could play a much active role than P-CARS, particularly for high contrast imaging on weak responses of certain biologically relevant molecules in tissues and cells.

3.2 Elliptically Polarized CARS for Intrinsic Nonresonant Background Suppression

3.2.1 Principle

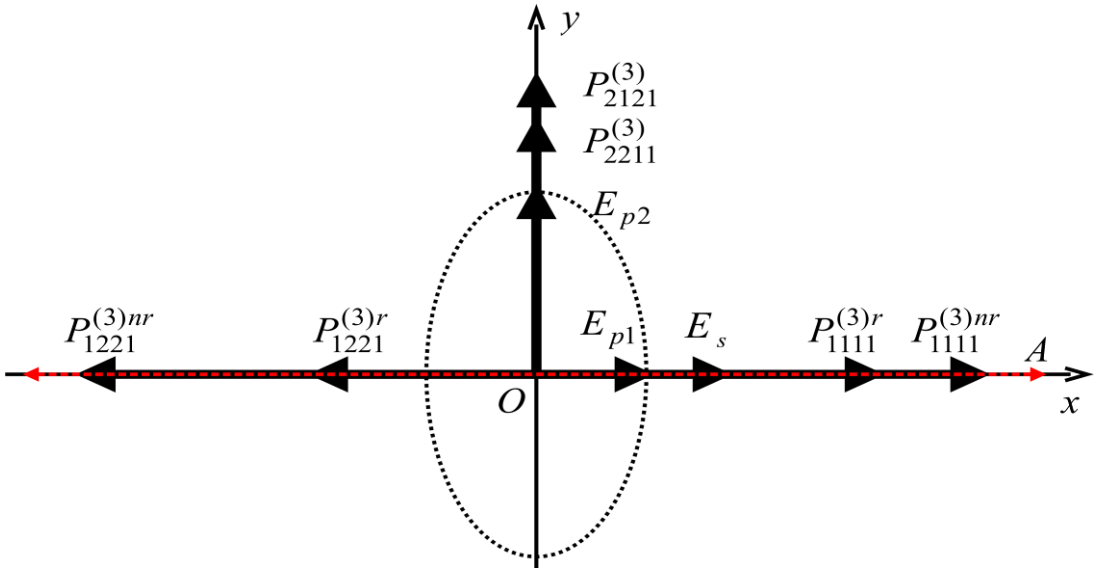

Fig. 3.15 Polarization vectors of the elliptically polarized pump field comprising the two linear components of E_{p1} and E_{p2}, the linearly polarized Stokes field E_s, and the generated CARS radiations ($P_{1221}^{(3)nr}$, $P_{1221}^{(3)r}$, $P_{1111}^{(3)nr}$, $P_{1111}^{(3)r}$, $P_{2211}^{(3)}$ and $P_{2121}^{(3)}$), as well as the orientation of the polarization analyzer (A) along the x-axis.

Fig. 3.15 shows the principle of the developed EP-CARS microscopic technique in which the pump field E_p is elliptically polarized, while the Stokes field E_s is linearly polarized along the x-axis. The elliptically polarized pump field used can be resolved into two linearly polarized components E_{p1} (x-polarization) and E_{p2} (y-polarization) in phase quadrature as follows [53]:

$$E_{p2} = \alpha E_{p1} e^{i\frac{\pi}{2}}, \tag{3.16}$$

where α is the aspect ratio of the ellipse determined by the amplitude ratio of the linear polarization component E_{p2} to the component E_{p1}. The induced third-order nonlinear polarization $P^{(3)}$ generated by the elliptically polarized pump field (E_{p1} and E_{p2}) associated with the Stokes beam E_s comprises the x-component $P_x^{(3)}(P_{1111}^{(3)nr}, P_{1111}^{(3)r}, P_{1221}^{(3)nr}, P_{1221}^{(3)r})$, and the y-component $P_y^{(3)}(P_{2211}^{(3)}, P_{2121}^{(3)})$. To remove the

component $P_y^{(3)}$, a polarization analyzer is oriented perpendicularly to the y-axis, and thus only the x-component $P_x^{(3)}$ of CARS radiations is allowed to pass through the analyzer (Fig. 3.15), which can be expressed as,

$$\begin{aligned} P_x^{(3)} &= P_{1111}^{(3)nr} + P_{1111}^{(3)r} + P_{1221}^{(3)nr} + P_{1221}^{(3)r} \\ &= 3\chi_{1111}^{(3)nr} E_{p1} E_{p1} E_s^* + 3\chi_{1111}^{(3)r} E_{p1} E_{p1} E_s^* + 3\chi_{1221}^{(3)nr} E_{p2} E_{p2} E_s^* + 3\chi_{1221}^{(3)r} E_{p2} E_{p2} E_s^*. \end{aligned} \tag{3.17}$$

By substituting Eq. (3.16) into Eq. (3.17), the induced nonlinear polarization $P_x^{(3)}$ is rewritten as,

$$P_x^{(3)} = 3[(1-\rho_{nr}\alpha^2)\chi_{1111}^{(3)nr} + (1-\rho_r\alpha^2)\chi_{1111}^{(3)r}]E_{p1}E_{p1}E_s^*. \tag{3.18}$$

Here $\rho_r (= \chi_{1221}^{(3)r} / \chi_{1111}^{(3)r})$ is the depolarization ratio of resonant CARS, whereas $\rho_{nr} (= \chi_{1221}^{(3)nr} / \chi_{1111}^{(3)nr} \approx 1/3)$ is the depolarization ratio of nonresonant CARS following the Kleinman's symmetry. To remove the nonresonant component (first term in Eq. (3.18)), the amplitude ratio α of the elliptically polarized pump field is set at $1/\sqrt{\rho_{nr}} (= \sqrt{3})$, and then the nonresonant signals arising from the two nonresonant polarizations $P_{1111}^{(3)nr}$ and $P_{1221}^{(3)nr}$ (with the same amplitudes but in opposite phase) will cancel out due to their complete destructive interference with each other. The resulting elliptically polarized CARS signal ($I_{EP-CARS}$) which represents pure resonant CARS is as follows:

$$I_{EP-CARS} \propto \left|P_x^{(3)}\right|^2 = 9\left|(1-3\rho_r)\chi_{1111}^{(3)r} E_{p1} E_{p1} E_s^*\right|^2. \tag{3. 19}$$

Therefore, this so-called elliptically polarized CARS (EP-CARS) microscopy technique can realize background-free vibrational imaging. If employing the same excitation powers of linearly polarized pump and Stokes light fields as used in the

EP-CARS microscopy, and also consider the conditions of $|E_p| = 2|E_{p1}|$, $\phi = 71.6^\circ$ and $\theta = 45^\circ$, the normal P-CARS signal (I_{P-CARS}) can be expressed as:

$$I_{P-CARS} \propto \left|3E_p^2 E_s^* \chi_{1111}^{(3)r}(\cos\phi\sin\theta - \rho_r \sin\phi\cos\theta)\right|^2 = 0.8 I_{EP-CARS} \quad (3.20)$$

Obviously, the EP-CARS microscopy has a 1.25-fold improvement in signal level than normal P-CARS microscopy [84]. It should be pointed out that both the EP-CARS and the P-CARS techniques are workable only when the resonant depolarization ratio ρ_r of the Raman-active molecular vibration is not equal to 1/3 (i.e., $\rho_r \neq \rho_{nr}$).

3.2.2 Experiment

In this experiment, the pump and the Stokes fields were the two inherently synchronized 120 fs pulse trains [46, 122, 184]. The linearly polarized pump beam from the laser was converted to an elliptically polarized light field with an amplitude ratio of the x-polarization component to the y- component being $1:\sqrt{3}$ by using a quarter-wave plate (10RP44-3, Newport) and a half-wave plate (10RP42-3, Newport Inc). This elliptically polarized pump beam was collinearly combined with the linearly polarized Stokes beam through a dichroic mirror (LW-45-RU780-TU946, CVI Inc), and delivered into a customized confocal laser scanning system (FV300, Olympus Inc) and then focused onto the sample by a microscope objective (UPlanSApo 40×, N.A. 0.9, Olympus Inc) for CARS generations. The CARS signals were collected by a condenser (IX2-LWUCD, N.A. 0.55, Olympus Inc) and detected by a photomultiplier tube (PMT) (R3896, Hamamatsu Inc) through a filter set (equivalent to a bandpass filter centered at 660 nm with FWHM of 40 nm) and a polarization analyzer. In this

work, the medium N.A.(≤0.9) objectives were used to reduce the polarization scrambling effect of the samples caused by tightly focusing. The polarization extinction ratio of the linearly polarized Stokes beam after passing through the microscope objectives and the sample was around 150:1, which was proved to be sufficient for polarization-sensitive CARS detection. The intensity ratio of the x-polarization component to the y-component for the elliptically polarized pump field was maintained at 1.0:3.0.

3.2.3 Results and Discussions

Fig. 3.16 shows the CARS images of 1.5 μm polystyrene beads immersed in water for: (a) normal CARS, (b) elliptically polarized CARS, and (c) normal P-CARS, respectively. The corresponding intensity profiles across the lines indicated in the CARS images (Figs. 3.16(a-c)) were shown in Figs. 3(d-f), respectively. The normal CARS imaging (Fig. 3.16(a)) provided a relatively intense signal, but a large nonresonant background from the beads and the surrounding water was also present, resulting in a poor contrast of image (signal-to-background ratio of ~2:1, Fig. 3.16(d)). In contrast, the EP-CARS imaging (Fig. 3.16(b)) significantly suppressed the nonresonant background yielding a 6-7-fold improvement in image contrast (signal-to-background ratio of 12~14:1, Fig. 3.16(e)), which was similar to the normal P-CARS technique with efficient background rejection capability (ratio of 10~12:1, Figs. 3.16(c, f)). Moreover, the EP-CARS technique also offered an approximately 1.25-fold improvement in resonant CARS signal detection (~120 counts, Fig. 3.16(e)) than that of normal P-CARS (~95 counts, Fig. 3.16(f)), which was consistent with

theoretical calculations (Eq. (3.20)). The normal CARS and the EP-CARS spectra as well as the Raman spectrum of 1.5 μm polystyrene beads immersed in water were also measured. Different from the normal CARS spectrum which displayed a dispersive lineshape with a large nonresonant background, the EP-CARS spectrum had a spectral lineshape similar to the Raman spectrum without nonresonant interference from water and the beads. The above results confirmed the ability of the elliptically polarized CARS technique for effective suppression of the nonresonant background while also improving the detected signal levels compared with normal P-CARS microscopy, thereby enabling high sensitive and high contrast vibrational imaging.

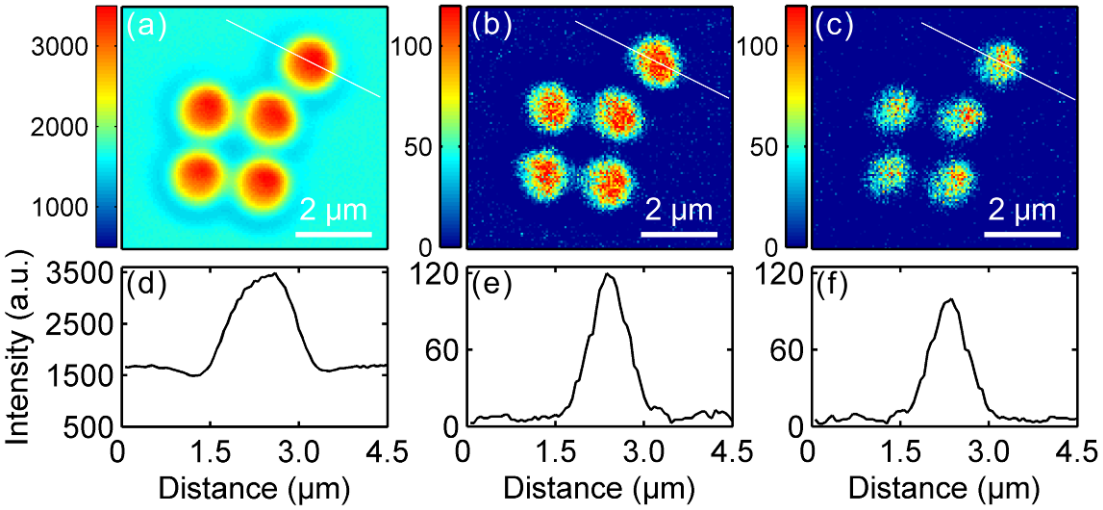

Fig. 3.16 Comparison of CARS images (aromatic C-H stretching vibration centered at 3054 cm^{-1}, FWHM: ~150cm^{-1}) of 1.5 μm polystyrene beads immersed in water: (a) normal CARS; (b) EP-CARS, and (c) normal P-CARS. Figs. (d-f) are the corresponding intensity profiles across the lines indicated in the images (a)-(c). The average powers of the pump beam (835 nm) and Stokes beam (1121 nm) on the sample are 2 mW and 0.5 mW, respectively.

The applicability of the EP-CARS technique for high contrast cell imaging was illustrated. Fig. 3.17 shows an example of CARS images of lipid droplets in an unstained fibroblast cell from (a) normal CARS, and (b) EP-CARS, respectively. The

corresponding intensity profiles were displayed in Figs. 3.17(c-d). Clearly, the EP-CARS imaging on the fibroblast cell (Fig. 3.17(b)) gave a higher signal-to-background ratio (of ~13-15:1, Fig. 3.17(d)) than the normal CARS (vibrational contrast of ~2:1, Fig. 3.17(c)). This reconfirmed the superior capability of the EP-CARS technique for effective removal of nonresonant background, which was particularly useful for probing biomolecules in biological systems with high contrast.

One notes that the EP-CARS detection is relatively less sensitive to the interference of frequency-independent large nonresonant backgrounds created by using the femtosecond excitation laser pulses (broadband: ~100-150 cm^{-1}) for high contrast, directly quantitative imaging of biological samples (Fig. 3.17). This is because in EP-CARS microscopy, the two nonresonant background signals generated by $P_{1111}^{(3)nr}$ and $P_{1221}^{(3)nr}$ can be maintained at the same amplitude while in opposite phase, and thus no matter using femtosecond or picosecond laser pulses as excitation sources, the complete destructive interference of the two nonresonant CARS fields can always hold, thereby enabling an effective cancellation of nonresonant backgrounds for background-free CARS imaging. It should be pointed out that similar to the P-CARS microscopy, the performance of nonresonant background suppression using EP-CARS microscopy could be limited by some factors, such as wavelength-dependent depolarization effect and the birefringence of the optics, as well as polarization scrambling caused by highly scattering samples (e.g., thick tissue) [29].

3.2.4 Summary

A novel EP-CARS microscopy was developed employing the excitation of an elliptically polarized pump field and a linearly polarized Stoke field to permit effective removal of nonresonant backgrounds for high contrast vibrational imaging. It is expected that the EP-CARS technique would be robust working with broadband laser sources (e.g., femtosecond pulses excitation) for high contrast biomolecular imaging in biological systems.

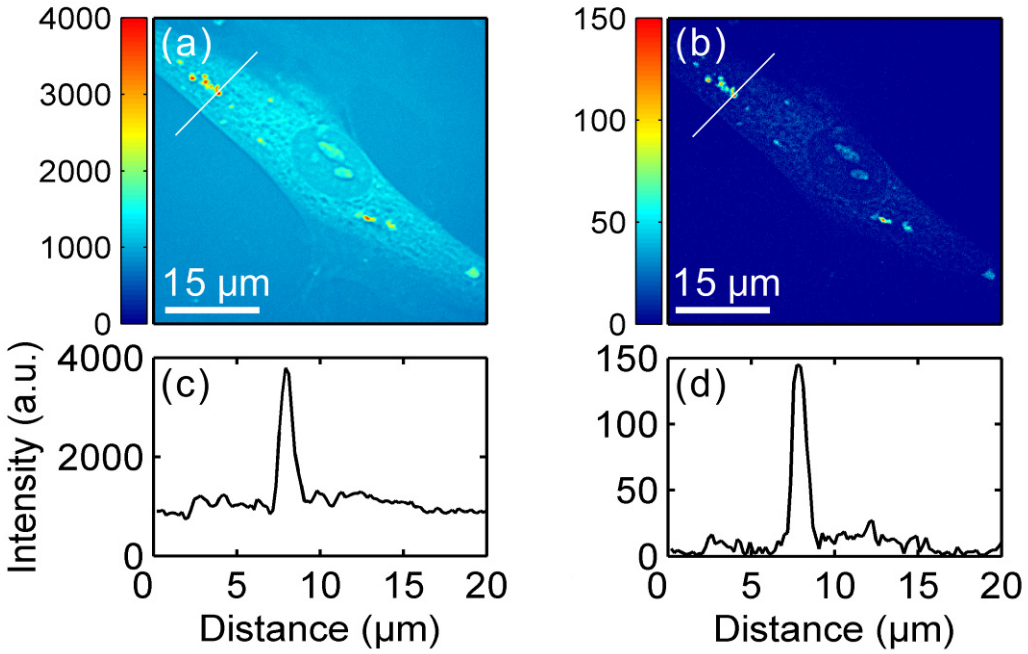

Fig. 3.17 CARS images (symmetric CH_2 stretching vibration centered at 2845 cm^{-1}, FWHM: ~150cm^{-1}) of lipid droplets in an unstained fibroblast cell: (a) normal CARS, and (b) EP-CARS. (c) and (d) are the corresponding intensity profiles across the lines indicated in the images (a) and (b), respectively. The average powers of the pump beam (835 nm) and Stokes beam (1095 nm) on the cell are 1.6 mW and 0.4 mW, respectively.

In this chapter, four kinds of modalities based on interference and polarization, that is, IP-CARS, phase-controlled P-CARS, HP-CARS and EP-CARS techniques, were demonstrated to realize high contrast CARS imaging with sensitivity ((e.g., for IP-CARS, ~2-fold improved SNR compared with conventional P-CARS was

achieved). Compared with time-resolved CARS, Heterodyne-CARS and FM-CARS previously reported, only one pump and one Stokes pulsed laser source are needed in IP-CARS, HP-CARS and EP-CARS we developed. Therefore, our methods are cost-effective. Compared with the weak resonant signals in conventional P-CARS, time-resolved CARS, and FM-CARS, IP-CARS and HP-CARS yield 10-20-fold resonant signal amplification, which greatly improves the detection sensitivity. Compared with conventional interferometric CARS techniques (such as Heterodyne-CARS), higher interference efficiency between generated CARS signal and the local oscillator can be achieved in our IP-CARS and HP-CARS, which results in a better tolerance in our methods for highly scattering samples, such as tissues . The reason is that since both the CARS signal and the local oscillator arise from exactly the same focal excitation volume, the complete constructive and destructive interference of the two CARS signals may still be achievable even for highly scattering samples. HP-CARS requires very low excitation power, because the local oscillator in this method is gained from the idle CARS signal generated in the conventional P-CARS process. EP-CARS microscopy has a 1.25-fold improvement in sensitivity over normal P-CARS. Note that the 1.25-fold increase of resonant signal achieved with EP-CARS can also be realized by common P-CARS technique with 3 color excitation [41]. However, involving of 3-color laser beams makes the system too complex and highly cost.

Chapter 4 CARS Imaging using Tightly Focused Radially Polarized Light

Very recently, radial polarization beam has attracted increasing attention due to their unique focusing properties as well as a very strong longitudinal field component generated at the focal point. In this chapter, radial polarization (RP-) CARS microcopy using annular detection was proposed and numerically investigated through FDTD simulation method. In addition, RP-CARS microscopy for facilitating longitudinally oriented molecules detection has also been experimentally demonstrated for the first time.

4.1 Radial Polarization (RP-) CARS with Annular Detection for High Contrast Imaging

4.1.1 Introduction

Recently, radially polarized laser beams have attracted increasing attention because of their unique light distribution properties (e.g., a very strong longitudinal field component and a tighter focal spot size) at the focal point by using a high numerical aperture (NA) objective [185]. The unique radial focal field distribution thus has potential applications in high-resolution 3-D microscopy imaging, such as confocal microscopy [186], second harmonic generation (SHG) [187], third harmonic generation (THG) [188]. In this study, a unique annular aperture detection scheme was proposed in radially polarized CARS (RP-CARS) microscopy under tightly focused radially polarized pump and Stokes light excitation to effectively remove the nonresonant background for high contrast vibrational imaging. The finite-difference

time-domain (FDTD) method [189, 190] was employed to investigate the effects of the scatterers' sizes and annular aperture diameters on the signal-to-background ratio (SBR) of the forward- and backward- detected RP-CARS microscopy.

4.1.2 Theory

Fig. 4.1 illustrates the schematic of an annular aperture detected RP-CARS microscopy for both the forward- and backward- CARS detection. The radially polarized pump ($\boldsymbol{E}(\boldsymbol{r}, \omega_p)$) and Stokes ($\boldsymbol{E}(\boldsymbol{r}, \omega_s)$) light fields are tightly focused onto a spherical scatterer through a high NA objective for CARS generation. Under tight focusing of the radially polarized light field, the longitudinal electric field component (E_z) and the radial component (E_ρ) at the focal point can be expressed as [191]

$$E_z(\rho, z) = 2iA\int_0^\alpha \cos^{1/2}(\theta)\sin^2(\theta)l(\theta)J_0(k\rho\sin\theta)e^{ikz\cos\theta}\mathrm{d}\theta, \tag{4.1.1}$$

$$E_\rho(\rho, z) = 2A\int_0^\alpha \cos^{1/2}(\theta)\sin(2\theta)l(\theta)J_1(k\rho\sin\theta)e^{ikz\cos\theta}\mathrm{d}\theta, \tag{4.1.2}$$

where A is a constant; $\alpha = \arcsin(\mathrm{NA}/n)$; $k = 2\pi/\lambda$ is the wave vector; J_0 and J_1 denote Bessel functions of the first kind with orders 0 and 1; $l(\theta)$ is the pupil function of a Bessel-Gaussian beam:

$$l(\theta) = \exp\left[-\beta_0^2\left(\frac{\sin\theta}{\cos\alpha}\right)^2\right]J_1\left(2\beta_0\frac{\sin\theta}{\sin\alpha}\right), \tag{4.2}$$

where β_0=3/2 is the ratio of the pupil radius to the beam waist.

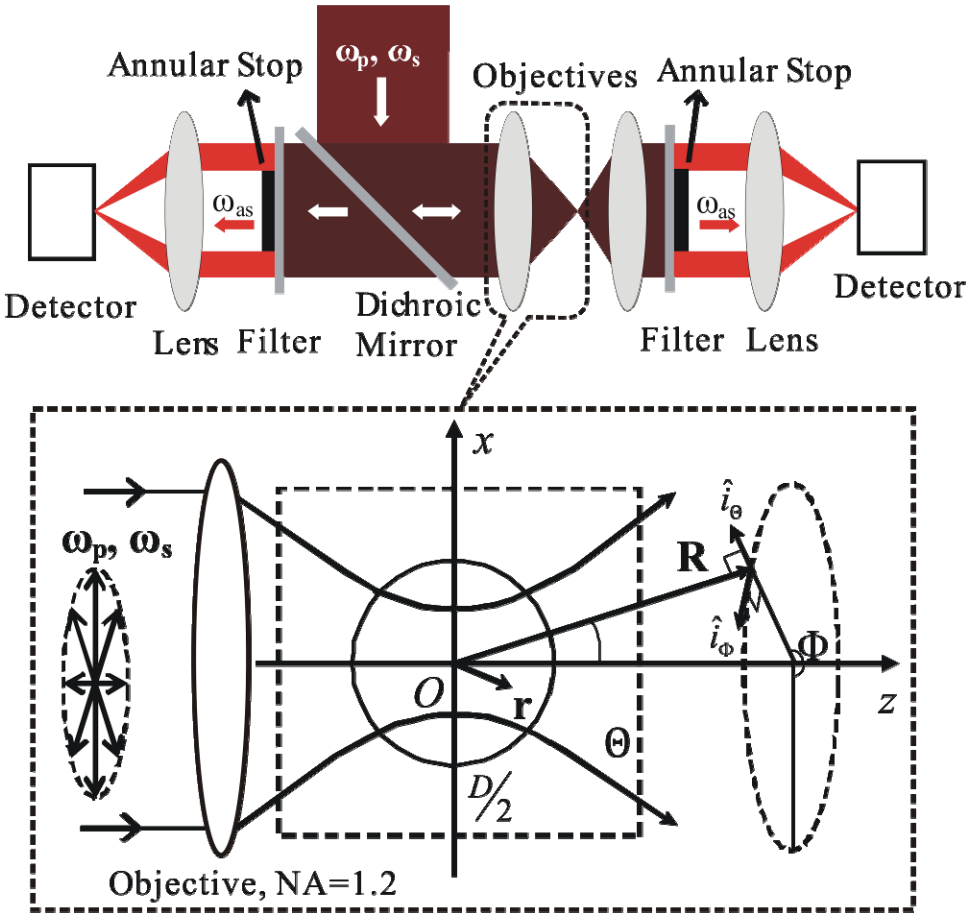

Fig. 4.1 Illustration of the annular-aperture detected radially polarized CARS (RP-CARS) microscopy. The radially polarized pump and Stokes light fields are tightly focused into a scatterer (i.e., polystyrene bead) by a high NA objective for CARS generation. The annular aperture detection in the forward and backward directions uses aperture stops to block the central part of the objective's aperture. The pump beam wavelength λ_p is selected at 750 nm; whereas the Stokes beam λ_s is 852 nm. The CARS radiation wavelength λ_{CARS} is at 670 nm, representing the mono-substituted benzene rings stretch vibration at 1600 cm^{-1} of polystyrene beads. Note that the dashed box represents the finite-difference time-domain (FDTD) computation space that is divided into cubic cells of $\lambda_p/40$ at each step for simulations. The NAs of the focusing and collecting objectives are assumed to be 1.2 (water immersion) and 1.42 (oil immersion), respectively. The refractive indices of water and polystyrene beads are 1.33 and 1.59, respectively.

The induced third-order nonlinear polarization at the anti-Stokes frequency, $\omega_{as} = 2\omega_p - \omega_s$ with the phase matching condition $|\Delta\mathbf{k}|\ D << \pi$ (D is the size of the scatterer; $\Delta\mathbf{k} = \mathbf{k}_{as}-(2\mathbf{k}_p-\mathbf{k}_s)$), can be written as [52]

$$P_i^{(3)}(\mathbf{r},\omega_{as}) = 3\sum_{jkl}\chi_{ijkl}^{(3)}E_j(\mathbf{r},\omega_p)E_k(\mathbf{r},\omega_p)E_l^*(\mathbf{r},\omega_s)\,, \tag{4.3}$$

where $\chi_{ijkl}^{(3)}$ is the third-order nonlinear susceptibility; *i*, *j*, *k*, and *l* run over *x*, *y*, *z*, respectively, of the three components in a Cartesian coordinate system. According to Green's function, the CARS radiation in the far-field can be expressed as [28]

$$\begin{aligned}\mathbf{E}_{as}(\mathbf{R},\Theta,\Phi) = -\frac{\omega_{as}^2}{c^2}\frac{\exp(ik_{as}|\mathbf{R}|)}{|\mathbf{R}|}\int \mathrm{d}V \exp\left(\frac{-ik_{as}\mathbf{R}\cdot\mathbf{r}}{|\mathbf{R}|}\right)\\ \times\begin{bmatrix}0 & 0 & 0\\ \cos\Theta\cos\Phi & \cos\Theta\sin\Phi & -\sin\Theta\\ -\sin\Phi & \cos\Phi & 0\end{bmatrix},\\ \times\begin{bmatrix}P_x^{(3)}(\mathbf{r})\\ P_y^{(3)}(\mathbf{r})\\ P_z^{(3)}(\mathbf{r})\end{bmatrix}\begin{matrix}\hat{i}_R\\ \hat{i}_\Theta\\ \hat{i}_\Phi\end{matrix}\end{aligned} \tag{4.4}$$

where $\hat{i}_R$, $\hat{i}_\Theta$, and $\hat{i}_\Phi$ denote the spherical components of the CARS field (inset of Fig. 4.1). The collected CARS radiation power (I_{CARS}) can be calculated by integrating the Poynting vector over the spherical surface of radius R within the cone angle of the collection objective as follows:

$$I_{CARS} = \frac{n_{as}c}{8\pi}\int_{\Theta_1}^{\Theta_2}\mathrm{d}\Theta\int_{\Phi_1}^{\Phi_2}\mathrm{d}\Phi\left|\mathbf{E}_{as}(\mathbf{R})\right|^2 R^2\sin\Theta\,, \tag{4.5}$$

where the acceptance cone angles Θ1 and Θ2 are determined by the diameter of the annular aperture and the NA of the objective used.

4.1.3 Results and discussions

Applying the FDTD calculation, Maxwell's equations directly in time domain through the leap-frogging scheme can be solved for computing the field distributions (e.g., pump field ($\boldsymbol{E}(\boldsymbol{r}, \omega_p)$), Stokes field ($\boldsymbol{E}(\boldsymbol{r}, \omega_s)$, and CARS field ($\boldsymbol{E}(\boldsymbol{r}, \omega_{as})$) of the tightly focused radially polarized pump and Stokes fields in the focal region of the high NA microscope objective, as well as the far-field CARS radiations collected by

incorporating Eqs. (4.1-5) into the FDTD program developed. Fig. 4.2(a) shows an example of the far-field radially polarized CARS (RP-CARS) radiation pattern from a scatterer (D= $0.5\lambda_p$) centered at the focus under tightly focused radially polarized pump and Stoke fields excitation with a water immersion objective (NA of 1.2). It is observed that the RP-CARS radiation pattern is doughnut-shaped, with the radiation confined within the cone angles depending on the scatterers' sizes and the objective NA used [122]. Fig. 4.2(b) shows the comparison of RP-CARS radiation patterns generated from the scatterers at different diameters (D= $0.1\lambda_p$, $0.5\lambda_p$, $1.0\lambda_p$, and $2.0\lambda_p$) and the nonresonant background from water. For the forward RP-CARS detection using the oil immersion objective (NA=1.42), the nonresonant background from water increases with the acceptance cone angles ranging from 0 to 20° (maximum), and then rapidly falls when further increasing the acceptance cone angles (20° to 70°). The RP-CARS radiation patterns from the scatterers with a small diameter ($\leq 0.1\lambda_p$) or a large diameter ($\geq 2.0\lambda_p$, exceeding the focal volume of light beam) are similar to that of the nonresonant background radiation from water. However, the RP-CARS radiation from those scatterers with sizes of between $0.1\lambda_p$ and $2.0\lambda_p$ are much stronger than the nonresonant background within the acceptance cone angles ranging from 50° to 70° for the forward-detected direction, whereas the acceptance cone angles ranging from 115° to 150° for the backward-detected direction (Fig. 4.2(b)). Therefore, by incorporating the suitable sizes of annular stop apertures into CARS detection paths, the nonresonant background from water can be significantly removed for high contrast RP-CARS imaging.

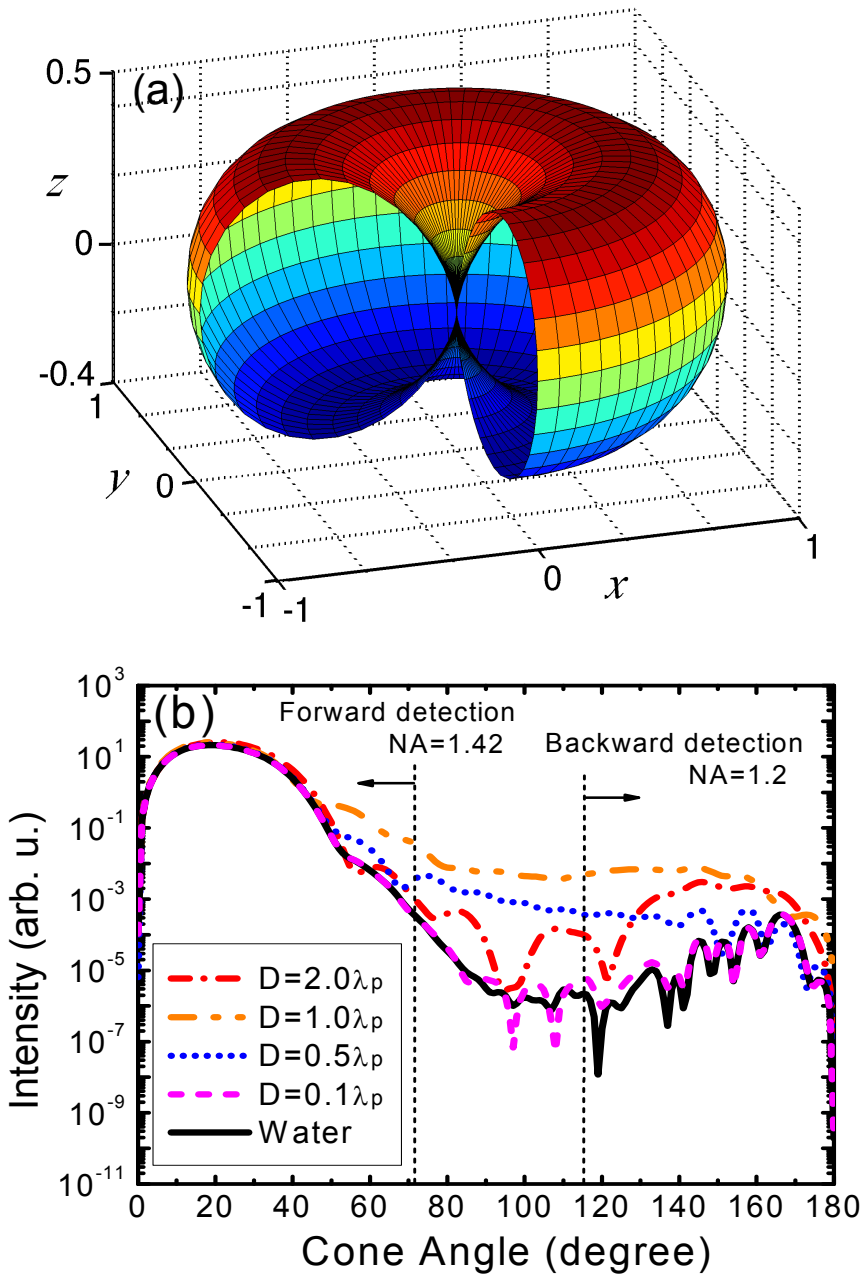

Fig. 4.2 (a) Far-field RP-CARS radiation pattern from a scatterer (D= $0.5\lambda_p$) centered at the focus under the tightly focused radially polarized pump and Stoke fields excitation with a water immersion objective of NA 1.2. The x, y and z axes are in arbitrary units. Only the radiation in the range $-\pi/2 \leq \Phi \leq \pi$ is displayed for clarity. **(b)** Far-field RP-CARS radiation patterns generated from the scatterers at different diameters (D= $0.1\lambda_p$, $0.5\lambda_p$, $1.0\lambda_p$, and $2.0\lambda_p$) as well the nonresonant background from water. The vertically dashed lines in the figure indicate the maximum acceptance cone angles of the microscope objectives for both the forward (NA=1.2) and backward (NA=1.42) CARS detection, respectively.

To evaluate the efficacy of applying the annular aperture detection scheme in RP-CARS microscopy for improving image contrast, FDTD method is applied to study the changes of forward-detected RP-CARS (F-CARS) intensities and the corresponding signal-to-background ratios (SBR) with different diameters of annular stop apertures (Fig. 4.3). Although the F-CARS radiation from the scatterers with different diameters (i.e., $0.1\lambda_p$ to $2.0\lambda_p$) decreases by 4 to 5 orders in intensity with the increased diameters (i.e., 0 to 0.9) of annular stop apertures used, the lowest F-CARS intensity level is still comparable to that in backward-detected RP-CARS (E-CARS) without using any annular aperture (Fig. 4.4(a) at $D_S/D_A=0$); and the corresponding SBR of F-CARS radiation from the scatterers with diameters of $0.1\lambda_p$ to $2.0\lambda_p$ increases remarkably, particularly when the annular stop aperture is larger than 0.4 (Fig. 4.3(b)). For instance, an SBR of 90 can be achieved for F-CARS radiation from the scatterer with a diameter of $1.0\lambda_p$ when applying an annular stop aperture of 0.9 in diameter (acceptance cone angles range from 55° to 70°). The backward-detected RP-CARS (E-CARS) intensities and the corresponding SBR with different diameters of annular stop apertures in the detection path (Fig. 4.4) were also calculated. The E-CARS radiation from the scatterers with different diameters ($0.1\lambda_p$ to $2.0\lambda_p$) decreases by 1 to 2 orders in intensity with the increased diameters (0 to 0.9) of annular stop apertures used (Fig. 4.4(a)). The corresponding SBR of E-CARS radiation from the scatterers with diameters of $0.1\lambda_p$ to $2.0\lambda_p$ increases gradually with the increased diameters of annular stop apertures up to 0.8 (corresponding to acceptance cone angles ranging from 115° to 120°), at which the maximum SBR of $\sim 1.2 \times 10^4$

can be achieved for E-CARS radiation from the scatterer with a diameter of $1.5\lambda_p$ (Fig. 4.4(b)).

4.1.4 Summary

Compared with RP-CARS radiation without applying annular apertures (Figs. 4.3(b) and 4.4(b) at $D_S/D_A=0$), the annular aperture detection can improve the SBR of up to 115 times for forward-detected RP-CARS imaging, and of ~ 55 times for backward-detected RP-CARS microscopy. This work demonstrated that the annular aperture detection scheme can effectively remove nonresonant background for high contrast vibrational imaging in RP-CARS microscopy. As a future direction, experiments could be performed to validate the effectiveness of this annular detection scheme.

4.2 RP-CARS for Sensing Molecular Orientation

In this section, the realization of a radially polarized CARS (RP-CARS) microscopy technique was demonstrated by utilizing the tightly focused radial polarization pump and Stokes light fields to facilitate longitudinally oriented molecules detection in vibrational imaging with high spatial resolution.

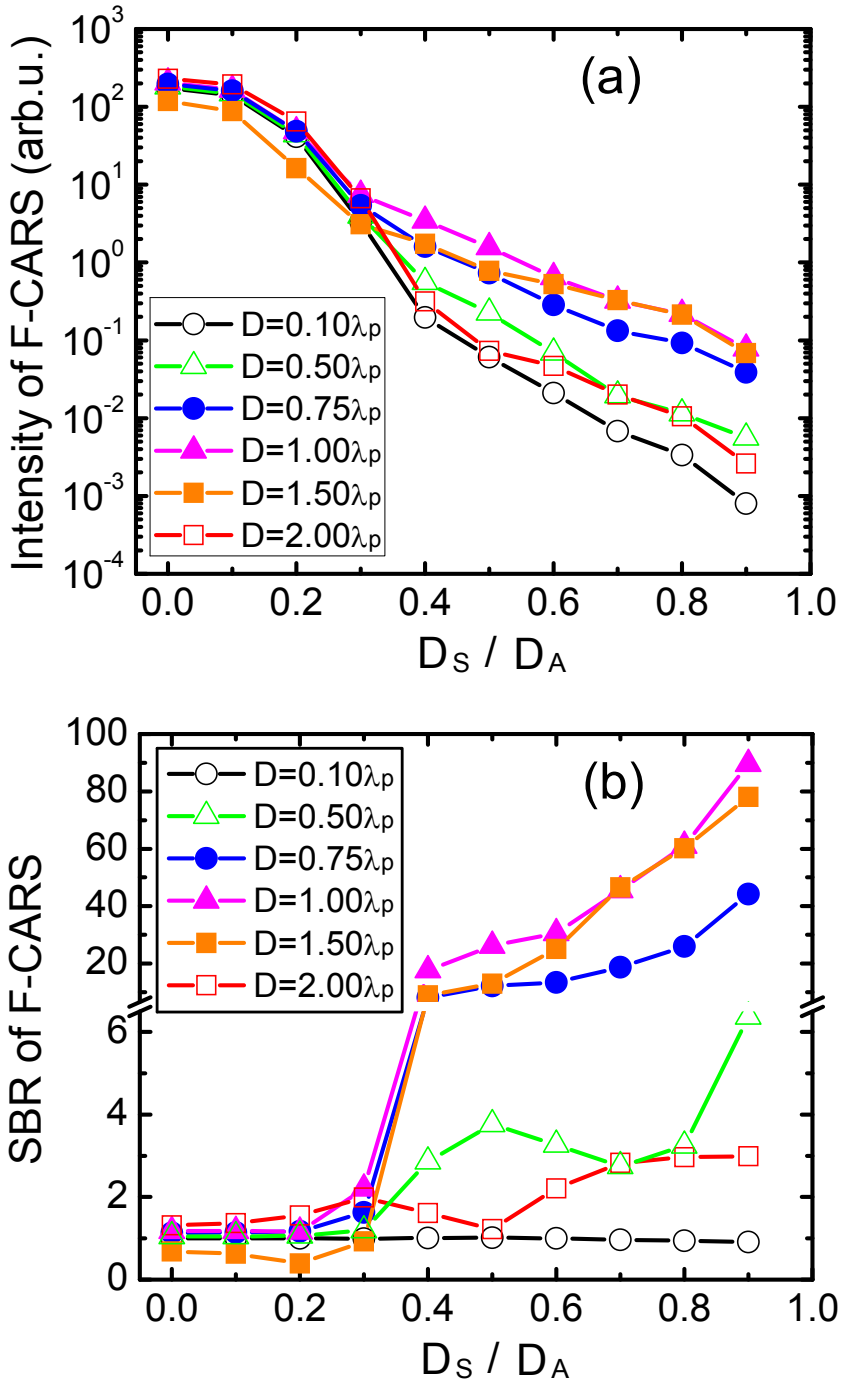

Fig. 4.3 (a) Calculated forward-detected RP-CARS (F-CARS) intensities of different scatterers (D= $0.1\lambda_p$, $0.5\lambda_p$, $1.0\lambda_p$, and $2.0\lambda_p$ using annular stop apertures with different diameters. **(b)** Relationship of the signal-to-background ratio (SBR) of F-CARS with different diameters of annular stop apertures. Note that the diameter of the annular stop aperture placed along the detection path is defined as the ratio of the diameter of the annular stop aperture (D_S) to the diameter of the objective's aperture (D_A).

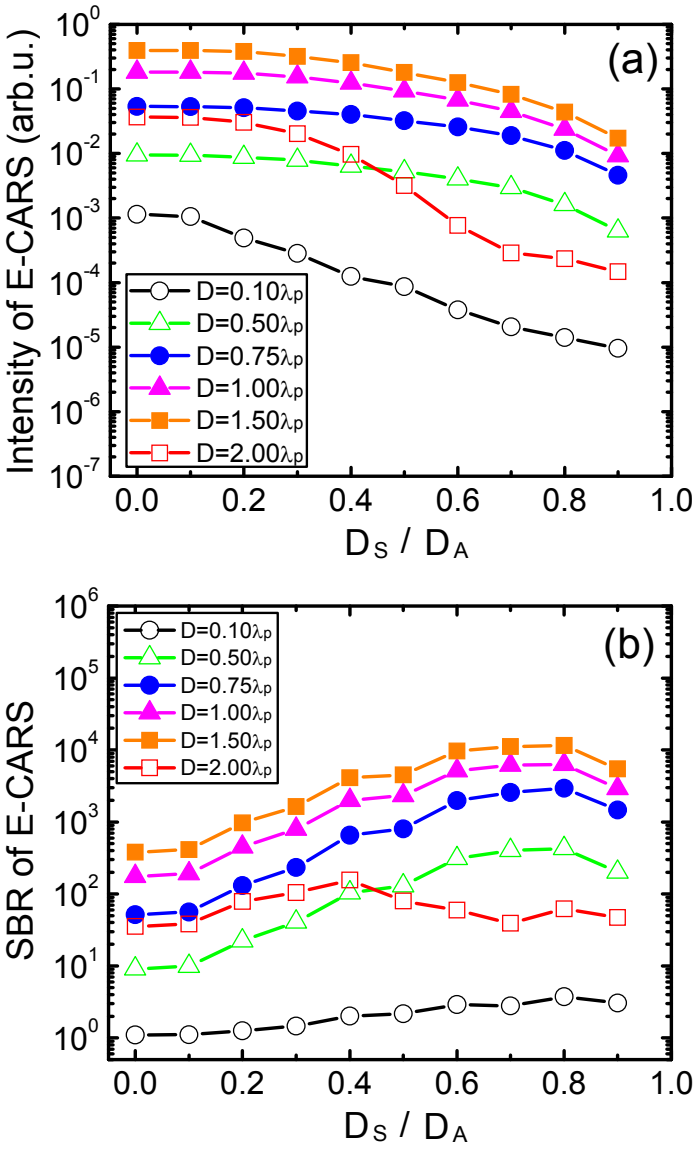

Fig. 4.4 (a) Calculated backward-detected RP-CARS (E-CARS) intensities of different scatterers (D= $0.1\lambda_p$, $0.5\lambda_p$, $1.0\lambda_p$, and $2.0\lambda_p$) using annular stop apertures with different diameters. **(b)** Relationship of the signal-to-background ratio (SBR) of E-CARS with different diameters of annular stop apertures.

4.2.1 Principle

The amplitude of the CARS field ($\vec{E}_{as}^{(j)}$) is determined by the relative orientation of the transition dipole moments (i.e., molecule orientations) with respect to the polarization direction of the excitation light fields [77, 78]:

$$\vec{E}_{as}^{(j)} \propto \sum_{i}^{N} (\vec{\varepsilon}_{p}^{(j)} \cdot \vec{\mu}_{ge}^{(i)})(\vec{\varepsilon}_{s}^{(j)} \cdot \vec{\mu}_{ev}^{(i)})(\vec{\varepsilon}_{p}^{(j)} \cdot \vec{\mu}_{ve}^{(i)})(\vec{\varepsilon}_{as}^{(j)} \cdot \vec{\mu}_{eg}^{(i)}) \chi_{1111}^{(3)} \vec{E}_{p}^{(j)} \vec{E}_{p}^{(j)} \vec{E}_{s}^{*(j)}, \qquad (4.6)$$

where *i* runs over all of the vibrational modes (*N*) involved, and *j* (= z, or tr) represents either the longitudinal or transverse component of the electric field. $\chi^{(3)}_{1111}$ is the third-order nonlinear susceptibility, and *E* and *ε* are the amplitude and polarization direction of the pump (*p*), Stokes (*s*), and CARS (*as*) fields, respectively. μ_{ge} and μ_{ev} denote the transition dipole moments among the ground state (*g*), the virtual state (*e*), and the vibrational state (*v*) of the molecular vibrations. The orientation of the transition dipole moments can be deduced from Raman scattering and the symmetry properties of the vibrational modes of interest. Using the radial polarization pump and Stokes light fields for CARS imaging, the condition $\vec{\varepsilon}_p = \vec{\varepsilon}_s$ always holds. To simplify the CARS calculation, a symmetric stretch vibration is assumed (i.e., μ_{ge}=μ_{eg}=μ_{ve}=μ_{ev}), and thus the CARS field amplitude is reduced to:

$$\vec{E}_{as}^{(j)} \propto \sum_{i}^{N} \cos^4(\varphi) \chi^{(3)}_{1111} \vec{E}_p^{(j)} \vec{E}_p^{(j)} \vec{E}_s^{*(j)}, \tag{4.7}$$

where the angle, φ, is the relative orientation of the excitation light field polarization with regard to the transition dipole moment. Hence, the CARS intensity (I_{as}) can be expressed as

$$I_{as} \propto \left|\vec{E}_{as}^{(j)}\right|^2 \propto \cos^8 \varphi. \tag{4.8}$$

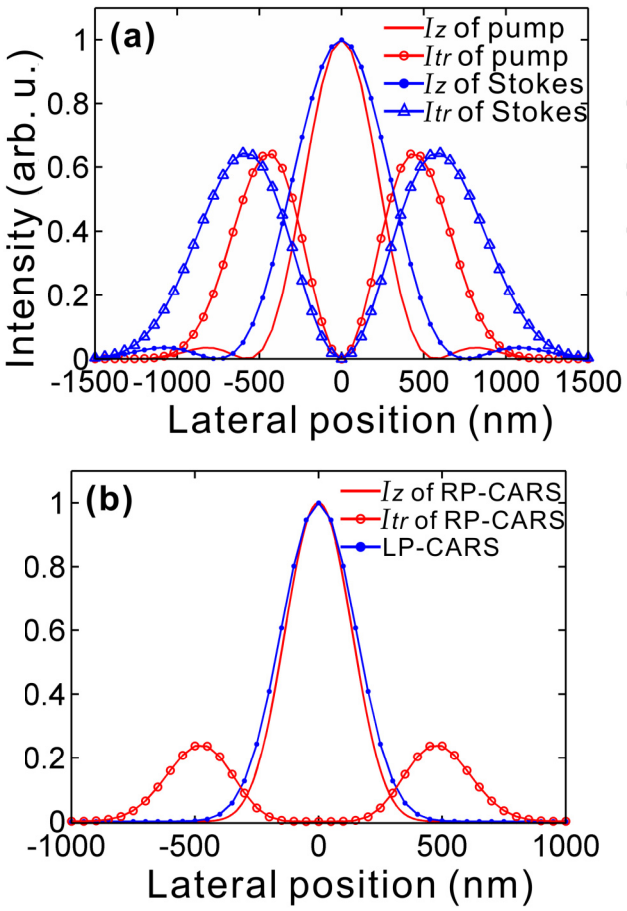

Fig. 4.5 (a) Calculated intensity distributions of the longitudinal component (I_z) and transverse component (I_{tr}) on the focal plane of the objective for the radially polarized pump and Stokes light fields. **(b)** Comparison of the calculated intensity distributions of radially polarized CARS and linearly polarized CARS on the focal plane of the objective. Note that in intensity distribution computations, NA of the water immersion objective is assumed to be 1.2, and the pump, Stokes and CARS fields are centered at 832, 1096, and 670 nm, respectively. RP-CARS, radially polarized CARS; LP-CARS, linearly polarized CARS.

Obviously, when the polarization angle of the excitation light field is parallel to the transition dipole moment of molecular vibrations, a maximum CARS radiation will be generated from the longitudinally oriented molecules (i.e., $\varphi = 0$); whereas only a minimum CARS radiation can be observed from the transversely orientated molecules (i.e., $\varphi = 90^\circ$).

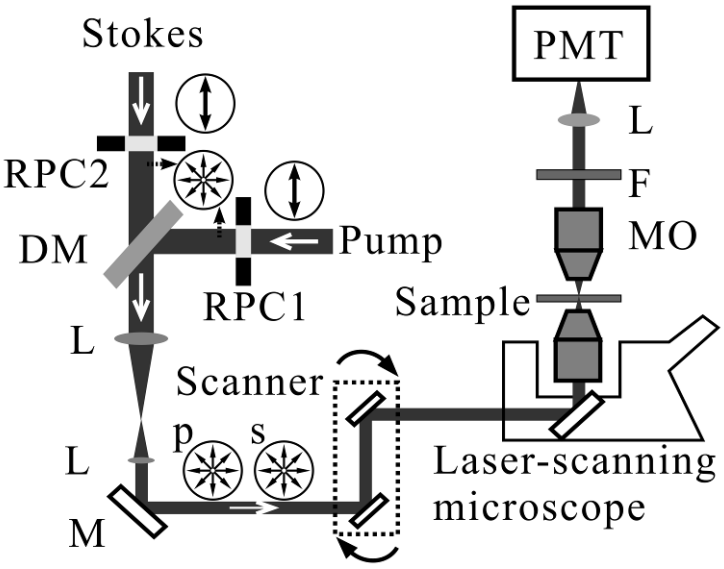

Fig. 4.6 Schematic of the radially polarized coherent anti-Stokes Raman scattering (CARS) microscope developed. Radially polarized pump and Stokes light fields are generated by passing the linearly polarized pump and Stokes beams through the liquid crystal-based radial polarization converters and then collinearly coupled into a laser scanning confocal microscope for CARS imaging. RPC, radial polarization converter; DM, dichroic mirror; L, lens; M, mirror; MO, microscope objective; F, filter set; PMT, photomultiplier tube; p, pump beam; s, Stokes beam.

To better understand the focusing properties of radially polarized beams on CARS microscopy, the focal intensity distributions of the longitudinal component (I_z) and the transverse component (I_{tr}) of the radially polarized pump and Stokes fields focused by a 1.2 NA objective (Fig. 4.5(a)) were calculated. The corresponding radially polarized CARS intensity distributions of the longitudinal and transverse components are shown in Fig. 4.5(b). The intensity ratio of the longitudinal component I_z to the transverse component I_{tr} for both the radial polarization pump and Stokes light fields is ~1.5 (Fig. 4.5(a)), while the CARS intensity ratio of the longitudinal component to the transverse component is ~4.2 (Fig. 4.5(b)). This suggests that using the radial polarization pump and Stokes light fields, CARS radiations from longitudinal oriented molecules (i.e., longitudinal component) dominate over CARS signals generated from

transversely oriented molecules (i.e., transverse component). Furthermore, to compare the lateral resolution (FWHM) between radially polarized CARS and linearly polarized CARS techniques, the lateral intensity profile of linearly polarized CARS (blue curve in Fig. 4.5(b)) was also calculated. The radially polarized CARS gives an FWHM of ~310 nm, which is ~10% narrower than the linearly polarized CARS (FWHM of 350 nm), indicating the ability of radially polarized CARS microscopy technique for providing a higher spatial resolution for molecular imaging (This was also confirmed by the RP-CARS experimental result in Fig. 4.7 below).

4.2.2 Experiment

RP-CARS microscope system for molecular vibration imaging (Fig. 4.6) has been developed [122, 192]. The radially polarized pump and Stokes light fields were effectively generated through coupling the linearly polarized pump and Stokes light beams into a pair of liquid crystal-based radial polarization converters (working range of 400-1700 nm, ARCoptix S.A, Switzerland) [193]. The radially polarized pump and Stokes light beams generated were collinearly combined through a dichroic mirror (LW-45-RU780-TU946, CVI), and delivered into a customized confocal laser scanning microscope (FV300, Olympus), and then focused onto the sample by a microscope objective (UPlanSApo, water immersion, 60×, NA 1.2, Olympus) for CARS imaging. The radially polarized CARS radiations were collected by a condenser (U-TLO, oil immersion, NA 1.42, Olympus) and detected by a photomultiplier tube (R3896, Hamamatsu) through a set of filters (equivalent to a bandpass filter centered at 670 nm with FWHM 10 nm).

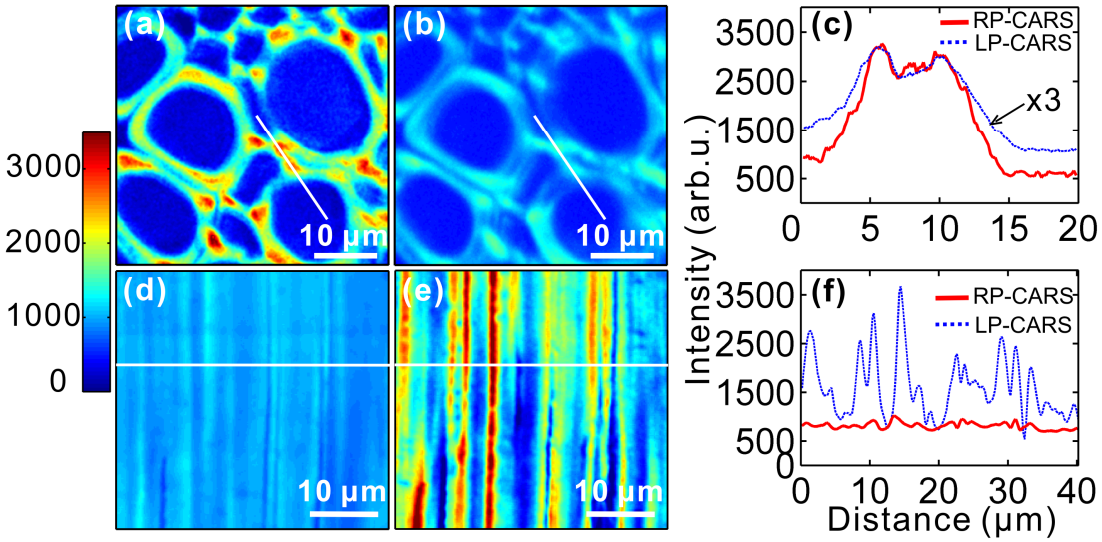

Fig. 4.7 (a) The radially polarized CARS image and (b) the linearly polarized CARS image on the 20 μm thick cottonwood leaf vascular bundles sectioned perpendicularly to the vein fibers. (c) Comparison of the corresponding intensity profiles across the lines indicated in images (a) and (b), respectively. (d) The radially polarized CARS image and (e) the linearly polarized CARS image on the 20 μm thick cottonwood leaf vascular bundles sectioned parallel to the vein fibers. (f) Comparison of the corresponding intensity profiles across the lines indicated in images (d) and (e), respectively. The C-H stretch vibration centered at 2900 cm^{-1} (FWHM~150 cm^{-1}) is used for CARS imaging. The average powers of the pump beam (832 nm) and the Stokes beam (1096 nm) on the samples are 4 and 2 mW, respectively.

4.2.3 Results and discussions

Figs. 4.7(a) and 4.7(b) show the comparison of the radially polarized CARS image and the linearly polarized CARS image (C-H stretch vibration centered at 2900 cm^{-1}, FWHM~150 cm^{-1}) on the 20 μm cottonwood leaf vascular bundles sectioned perpendicularly to the vein fibers. The corresponding intensity profiles (Fig. 4.7(c)) indicate that the CARS radiations generated from the regions with longitudinally oriented molecules were approximately 3-fold stronger in radially polarized CARS imaging compared to those in linearly polarized CARS imaging. Conversely, the linearly polarized CARS microscopy can effectively excite the regions with

transversely oriented molecules rather than longitudinally oriented molecules for vibrational imaging (Figs. 4.7(d-f)). These results confirmed that in radially polarized CARS imaging, the very strong longitudinal field components of both the tightly focused radially polarized pump and Stokes light fields are generated at the focal point, leading to an effective excitation of longitudinally oriented molecules for CARS imaging. Meanwhile, it is observed that the fine structures of molecular distributions across the fiber bundles could be identified more clearly by using the radially polarized CARS technique as compared to the linearly polarized CARS (Fig. 4.7(c)), confirming the ability of radially polarized CARS microscopy for improving the spatial resolution in vibrational imaging. One notes that although the focal spot size of the tightly focused radially polarized light beam becomes elongated along the axial direction, the focal spot size of the radially polarized CARS field generated is still much narrower than each of the pump and Stokes excitation fields according to the four-wave mixing nonlinear optical process of CARS generations. Hence, different from radially polarized SHG or THG imaging, the elongation of the focused radially polarization light has a relatively less degree of effect on the longitudinally sectioning capability in radially polarized CARS imaging.

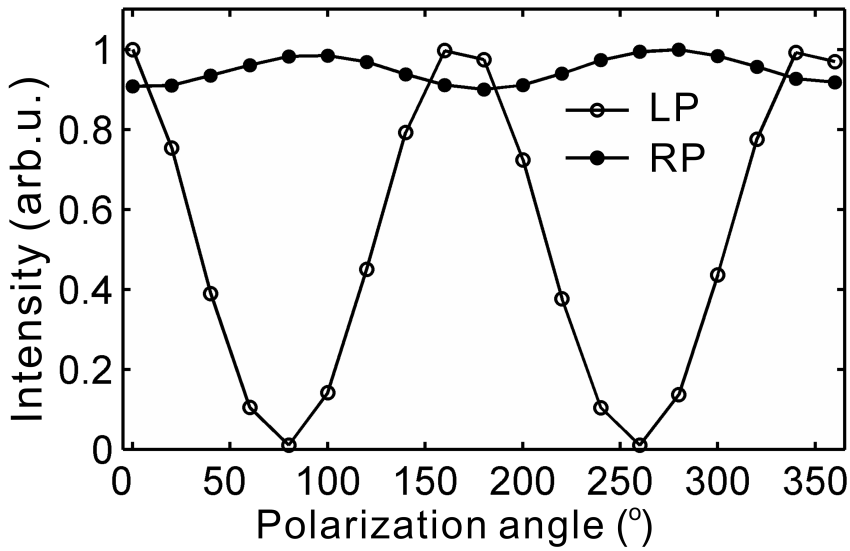

Fig. 4.8 Changes of radially polarized CARS and linearly polarized CARS intensities against the analyzer (polarizer) angle. RP, radially polarized; LP, linearly polarized.

The changes of radially polarized and linearly polarized CARS signals against the analyzer angle θ (Fig. 4.8) were compared. Different from linearly polarized CARS signals which showed a $cos^2\theta$ or $sin^2\theta$ dependency with an extinction ratio of ~100:1, the radially polarized CARS signals detected were almost independent of the analyzer angle, illustrating the unique radially polarized properties of CARS radiations after collimation. A slight fluctuation (<10%) in radially polarized CARS signals mainly arises from polarization scrambling effect of optics (e.g., birefringent effect of the dichroic mirror) in the optical path (Fig. 4.6). One notes that the radially polarized CARS signals detected in the far-field included the contributions from both the longitudinal and transverse components. With the use of near-field detection scheme, it is possible to selectively pick up the longitudinal CARS component at the focal point, thereby enabling a more effective detection of longitudinally orientated molecules [194].

4.2.4 Summary

In conclusion, a radially polarized CARS microscope was successfully developed and its ability of facilitating the longitudinally oriented molecules detection in molecular vibrational imaging with high spatial resolution was also demonstrated. It is expected that combining both the radially and linearly polarized excitation schemes, CARS microscopy could be a very powerful tool for identifying the 3-D orientations of molecules with both high sensitivity and chemical specificity.

Chapter 5 Integrated CARS and Multiphoton Microscopy for Assessment of Fibrotic Liver Tissues

In this chapter, a novel femtosecond / picosecond swappable multimodal nonlinear optical microscopy was established based on a dual 4-f paired-gratings spectral filtering of a femtosecond laser source. The application of the system was demonstrated by label-free imaging and quantitatively assessing of hepatic fats and collagens in fibrotic liver tissues. It is anticipated that the system may find wide applications of unstained biomolecular imaging in biological and biomedical systems.

5.1 Integrated CARS and Multiphoton Microscopy using Dual Paired-Gratings Spectral Filtering of a Femtosecond Laser Source

5.1.1 Instrumentation

Fig. 5.1 shows the schematic of the integrated CARS and multiphoton microscope developed for bioimaging. The pump and Stokes beams were delivered into the two separate 4-f configured paired-gratings spectral filtering systems for pulse shaping. The spectrally shaped pump and Stokes beams were collinearly combined through a dichroic mirror (SWP-45-RU1080-TU830, CVI), and delivered into a customized confocal laser scanning microscope (FV300, Olympus), and then focused onto the sample by a microscope objective (UPlanSApo 40×, N.A. 0.9, Olympus) for multimodal nonlinear optical imaging. The nonlinear optical signal radiation from the sample was collected by a condenser (U-TLD, NA 0.9, Olympus) and detected by a photomultiplier tube (R3896, Hamamatsu) through spectral filters. A flip mirror was

placed before the PMT to allow the forward CARS spectral measurements by a spectrometer (HR4000, Ocean Optics Inc., Dunedin, FL).

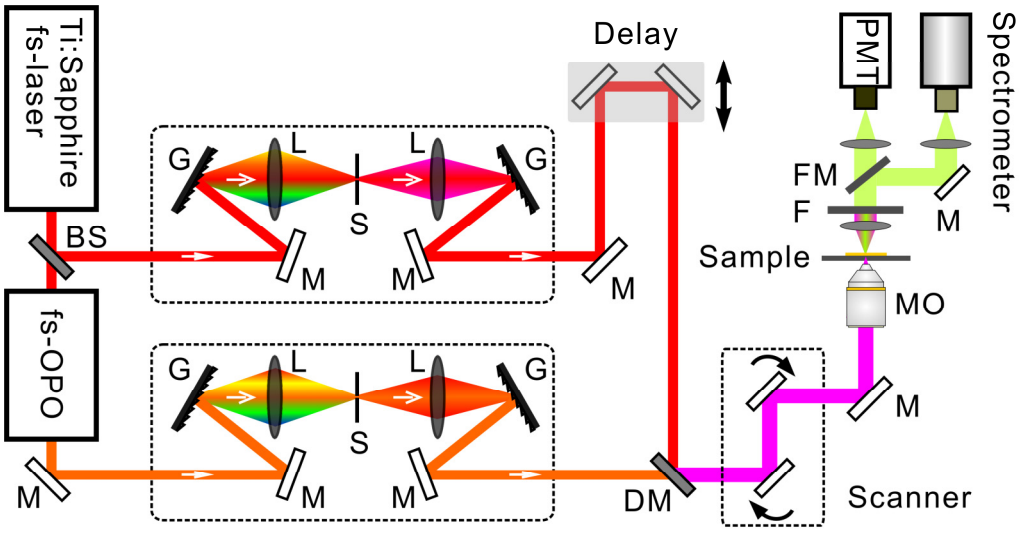

Fig. 5.1 Schematic of the integrated CARS and multiphoton microscopic platform for bioimaging. The broad bandwidth of the 100 fs pump and Stokes beams can be narrowed down to the spectral bandwidth of 11 cm^{-1} by utilizing 4-f configured paired-gratings spectral filtering. The spectrally shaped pump and Stokes beams are then collinearly coupled into a laser scanning confocal microscope (FV300) for CARS imaging. BS, beam splitter; M, mirror; G, grating; L, lens; S, slit; DM, dichroic mirror; MO, microscope objective; F, filter set; FM, flip mirror; PMT, photomultiplier tube.

When the 100 fs pump and Stokes light beams are directed into the 4-f configured paired-gratings spectral filtering systems design (Fig. 5.1), different spectral or wavelength components of the incident light are angularly dispersed into different directions by the first grating and then focused into a line on the focal plane of the first achromatic focusing lens (f = 100 mm). A motorized tunable slit is placed on the spectral plane of the first lens for spectral shaping or tailoring: i.e., the lateral position of the slit determines the central wavelength, while the slit width controls the bandwidth of the output filtered laser pulses. Since different spectral components dispersed will travel to different optical paths in this process, resulting in pulse

dispersion, and thus the second achromatic focusing lens and grating (the same as previous ones) positioned in a 4-f optics configuration are used to completely cancel out these optical path differences to minimize the overall group-velocity dispersion, which is critical to maintaining the high pulse peak power of the spectrally filtered output laser pulses for effective nonlinear optical signal generation. Note that in the 4-f configured paired-gratings filtering design, the orientations of the paired gratings are aligned in counter-directions to recombine the spectrally filtered components and compensate their angular dispersions completely. The measured the pulse spectral bandwidth (FWHM) with the spectrometer (HR4000, Ocean Optics) and the pulse duration with an interferometric autocorrelator (AA-10DM, Avesta) versus the width of the slit was shown in Fig. 5.2. It was observed that with narrowing down the slit width, the pulse FWHM becomes smaller; in contrast, the temporal duration becomes larger accordingly. The measurements confirmed that the transform-limited property of the pulses was still kept very well ($\Delta\nu \cdot \Delta t \approx 0.315$, where $\Delta\nu$ is the pulse spectral bandwidth and Δt is the temporal pulsewidth at FWHM).

The paired gratings (1200 gr/mm, blazed at 750 nm, GR50-1208, Thorlabs Inc., Newton, NJ) used for spectral filtering of the 100 fs pump beam provide an approximately 75% diffraction efficiency in the 700-1600 nm, the other paired-gratings (1200 gr/mm, blazed at 1000 nm, GR50-1210, Thorlabs Inc., Newton, NJ) for the fs Stokes beam filtering also have about 75% diffraction efficiency in the 880-1600 nm. This 4-f configured paired-gratings spectral filtering design offers a large tunability of Raman shifts covering from 100 to 8000 cm^{-1} for CARS imaging.

The overall diffraction efficiency measured from the 4-f paired-gratings system is ~6% for pump beam, and ~8% for Stokes beam. The CARS experiments proved that the power level with 6 to 8% diffraction efficiency is sufficient for high contrast ps-CARS imaging. In addition, by adjusting the slit widths down to 150 μm and 200 μm, respectively, for the input pump and Stokes light beams with pulse widths of ~100 fs (FWHM of ~ 120 cm^{-1}), ~1 ps (FWHM of ~ 11 cm^{-1}) output pump and Stokes laser pulses can be achieved from the 4-f gratings filtering system for ps-CARS imaging. As the FWHM of the spectrally filtered pump and Stokes light beams is 10-fold narrower than the fs laser beams, this indicates that the ps-CARS imaging can provide at least 10-fold improvements in spectral resolution as compared to fs-CARS [195]. Thus, simply by changing the slit widths in the 4-f paired-gratings filtering system, switching between the 1 ps and 100 fs laser pulses can be readily realized for CARS imaging (ps pulses) and multiphoton imaging (fs pulses) on the same platform for biomedical applications.

5.1.2 Results and Discussions

Figure 5.3(a) shows the comparison of fs-CARS and ps-CARS spectra as well as the corresponding Raman spectrum of 465 nm polystyrene beads immersed in water. As compared to the fs-CARS spectrum, the ps-CARS spectrum shows a much less spectral lineshape distortion and smaller frequency shift relative to the Raman spectrum. This result indicated that the nonresonant background in ps-CARS was relatively smaller than that of fs-CARS. Further, fs-CARS and ps-CARS imaging (aromatic C-H stretching vibration at 3054 cm^{-1}) of 465 nm polystyrene beads in water

(Figs. 5.3(b, c)) confirmed a 2-fold improvement in the suppression of nonresonant background using ps-CARS imaging (vibrational contrast of ~3:1, inset of Fig. 5.3(b)) compared with fs-CARS (vibrational contrast of ~1.5:1, inset of Fig. 5.3(c)). The results validated the capability of the system for realizing both high-contrast CARS imaging and high-quality multiphoton imaging on the same platform. In the next section, the system was applied for multimodal imaging of fibrotic liver tissues for both qualitative and quantitative analysis.

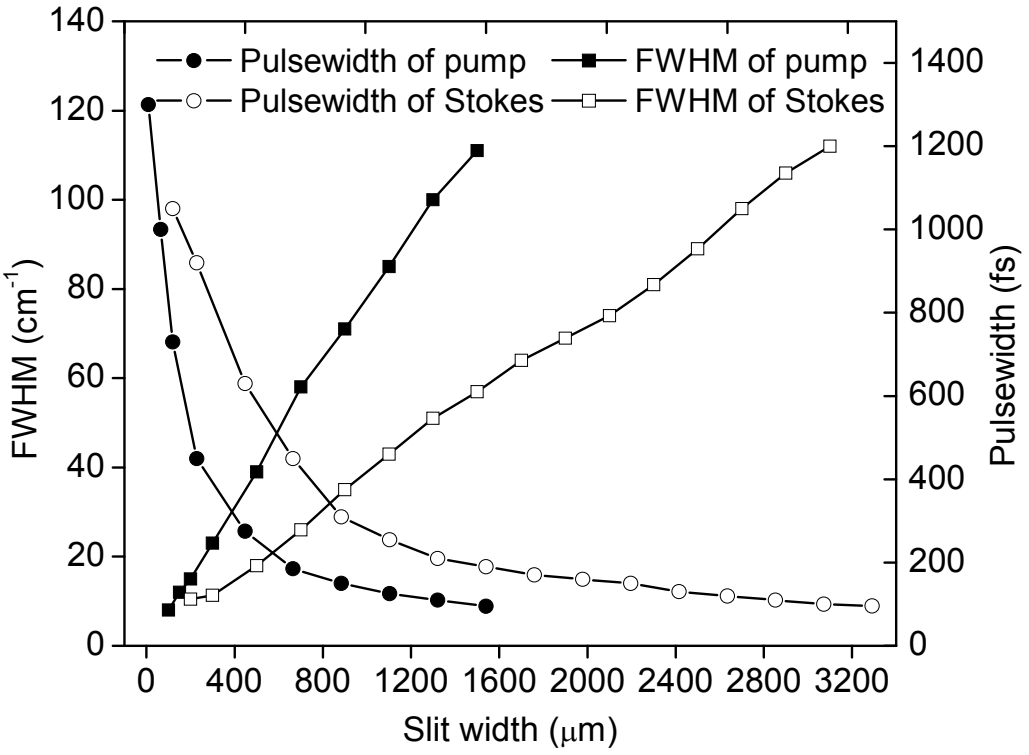

Fig. 5.2 The plotted pulse spectral FWHM and temporal duration of the pump and Stokes beams as a function of the slit width.

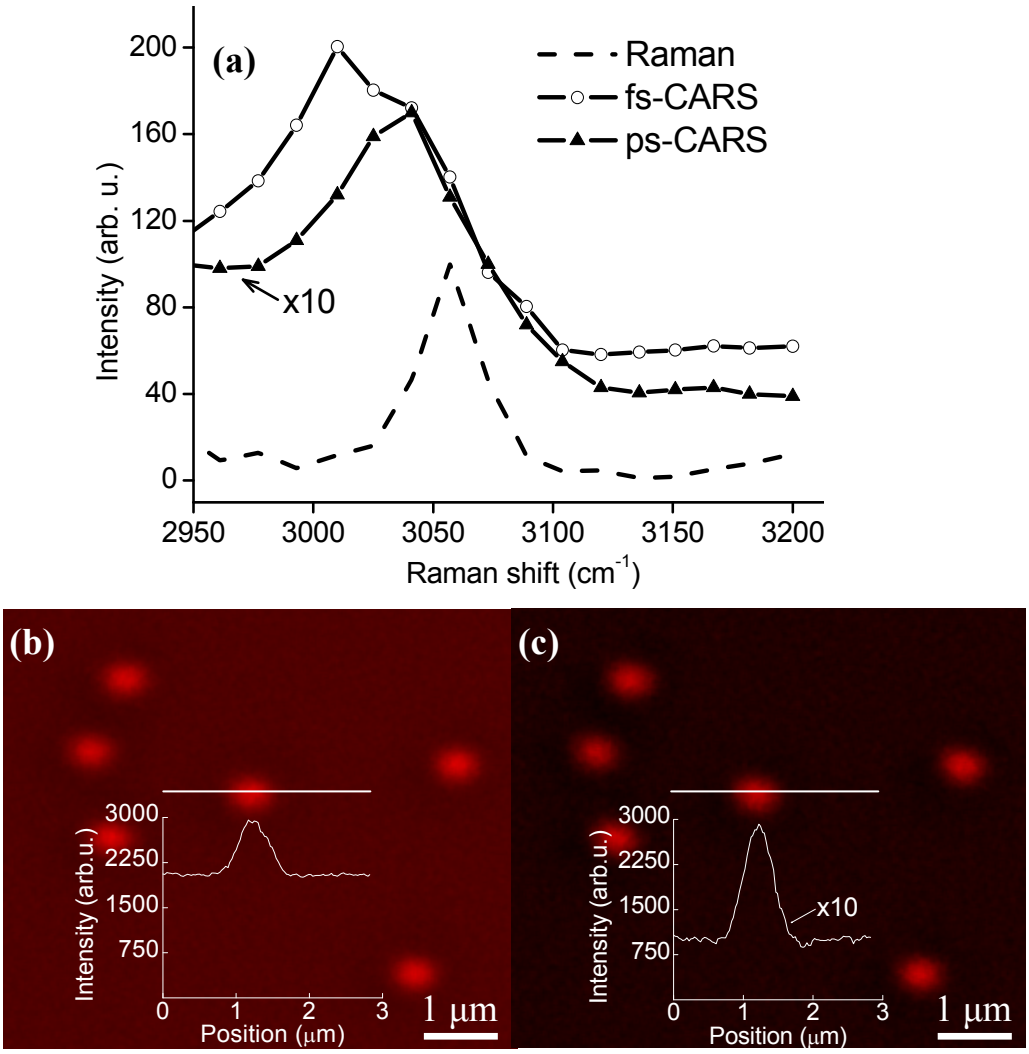

Fig. 5.3 (a) Comparison of fs-CARS and ps-CARS spectra, as well as the Raman spectrum of 465 nm polystyrene beads immersed in water. Comparison of the fs-CARS image (b) and ps-CARS image (c) of 465 nm polystyrene beads in water (aromatic C-H stretching vibration at 3054 cm^{-1} of polystyrene beads). Note that the Raman spectrum was recorded using a micro-Raman spectrometer system (inVia, Renishaw, UK), and CARS spectra were obtained by scanning the wavelengths of Stokes beam from 1099 nm to 1130 nm while fixing the wavelength of pump beam at 830 nm. The average powers of the pump and Stokes beams are 4 and 2 mW, respectively, for both fs-CARS and ps-CARS imaging.

5.2 Multimodal Nonlinear Optical (NLO) Imaging of Fibrotic Live Tissues

5.2.1 Sample preparation: the BDL rat model

As shown in Fig. 5.4, liver fibrosis disease was induced by bile duct ligation (BDL) on a rat model [196, 197]. All procedures were performed on male Wistar rats, with initial weight of 200g. Animals were housed in the Animal Holding Unit (AHU) of the National University of Singapore (NUS) with free access to standard lab chow (Laboratory Rodent Diet 5001; LabDiet, Richmond, IN) and water in a 12:12 – hour light / dark schedule. Experiments were approved by the Institutional Animal Care and Use Committee (IACUC). Bile duct ligation (BDL) of rats was performed under general anesthesia with ketamine and xylazine. A midline abdominal incision was performed, exposing the liver and intestines. The lower end of the bile duct is identified at its insertion into the small intestines and traced up towards the porta. The bile duct is then doubly ligated at two areas near the porta with silk sutures and then transacted between the two ligation points. Wound is then closed with double layered tissue closure with vicryl sutures. A total of 9 rats were ligated and sacrificed at intervals of 2, 4 and 6 weeks (n = 3 per week). 3 control rats were also sacrificed at week 0.

Cardiac perfusion with 4 % paraformaldehyde was performed to flush out blood cells. The liver tissues were fixed using formalin before harvesting. After fixation, the tissue blocks were embedded in paraffin, then cut in a microtome to 50 micron and affixed onto the slides. Leave the slides overnight to dry, then deparaffinization and

rehydration were performed as follows: Place the slides in a rack, and wash the samples in the following sequences: (1) Xylene for 6 minutes; (2) Xylene 1:1 with 100% ethanol for 3 minutes; (3) 100% ethanol for 6 minutes; (4) 95% ethanol for 3 minutes; (5) 70% ethanol for 3 minutes; (6) 50% ethanol for 3 minutes; (7) Running cold tap water to rinse.

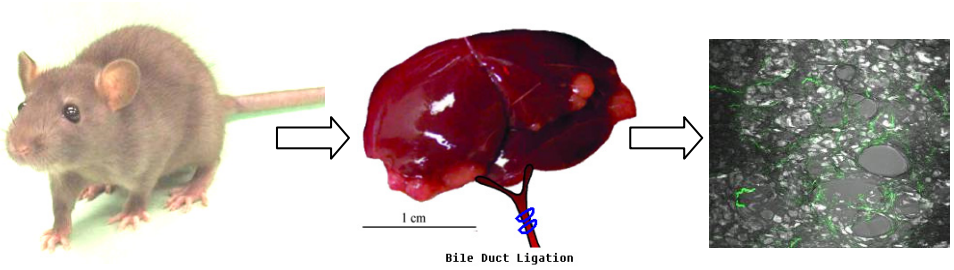

Fig. 5.4 Illustration of a bile duct ligation (BDL) rat modal for fibrotic liver disease. The SHG signals (green) are from collagen fibrils, and CARS signals (white) represent hepatic fats.

5.2.2 Results and discussions

BDL surgery is usually considered to be an effective approach for inducing of liver fibrosis diseases. Due to the close relationship between liver steatosis and liver fibrosis, it would be interesting to study the possible accumulation of hepatic fats, in addition to the aggregated collagens in BDL model using multimodal nonlinear imaging modality, to reveal their clinical correlations for the purpose of liver disease diagnosis.

5.2.2.1 Multimodal imaging of fibrotic liver tissue

The integrated CARS and multiphoton microscope developed was applied for fibrotic liver tissues. Fig. 5.5 shows the comparison between (a) normal liver and (b) BDL induced fibrotic liver tissue. It is clear that in normal tissue, there were few collagens and hepatic fat droplets, while in diseased liver tissue, a lot of aggregated collagen fibers and hepatic fat droplets were directly visualized by SHG and CARS,

respectively, in a label-free manner [198].

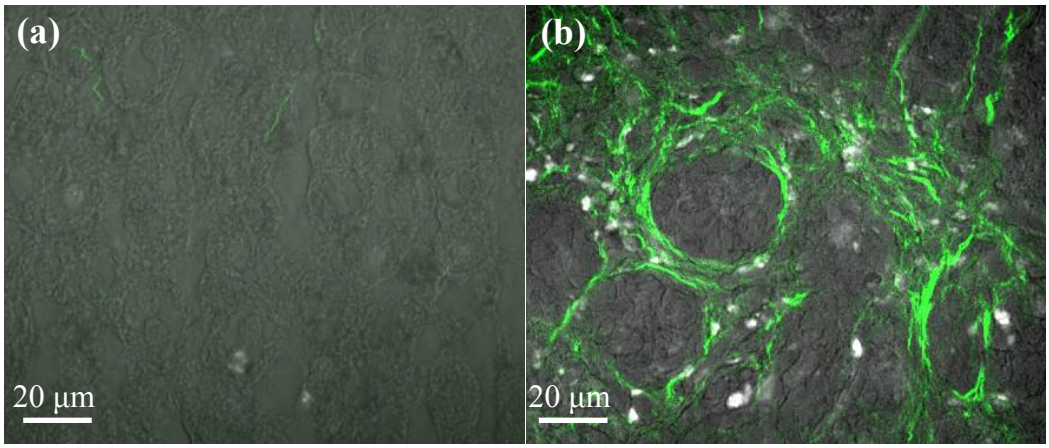

Fig. 5.5 Comparison of normal (a) and BDL induced fibrotic rat liver tissue (b). Many aggregated collagen fibers (Green) were generated in diseased liver, and some hepatic fat droplets were also observed (Gray). However, in normal liver, there are few collagens and hepatic fats.

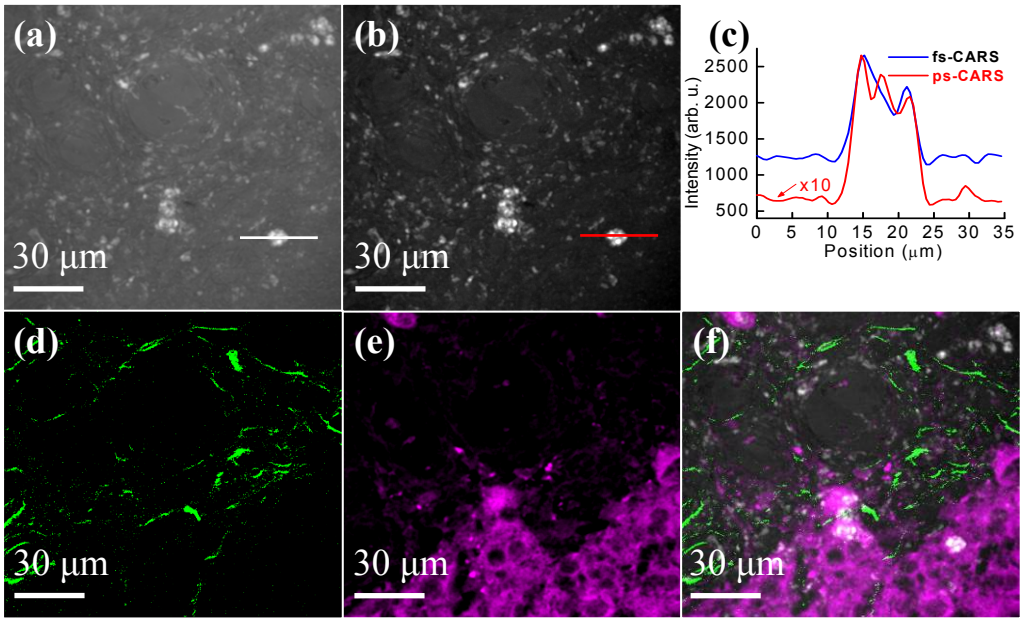

Fig. 5.6 fs-CARS image (a) and ps-CARS image (b) of the lipid droplets in a 50 μm sectioned fibrotic liver tissue, and (c) shows the corresponding intensity profiles along the lines in Figs. (a, b). (d) SHG image, (e) TPEF image, and (f) the merged image of (b), (d) and (e). The average powers of the pump and Stokes beams are 6 and 3 mW, respectively, for both fs-CARS and ps-CARS imaging, while the average power of the laser beam at 800 nm for SHG and TPEF imaging is about 10 mW.

Figure 5.6 shows an example of the multimodal nonlinear optical imaging (CARS, TPEF, and SHG) acquired from a sectioned fibrotic liver tissue induced by bile duct ligation (BDL) in a rat model. The hepatic lipid droplets occurring in rat liver tissue were clearly identified in both fs- and ps-CARS images (symmetric CH_2 stretch vibration of hepatic lipids at 2840 cm^{-1}) as shown in Figs. 5.6(a, b), but ps-CARS imaging gives a higher vibrational contrast (of ~4:1) compared to fs-CARS (vibrational contrast of ~2:1) as depicted in Fig. 5.6(c) (the corresponding intensity profiles across the lines indicated in the CARS images (Figs. 5.6(a, b))). The lipid droplet distributions and variations inside the hepatic cells could be observed more clearly in ps-CARS imaging due to its improved sensitivity and spectral resolution (Fig. 5.6(c)). When swapping the dual 4-f grating filtering from the ps mode to fs mode, the multiphoton microscopy images of the same tissue in tandem could be measured. The SHG image and TPEF image of fibrotic liver tissue excited by the 100 fs laser light at 800 nm are shown in Figs. 5.6(d) and 5.6(e), respectively. The dense while aggregated fibril collagen were clearly identified by SHG signals of fibrotic liver tissue (Fig. 5.6(d)); however, very weak SHG signals of collagen fibers can be detected in normal liver tissue (Fig. 5.5(a)). The hepatocyte morphology was also observed by TPEF signals arising from NAD(P)H and flavins' autofluorescence in liver tissue (Fig. 5.6(e)). The merged image of ps-CARS, SHG and TPEF of liver tissue (Fig. 5.6(f)) reveals that the collagen fibers were more preferentially produced in the areas where the hepatocytes were damaged, whereas the distribution of hepatic lipid droplets did not show the similar trend in fibrotic liver tissue. Hence, the integrated CARS microscopy and

multiphoton microscopy could be used for label-free imaging of significant biochemical components and structures of liver tissues with potential for monitoring the onset and progression of liver disease.

5.2.2.2 Quantitative assessment of hepatic fats and aggregated collagens

Both resonant and nonresonant CARS signals can contribute to the overall imaging intensities [143]. To assess their relative contributions, resonant and nonresonant CARS images of the same sample were acquired as shown in Fig. 5.7. It is observed that the intensity of the resonant image (Fig. 5.7(a)) was much stronger than the nonresonant one (Fig. 5.7(b)). In addition, lipid droplets could be clearly revealed in resonant image, while the nonresonant image is lack of appreciable contrast, indicating that the nonresonant background may affect little on the quantitative analysis, especially for lipid droplets due to their relatively high density in targeted chemical bonds (CH_2).

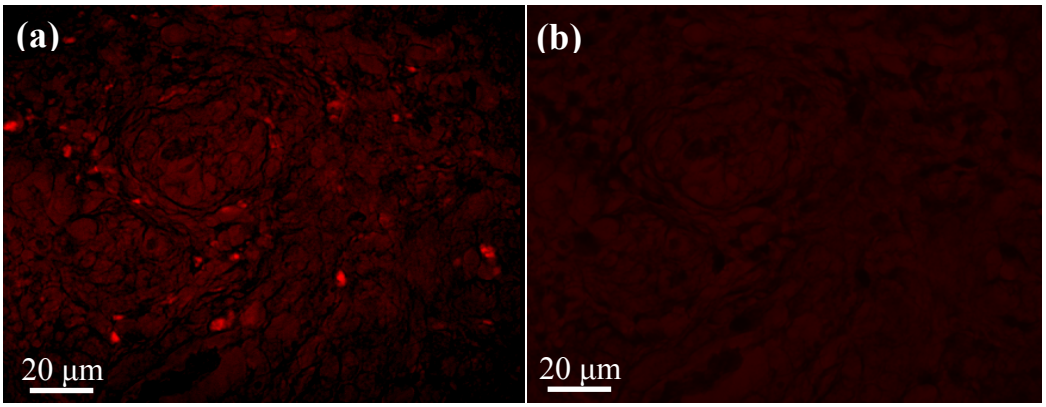

Fig. 5.7 CARS images of the same area of a fibrotic liver tissue sample. (a), Resonant at 2840 cm^{-1} corresponding to CH_2 stretching vibration in lipids, and (b), nonresonant at 2940 cm^{-1}.

In order to validate that the contrast revealed by CARS is really from hepatic lipid droplets, both CARS and TPEF imaging were performed on a fat-specific

ORO-stained liver tissue sample, as shown in Fig. 5.8. The bright spots in the two images were highly coincident with each other, confirming that CARS microscopy can realize chemical selective imaging for lipids.

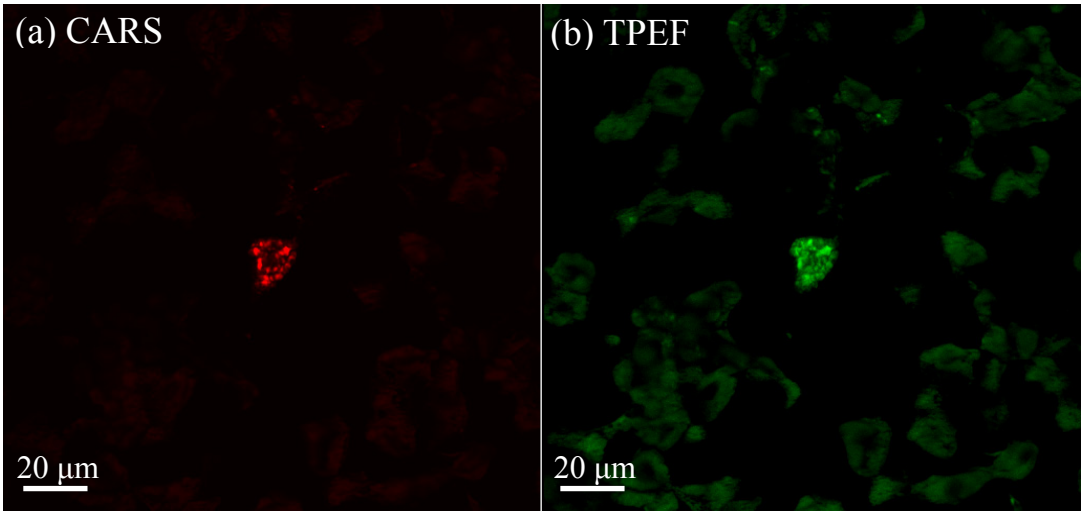

Fig. 5.8 Hepatic fat droplets in fibrotic liver tissue imaged by both CARS (a) and TPEF (b). The fats or lipid droplets were stained using Oil Red O (ORO) fluorescence dye.

An image-based algorithm to extract the hepatic fat content was proposed for accurately quantitative analysis of lipids as shown in Fig. 5.9. First of all, a digital mask image (Figs. 5.9(a, d)) was generated according to the original CARS image of a fibrotic liver sample (Figs. 5.9(b, e)). Specifically, the intensity of the pixels in the digital mask image was defined as 1 if the intensity of the original image was larger than the threshold, otherwise 0 if the intensity was equal or smaller than the threshold. The value of the threshold was determined by analyzing the intensities from relatively smaller lipid droplets. Secondly, the logic operation of 'and' was performed between the digital mask image and the original image to get the processed image only containing the hepatic fat droplets with the original intensities (Figs. 5.9(c, f)). This

method could effectively remove the background signals from non-droplet areas for quantitative assessment.

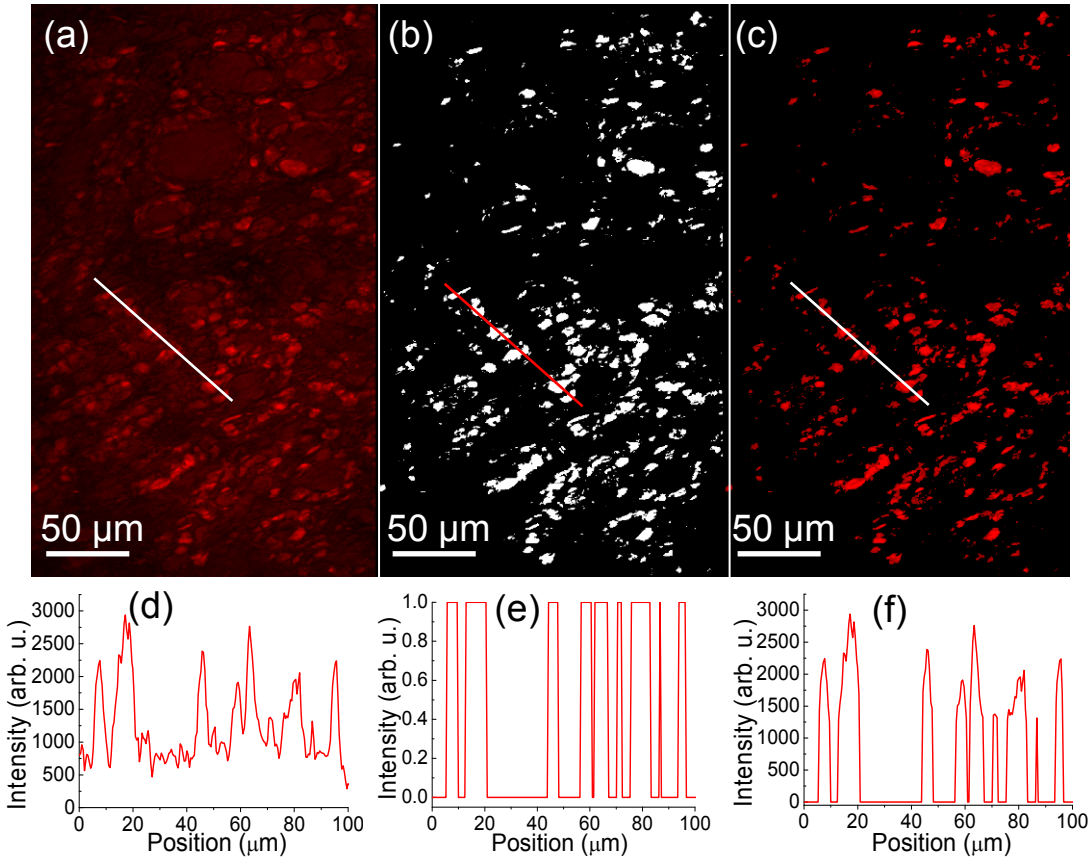

Fig. 5.9Digital mask processing for quantitative assessment of lipid droplets in CARS imaging in diseased liver tissue. (a) Digital mask image, (b) original CARS image, and (c) processed background-free lipid droplets image. The intensity profiles along the line in Figs. (a-c) are displayed in Figs. (d-f), respectively.

It has been proved that resonant CARS intensity is quadratically proportional to the content of hepatic fats [143], while the intensity of SHG can reflect the concentration of collagen (type I) (i.e., the larger the SHG signals, the higher concentration of the collagens) [199]. Figure 3 shows the quantitative assessment of contents of the lipid droplets and collagen fibrils for the BDL rat liver at the time intervals of 2, 4, and 6 weeks. Week-0 denotes the control group. It is clear that more

collagens were generated in the BDL rat livers along the living time of the rats, indicating that liver fibrosis became more and more serious. However, lipid droplets increased until week-4 and then seemed to stop increasing at week-6. The contents of lipid droplets and collagens show a very high correlation factor (R^2=0.96) for week-0, -2 and -4, while the correlation factor became low when calculating until week-6 (R^2=0.78), demonstrating that in the BDL rat liver, fibrosis and steatosis may develop with close relationship but progress in different paces.

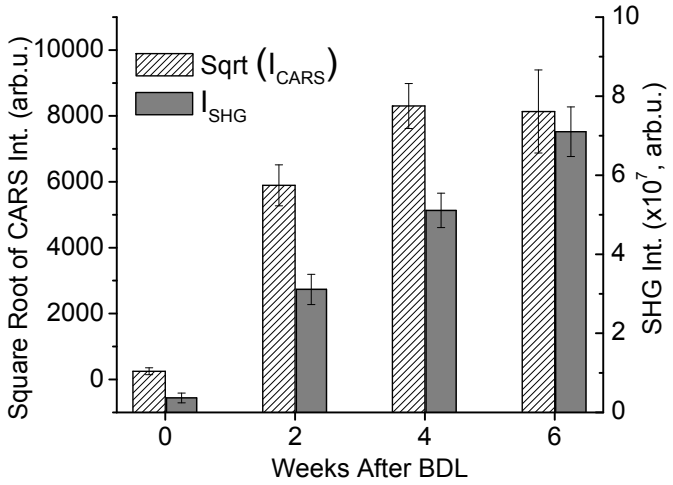

Fig. 5.10. Quantitative assessment of hepatic fat droplets by CARS and collagen fibrils by SHG imaging in the BDL rat model. Week-0 represents the control group, and week-2, -4 and -6 denote rat liver diseased progression at different stages after BDL surgery. The data were averaged from 5 different randomly decided imaging locations on each liver specimen. For each location, 30 sliced images (300 $\times$ 300 μm) were acquired from 10-μm tissue in thickness.

5.2.3 Summary

Preliminary results showed that the multimodal nonlinear optical microscopy technique developed possessed sufficient sensitivity and specificity, and appropriate dynamic ranges for the determination of fiber collagen and hepatic fat changes in liver disease models at various stages of progression, demonstrating the excellent capability

of CARS/SHG/TPEF techniques for monitoring and quantification of fatty liver and liver fibrosis without staining. Multimodal nonlinear optical imaging approach indicated applicable potential for exploring the pathological and clinical correlations between the two liver diseases.

Chapter 6 Conclusions and Future Directions

6.1 Conclusions

In this work, a number of novel polarization-encoded CARS microscopy techniques have been developed, including (i) interferometric polarization CARS, (ii) phase-controlled P-CARS, (iii) heterodyne polarization CARS, (iv) elliptically polarized CARS, and (v) radially polarized CARS, to effectively remove the nonresonant background while simultaneously improving the resonant CARS signals for high contrast and high sensitive vibrational imaging in biological/biomedical systems. In addition, an integrated CARS and multiphoton microscopic technique was developed based on a novel implementation of a dual 4-f paired-gratings spectral filtering module of a femtosecond laser source to realize both high contrast picosecond CARS and high quality femtosecond multiphoton (SHG, and TPEF, etc.) imaging on the same platform for quantitative assessment of liver fibrotic disease in a BDL rat model.

More specifically, the interferometric polarization CARS (IP-CARS) imaging technique was demonstrated for effectively suppressing the nonresonant background while significantly amplifying the resonant signal for label-free vibrational imaging. By modulating the phase difference between the two interference CARS signals generated from the same sample, and measuring the peak-to-peak intensity of the periodically modulated interference CARS signal, the IP-CARS technique yielded a 6-fold improvement in signal-to-background ratio compared to the conventional CARS, while providing an approximately 20-fold amplification of resonant CARS signal with

2-fold improvement of signal-to-noise-ratio (SNR) compared to the conventional P-CARS. The IP-CARS technique provided the potential for detecting weak signals of various biochemical species in biological systems for higher contrast, molecular vibrational imaging. The SNR of this technique could be further improved by utilizing a lock-in amplifier detection scheme.

Without the need of fast phase modulation for heterodyne detection in IP-CRAS, phase-controlled polarization CARS was proposed and demonstrated to realize background-free CARS imaging. The directly digital subtraction between the constructive and destructive interference CARS images yielded a 5-fold improvement in signal-to-background ratios compared with conventional CARS, while provided an approximately 20-fold amplification of resonant CARS signal compared with conventional polarization CARS imaging. It is expected that phase controlled P-CARS may play a more active role than P-CARS microscopy in probing weak signals of certain biologically relevant molecules at lower concentrations in biological/ biomedical systems.

To further reduce the excitation power for minimizing the photodamage to the specimens, only single pump-Stokes beam was used to excite the sample for heterodyne detection on polarization CARS signals. This heterodyne polarization (HP-CARS) technique utilized interference of the relatively intense local CARS signal and the weak resonant CARS signal generated simultaneously within the focal volume of the sample of conventional P-CARS for heterodyne detection. HP-CARS yielded an approximately 7-fold improvement in vibrational contrast compared to the

conventional CARS, while exhibited a 12-fold amplification on the resonant signal compared to the P-CARS.

Employing an elliptically polarized pump field with an aspect ratio of $1:\sqrt{3}$ of the ellipse combined with a linearly polarized Stokes field, intrinsic background-free CARS imaging was realized. This elliptically polarized CARS (EP-CARS) microscopy technique brought a 6-7-fold improvement in signal-to-background ratios compared with normal CARS, while provided an approximately 1.25-fold improvement in resonant CARS signal compared with normal polarization-sensitive CARS microscopy. It was demonstrated that this technique was capable of imaging 1.5 μm polystyrene beads in water and lipid droplets in unstained fibroblast cells.

CARS microscopy with radial polarization illumination has also been studied both theoretically and experimentally. A novel annular aperture detection scheme was proposed in radially polarized (RP-) CARS to significantly remove the nonresonant background for high contrast vibrational imaging. Finite-difference time-domain (FDTD) calculations showed that the maximum radiation patterns of RP-CARS signals from the scatterers vary with the scatterer's sizes, which are different from nonresonant CARS radiation from surrounding water. By applying appropriate sizes of annular stop apertures in the detection path, the nonresonant background from water could be effectively suppressed, yielding over 110-fold improvements in signal-to-background ratio (SBR) for the forward-detected RP-CARS, while over 50-fold improvements for the backward RP-CARS detection. In the future study, experimental realization of annular detection in CARS could be performed to evaluate its practical ability on

nonresonant background suppression and explore its potential application in cellular imaging.

RP-CARS microscopy for facilitating longitudinally oriented molecules detection was also demonstrated. It was observed that under a tight focusing of the radially polarized pump and Stokes light fields with a high NA objective, RP-CARS radiations from molecules oriented along the longitudinal direction were approximately 3-fold stronger than those using linearly polarized CARS technique, and the lateral resolution of RP-CARS imaging could be improved by about 10% compared to the linearly polarized CARS imaging.

In addition, a unique implementation of a dual 4-f configured paired-gratings spectral filtering of a femtosecond (fs) laser source to realize high CARS microscopy and high quality multiphoton microscopy on the same platform for label-free biomolecular imaging was demonstrated. The 4-f gratings filtering enabled ready conversion of the 100 fs laser pulse trains into transform-limited 1 picosecond (ps) pulses in the spectral range of 700-1600 nm with a power conversion efficiency of ~ 6 to 8%, which is sufficient for CARS imaging. Compared with fs-CARS microscopy, the ps-CARS imaging offered an approximately 10-fold improvement in spectral resolution, while a 2-fold improvement in nonresonant background suppression. High quality second-harmonic generation (SHG) and two-photon excitation fluorescence (TPEF) imaging can also be acquired in tandem when swapping the 4-f grating filtering from the ps mode to fs mode. The multimodal system was applied for fibrotic liver tissue imaging for disease diagnosis.

The multimodal system was applied to investigate the contents of hepatic fats by CARS, aggravated collagen by SHG and hepatocyte morphology by TPEF in a rat liver disease model induced by bile duct ligation (BDL) surgery. The multimodal imaging of the same liver tissue sample revealed the coexistence of both hepatic fat and aggravated collagen with submicron three-dimensional spatial resolutions in a label-free manner, indicating that there exists a close relationship between liver steatosis and fibrosis diseases. Quantitative assessment of the contents of the hepatic fats and collagen versus the growing time of the rats appeared to have a certain correlation (R^2= ~0.65) between each other. This result may provide a new perspective that is helpful for liver disease diagnosis and clinical research and managements.

6.2 Future Directions

This thesis work confirms that the integrated CARS microscopy and multiphoton microscopy is a powerful tool for label-free quantitative assessment of biomolecular and biochemical constituents in biological and biomedical systems. Looking into the future, there are several research directions warranting further exploration for the wide spread of label-free biomolecular imaging techniques, particularly in the Life Sciences.

i). Multimodal nonlinear optical microscopy imaging for disease diagnosis

Multimodal nonlinear optical microscope integrating CARS, SHG, TPEF, THG, SFG, and Raman techniques would find more applications in biological and biomedical research. As preliminarily demonstrated in this thesis, multimodal nonlinear optical imaging could be used for disease diagnosis (e.g., liver fibrosis, fatty liver), especially useful for revealing the close relationship between liver steatosis and liver fibrosis

diseases. By further advancing the available multimodal imaging and Raman spectroscopy platform with radial/linear polarization-encoded light excitation scheme, high sensitive 3-D molecular imaging with improved spatial and spectral resolution can be realized to explore the origins of molecular orientations associated with liver disease transformations (e.g., lipid orientations versus hepatic steatosis; collage fibrils orientation versus liver fibrosis). In addition, many other lipid/collagen related human diseases, such as angiocardiopathy, encephalopathy, and carcinoma can also be studied (typing and staging) by multimodal nonlinear optical imaging approach.

ii). Super-resolution in CARS microscopy

Although CARS microscopy has the capability of realizing chemical specificity and functional imaging of individual molecule without labeling, the diffraction limit in common optical components prevents researchers from resolving features smaller than half a wavelength of the light applied. The conventional super-resolution instruments including scanning electron microscope (SEM) and scanning near-field optical microscope (SNOM) have demonstrated the ability to image the morphology structures of biomaterials ranging from individual atoms to proteins, but these techniques are unable to provide the information about biochemical structure and composition of the specimens. As a future direction, to integrate CARS/Raman techniques into a tip-enhanced near-field scanning platform would provide novel nano-CARS imaging and nano-Raman spectroscopy techniques with both high chemical specificity and sensitivity that can be extensively used in many fields such as bioengineering, biosciences, biomaterials and biomedicine for molecular and functional nano-imaging.

The near-field CARS/Raman microspectroscopy will be particularly advantageous in imaging and spectrally analyzing small molecules such as DNA/RNA, proteins/lipids, hormones, and drug molecules, and small cellular organelles and structures (e.g., membrane, mitochondria, etc.), for which fluorescence labeling is prone to alter their normal functions in cells and tissues. On the other hand, integrating the CARS technique with the stimulated emission depletion (STED) microscopy will be another very interesting topic to explore for beating the diffraction-limitation while providing biomolecular information without labeling in biomedical research.

iii). Stimulated Raman scattering microscopy

Very recently, stimulated Raman scattering (SRS) has been demonstrated to be an intrinsic background free technique for label-free vibrational imaging by detecting the stimulated Raman loss (SRL) in the pump beam or the stimulated Raman gain (SRG) in the Stokes beam with radio-frequency lock-in modulation and detection [200, 201]. SRS microscopy has the major advantage over CARS in that it offers an intrinsic nonresonant background-free imaging ability and readily interpretable chemical contrast. Note that it would be easy to build a SRS microscopy on the available CARS modality. Based on the wealth of Raman spectroscopy, SRS microscopy can be an attractive approach for detecting weak Raman resonances from biochemical compounds in low concentrations inside living cells or tissues.

iv). Translational clinical research: CARS endoscopy

The cost and complexity of ultrafast pulsed laser sources are still the main prohibitive factor from wide applications of coherent Raman microscopy in biological and

biomedical areas. Potentially, fiber-based ultrafast lasers may offer great promising possibility for compact, portable, and low-cost CARS system to be applicable in many research laboratories, ranging from very basic biological and biophysics labs to biomedical and even clinical imaging in the hospitals [49-51]. Towards translational clinical research, the development of CARS endoscopy for in vivo diagnosis is expected to be a very exciting direction [137, 202]. It is anticipated that CARS endoscopy coupled with other existing optical modalities, such as optical coherent tomography (OCT) and wide-field fluorescence endoscopic imaging would create a multimodal imaging approach that is capable of providing both morphologic structure and biochemical information about tissue for advancing clinical disease diagnosis.

List of Publications

Peer-Reviewed Journal Articles

1. Jian Lin, **Fake Lu**, Wei Zheng, Zhiwei Huang, "Annular aperture-detected coherent anti-Stokes Raman scattering microscopy for high contrast vibrational imaging," ***Applied Physics Letters***, accepted (2010).
2. Chao Fang, **Fake Lu**, Wei Zheng, and Zhiwei Huang, "Triple-frequency symmetric subtraction scheme for nonresonant background suppression in coherent anti-Stokes Raman scattering (CARS) microscopy," ***Optics Express*** **18**, 15714 (2010).
3. **Fake Lu**, Wei Zheng, Jian Lin, Zhiwei Huang, "Integrated coherent anti-Stokes Raman scattering and multiphoton microscopy for biomolecular imaging using spectral filtering of a femtosecond laser," *Applied Physics Letters* **96**, 133701 (2010).
4. **Fake Lu**, Wei Zheng, and Zhiwei Huang, "Coherent anti-Stokes Raman scattering microscopy using tightly focused radially polarized light," *Optics Letters* **34**, 1870 (2009).
5. Jian Lin, **Fake Lu**, Haifeng Wang, Wei Zheng, Colin Sheppard, and Zhiwei Huang, "Improved contrast radially polarized coherent anti-Stokes Raman scattering microscopy using annular aperture detection," *Applied Physics Letters* **95**, 133703 (2009).
6. Jian Lin, Haifeng Wang, Wei Zheng, **Fake Lu**, Colin Sheppard, and Zhiwei Huang, "Numerical study of effects of light polarization, scatterer sizes and orientations on near-field coherent anti-Stokes Raman scattering microscopy," *Optics Express* **17**, 2423 (2009).
7. **Fake Lu**, Wei Zheng, and Zhiwei Huang, "Elliptically polarized coherent anti-Stokes Raman scattering microscopy", *Optics Letters* **33**, 2842 (2008).
8. **Fake Lu**, Wei Zheng, and Zhiwei Huang, "Phase-controlled polarization coherent anti-Stokes Raman scattering microscopy for high-sensitivity and high-contrast molecular imaging", *Journal of the optical Society of America B* **25**, 1907 (2008)
9. **Fake Lu**, Wei Zheng, Colin Sheppard, and Zhiwei Huang, "Interferometric polarization coherent anti-Stokes Raman scattering (IP-CARS) microscopy", *Optics Letters* **33**, 602 (2008).
10. **Fake Lu**, Wei Zheng, and Zhiwei Huang, "Heterodyne polarization coherent anti-Stokes Raman scattering microscopy", *Applied Physics Letters* **92**, 123901 (2008).
11. Cheng Liu, Zhiwei Huang, **Fake Lu**, Wei Zheng, Dietmar W. Hutmacher, and Colin Sheppard, "Near-field effects on coherent anti-Stokes Raman scattering microscopy imaging", *Optics Express* **15**, 4118 (2007).

Conference Proceedings

1. **Fake Lu**, Wei Zheng, Zhiwei Huang, "Novel coherent anti-stokes Raman scattering microscopy for high contrast bioimaging," Proc. SPIE, Vol. 6826, 68260Y (2007). SPIE/COS Photonics Asia 2007, 11-15 November 2007, Beijing China.
2. **Fake Lu**, Wei Zheng, Zhiwei Huang, "High contrast bioimaging using interferometric polarization coherent anti-Stokes Raman scattering microscopy," Proc. SPIE Vol. 6860, 68600Z (2008). SPIE/BIOS Photonics West, 19-24 January, 2008, San Jose, CA, USA.
3. **Fake Lu**, Wei Zheng, Zhiwei Huang, "Heterodyne polarization coherent anti-Stokes Raman scattering (HP-CARS) microscopy for high contrast bioimaging," Biomedical Optics (BIOMED), OSA Technical Digest (CD) (OSA 2008), paper PDPBSuE2. 16-20 March, 2008, St. Petersburg, Florida, USA.
4. **Fake Lu**, Jian Lin, Wei Zheng, Zhiwei Huang, (*Invited*) "Coherent anti-Stokes Raman scattering (CARS) microscopy for sensing molecular orientations," Asia Communications and Photonics Conference and Exhibition (ACP 2009), Technical Digest (CD) (OSA 2009), paper FV2. 2-6 November, 2009, Everbright Convention & Exhibition Center, Shanghai, China.
5. Zhiwei Huang, **Fake Lu**, Wei Zheng, "Elliptically polarized coherent anti-Stokes Raman scattering (EP-CARS) microscopy for high contrast vibrational imaging," Novel Techniques in Microscopy, OSA Technical Digest (CD) (OSA 2009), paper NMC5. Novel Techniques in Microscopy (NTM), 26-30 April 2009, Vancouver, Canada.

Conference Presentations

6. **Fake Lu**, Wei Zheng, Dean CS Tai, Jian Lin, Hanry Yu, and Zhiwei Huang, "Assessment of fibrotic liver disease with multimodal nonlinear optical microscopy," SPIE/BIOS Photonics West: Biomedical Optics, paper number 7569-61, 23-28 January 2010, San Francisco, California, USA. Scheduled for oral presentation on 26 January 2010.
7. Jian Lin, **Fake Lu**, Wei Zheng, Zhiwei Huang, "Annular-aperture detection scheme in radially polarized coherent anti-Stokes Raman scattering (RP-CARS) microscopy for vibrational contrast enhancement," SPIE/BIOS Photonic West: Biomedical Optics, paper number 7569-88, 23-28 January 2010, San Francisco, California, USA.
8. **Fake Lu**, Wei Zheng, Zhiwei Huang, "Radial polarization coherent anti-Stokes Raman scattering microscopy facilitates detection of longitudinally oriented molecules," 5-8 April 2009, Focus on Microscopy 2009 (FOM 2009), Krakow, Poland.

9. **Fake Lu**, Wei Zheng, Zhiwei Huang, "Heterodyne polarization coherent anti-Stokes Raman scattering (HP-CARS) microscopy for high contrast bioimaging," 1st European conference on CARS microscopy (MicroCARS 2008), Abstract Book: CT9, May 25-27, 2008, Igls, Austria. (2008)
10. Haifeng Wang, Zhiwei Huang, Luping Shi, Jian Lin, **Fake Lu**, Towchong Chong and Colin Sheppard, Polarization Encoded Coherent Anti-Stokes Raman Scattering Microscopy Abstract Book, P27, Optics Within Life Sciences-10 (OWLS-10), BIOPHOTONICS ASIA 2008, From Bench Top to Clinical Practice, 2 to 4 July 2008, SMU Conference Centre, Singapore. (2008)
11. **Fake Lu**, Wei Zheng and Zhiwei Huang, "Phase-Modulated Polarization Coherent Anti-Stokes Raman Scattering Microscopy For Molecular Vibration Imaging," Abstract Book, P26, Optics Within Life Sciences-10 (OWLS-10), BIOPHOTONICS ASIA 2008, From Bench Top to Clinical Practice, 2 to 4 July 2008, SMU Conference Centre, Singapore. (2008)
12. **Fake Lu**, Wei Zheng, Zhiwei Huang, "(*Invited*) Novel Heterodyne-Detection Polarization Coherent Anti-Stokes Raman Scattering Microscopy for High Contrast Molecule Imaging," 3rd Tohoku-NUS Joint Symposium on Nano-Biomedical Engineering in the East Asian-Pacific Rim Region, Dec 2007 (4th International Symposium of Tohoku University Global COE Programme Global Nano-Biomedical Engineering Education and Research Network Centre), Abstract Book Pg. 93, 10-11 December 2007, Singapore, Centre for Life Sciences (CELS), National University of Singapore. (2007)

References

1. J. P. Rigaut and J. Vassy, "High resolution 3-dimensional images from confocal scanning laser microscoy - Quantitative study and mathematical correlation of the effects from bleaching and fluorescence attenuation in depth," Anal. Quant. Cytol. Histol. **13**, 223-232 (1991).
2. M. R. Arnison, K. G. Larkin, C. J. R. Sheppard, N. I. Smith, and C. J. Cogswell, "Linear phase imaging using differential interference contrast microscopy," J. Microsc. **214**, 7-12 (2004).
3. R. D. Allen, N. S. Allen, and J. L. Travis, "Video-enhanced contrast, differential interference contrast (AVEC-DIC) microscopy - a new method capable of analyzing microtubule-related motility in the recticulopodial network of allogromia laticollaris," Cell Motil. Cytoskeleton **1**, 291-302 (1981).
4. K. Kneipp, H. Kneipp, I. Itzkan, R. R. Dasari, and M. S. Feld, "Ultrasensitive chemical analysis by Raman spectroscopy," Chem. Rev. **99**, 2957 (1999).
5. Z. Huang, A. McWilliams, H. Lui, D. I. McLean, S. Lam, and H. Zeng, "Near-infrared Raman spectroscopy for optical diagnosis of lung cancer," Int. J. Cancer **107**, 1047-1052 (2003).
6. S. K. Teh, W. Zheng, D. P. Lau, and Z. Huang, "Spectroscopic diagnosis of laryngeal carcinoma using near-infrared Raman spectroscopy and random recursive partitioning ensemble techniques," Analyst **134**, 1232-1239 (2009).
7. C. Yuen, W. Zheng, and Z. Huang, "Improving surface-enhanced Raman scattering effect using gold-coated hierarchical polystyrene bead substrates modified with postgrowth microwave treatment," J. Biomed. Opt. **13**, 064040 (2008).
8. B. R. Masters and P. T. C. So, *Handbook of biomedical nonlinear optical microscopy* (Oxford University Press, Oxford, 2008).
9. A. Zoumi, A. Yeh, and B. J. Tromberg, "Imaging cells and extracellular matrix in vivo by using second-harmonic generation and two-photon excited fluorescence," Proc. Natl. Acad. Sci. U. S. A. **99**, 11014-11019 (2002).
10. W. R. Zipfel, R. M. Williams, R. Christie, A. Y. Nikitin, B. T. Hyman, and W. W. Webb, "Live tissue intrinsic emission microscopy using multiphoton-excited native fluorescence and second harmonic generation," Proc. Natl. Acad. Sci. U. S. A. **100**, 7075-7080 (2003).
11. R. Carriles, D. N. Schafer, K. E. Sheetz, J. J. Field, R. Cisek, V. Barzda, A. W. Sylvester, and J. A. Squier, "Invited Review Article: Imaging techniques for harmonic and multiphoton absorption fluorescence microscopy," Rev. Sci. Instrum. **80**, (2009).
12. P. J. Campagnola, M. D. Wei, A. Lewis, and L. M. Loew, "High-resolution nonlinear optical imaging of live cells by second harmonic generation," Biophys. J. **77**, 3341-3349 (1999).
13. P. J. Campagnola, A. C. Millard, M. Terasaki, P. E. Hoppe, C. J. Malone, and W. A. Mohler, "Three-dimensional high-resolution second-harmonic

generation imaging of endogenous structural proteins in biological tissues," Biophys. J. **82**, 493-508 (2002).
14. D. Debarre, A. M. Pena, W. Supatto, T. Boulesteix, M. Strupler, M. P. Sauviat, J. L. Martin, M. C. Schanne-Klein, and E. Beaurepaire, "Second- and third-harmonic generation microscopies for the structural imaging of intact tissues," Med. Sci. (Paris) **22**, 845-850 (2006).
15. J. A. Squier, M. Muller, G. J. Brakenhoff, and K. R. Wilson, "Third harmonic generation microscopy," Opt. Express **3**, 315-324 (1998).
16. D. Debarre, W. Supatto, A. M. Pena, A. Fabre, T. Tordjmann, L. Combettes, M. C. Schanne-Klein, and E. Beaurepaire, "Imaging lipid bodies in cells and tissues using third-harmonic generation microscopy," Nat. Methods **3**, 47-53 (2006).
17. E. B. K. Lawrence S. Friedman, *Handbook of liver disease, 2nd edition* (Churchill Livingstone, 2004).
18. A. Zumbusch, G. R. Holtom, and X. S. Xie, "Three-dimensional vibrational imaging by coherent anti-Stokes Raman scattering," Phys. Rev. Lett. **82**, 4142-4145 (1999).
19. J. Zhu, B. Lee, K. K. Buhman, and J. X. Cheng, "A dynamic, cytoplasmic triacylglycerol pool in enterocytes revealed by ex vivo and in vivo coherent anti-Stokes Raman scattering imaging," J. Lipid Res. **50**, 1080-1089 (2009).
20. P. D. Maker and R. W. Terhune, "Study of optical effects due to an induced polarization third order in the Electric Field strength," Phys. Rev. A **137**, (1965).
21. B. Hudson, W. Hetherington, 3rd, S. Cramer, I. Chabay, and G. K. Klauminzer, "Resonance enhanced coherent anti-Stokes Raman scattering," Proc. Natl. Acad. Sci. U. S. A. **73**, 3798-3802 (1976).
22. J.-L. Oudar, R. W. Smith, and Y. R. Shen, "Polarization-sensitive coherent anti-Stokes Raman spectroscopy," Appl. Phys. Lett. **34**, 758-760 (1979).
23. F. M. Kamga and M. G. Sceats, "Pulse-sequenced coherent anti-Stokes Raman scattering spectroscopy: a method for suppression of the nonresonant background," Opt. Lett. **5**, 4 (1980).
24. M. D. Duncan, J. Reintjes, and T. J. Manuccia, "Scanning coherent anti-Stokes Raman scattering microscope," Opt. Lett. **7**, 350-352 (1982).
25. J.-x. Cheng, A. Volkmer, L. D. Book, and X. S. Xie, "An Epi-Detected Coherent Anti-Stokes Raman Scattering (E-CARS) Microscope with High Spectral Resolution and High Sensitivity," J. Phys. Chem. B **105**, 1277-1280 (2001).
26. J. X. Cheng, Y. K. Jia, G. Zheng, and X. S. Xie, "Laser-scanning coherent anti-Stokes Raman scattering microscopy and applications to cell biology," Biophys. J. **83**, 502-509 (2002).
27. J. X. Cheng, E. Potma, and S. X. Xie, "Coherent anti-Stokes Raman scattering correlation spectroscopy: Probing dynamical processes with chemical selectivity," J. Phys. Chem. A **106**, 8561-8568 (2002).

28. J. X. Cheng, A. Volkmer, and X. S. Xie, "Theoretical and experimental characterization of coherent anti-Stokes Raman scattering microscopy," J. Opt. Soc. Am B **19**, 1363-1375 (2002).
29. J. X. Cheng, L. D. Book, and X. S. Xie, "Polarization coherent anti-Stokes Raman scattering microscopy," Opt. Lett. **26**, 1341-1343 (2001).
30. F. C. V. Raman, "A new radiation," Indian J. Phys. **2**, 12 (1928).
31. A. Y. Tu, *Raman spectroscopy in biology: principles & Applications* (Wiley, 1982).
32. H. X. Xu, E. J. Bjerneld, M. Kall, and L. Borjesson, "Spectroscopy of single hemoglobin molecules by surface enhanced Raman scattering," Phys. Rev. Lett. **83**, 4357-4360 (1999).
33. Z. Huang, H. Zeng, I. Hamzavi, D. I. McLean, and H. Lui, "Rapid near-infrared Raman spectroscopy system for real-time in vivo skin measurements," Opt. Lett. **26**, 1782-1784 (2001).
34. Z. Huang, A. McWilliams, S. Lam, J. English, D. I. McLean, H. Lui, and H. Zeng, "Effect of formalin fixation on the near-infrared Raman spectroscopy of normal and cancerous human bronchial tissues," Int. J. Oncol. **23**, 649-655 (2003).
35. S. K. Teh, W. Zheng, K. Y. Ho, M. Teh, K. G. Yeoh, and Z. Huang, "Near-infrared Raman spectroscopy for optical diagnosis in the stomach: Identification of Helicobacter-pylori infection and intestinal metaplasia," Int. J. Cancer (2009).
36. Z. Huang, H. Lui, X. K. Chen, A. Alajlan, D. I. McLean, and H. Zeng, "Raman spectroscopy of in vivo cutaneous melanin," J. Biomed. Opt. **9**, 1198-1205 (2004).
37. Z. Huang, H. Lui, D. I. McLean, M. Korbelik, and H. Zeng, "Raman spectroscopy in combination with background near-infrared autofluorescence enhances the in vivo assessment of malignant tissues," Photochem. Photobiol. **81**, 1219-1226 (2005).
38. D. P. Lau, Z. Huang, H. Lui, D. W. Anderson, K. Berean, M. D. Morrison, L. Shen, and H. Zeng, "Raman spectroscopy for optical diagnosis in the larynx: preliminary findings," Lasers Surg. Med. **37**, 192-200 (2005).
39. S. K. Teh, W. Zheng, K. Y. Ho, M. Teh, K. G. Yeoh, and Z. Huang, "Diagnosis of gastric cancer using near-infrared Raman spectroscopy and classification and regression tree techniques," J. Biomed. Opt. **13**, 034013 (2008).
40. D. Gachet, F. Billard, and H. Rigneault, "Coherent anti-Stokes Raman scattering in a microcavity," Opt. Lett. **34**, 1789-1791 (2009).
41. R. J. H. Clark and R. E. Hester, *Advances in non-linear spectroscopy* (Wiley, 1988).
42. D. A. Kleinman, "Nonlinear Dielectric Polarization in Optical Media," Phys. Rev. **126**, (1962).
43. C. L. Evans, E. O. Potma, M. Puoris'haag, D. Cote, C. P. Lin, and X. S. Xie, "Chemical imaging of tissue in vivo with video-rate coherent anti-Stokes

Raman scattering microscopy," Proc. Natl. Acad. Sci. U. S. A. **102**, 16807-16812 (2005).
44. J.-X. Cheng and X. S. Xie, "Coherent Anti-Stokes Raman Scattering Microscopy: Instrumentation, Theory, and Applications," J. Phys. Chem. B **108**, 827-840 (2003).
45. E. O. Potma, D. J. Jones, J. X. Cheng, X. S. Xie, and J. Ye, "High-sensitivity coherent anti-Stokes Raman scattering microscopy with two tightly synchronized picosecond lasers," Opt. Lett. **27**, 1168-1170 (2002).
46. F. Lu, W. Zheng, C. Sheppard, and Z. Huang, "Interferometric polarization coherent anti-Stokes Raman scattering (IP-CARS) microscopy," Opt. Lett. **33**, 602-604 (2008).
47. F. Ganikhanov, S. Carrasco, X. Sunney Xie, M. Katz, W. Seitz, and D. Kopf, "Broadly tunable dual-wavelength light source for coherent anti-Stokes Raman scattering microscopy," Opt. Lett. **31**, 1292-1294 (2006).
48. F. Ganikhanov, C. L. Evans, B. G. Saar, and X. S. Xie, "High-sensitivity vibrational imaging with frequency modulation coherent anti-Stokes Raman scattering (FM CARS) microscopy," Opt. Lett. **31**, 1872-1874 (2006).
49. D. A. Zheltikova and A. M. Zheltikov, "Toward all-fiber coherent anti-Stokes Raman scattering in the gas phase," Appl. Phys. B **83**, 11-16 (2006).
50. E. R. Andresen, C. K. Nielsen, J. Thogersen, and S. R. Keiding, "Fiber laser-based light source for coherent anti-Stokes Raman scattering microspectroscopy," Opt. Express **15**, 4848-4856 (2007).
51. G. Krauss, T. Hanke, A. Sell, D. Trautlein, A. Leitenstorfer, R. Selm, M. Winterhalder, and A. Zumbusch, "Compact coherent anti-Stokes Raman scattering microscope based on a picosecond two-color Er:fiber laser system," Opt. Lett. **34**, 2847-2849 (2009).
52. A. Volkmer, J. X. Cheng, and X. S. Xie, "Vibrational imaging with high sensitivity via epidetected coherent anti-Stokes Raman scattering microscopy," Phys. Rev. Lett. **87**, (2001).
53. S. A. Akhmanov, A. F. Bunkin, S. G. Ivanov, and N. I. Koroteev, "Coherent ellipsometry of Raman scattering of light," JETP Letters **25**, 5 (1977).
54. G. B. Hadjichristov, P. P. Kircheva, and N. Kirov, "Multiplex CARS spectroscopy of Rochelle salt crystal," J. Mol. Struct. **382**, 33-37 (1996).
55. C. Otto, A. Voroshilov, S. G. Kruglik, and J. Greve, "Vibrational bands of luminescent zinc(II)-octaethyl-porphyrin using a polarization-sensitive 'microscopic' multiplex CARS technique," J. Raman Spectrosc. **32**, 495-501 (2001).
56. S. Schlucker, J. Koster, M. Nissum, J. Popp, and W. Kiefer, "Structural investigations on octaethylporphyrin using density functional theory and polarization-sensitive resonance coherent anti-Stokes Raman scattering spectroscopy," J. Phys. Chem. A **105**, 9482-9488 (2001).
57. M. Muller and J. M. Schins, "Imaging the thermodynamic state of lipid membranes with multiplex CARS microscopy," J. Phys. Chem. B **106**, 3715-3723 (2002).

58. K. Ishii and H. Hamaguchi, "Picosecond time-resolved multiplex CARS spectroscopy using optical Kerr gating," Chem. Phys. Lett. **367**, 672-677 (2003).
59. K. P. Knutsen, J. C. Johnson, A. E. Miller, P. B. Petersen, and R. J. Saykally, "High spectral resolution multiplex CARS spectroscopy using chirped pulses," Chem. Phys. Lett. **387**, 436-441 (2004).
60. F. Benabid, J. C. Knight, G. Antonopoulos, and P. S. Russell, "Stimulated Raman scattering in hydrogen-filled hollow-core photonic crystal fiber," Science **298**, 399-402 (2002).
61. H. N. Paulsen, K. M. Hilligsoe, J. Thogersen, S. R. Keiding, and J. J. Larsen, "Coherent anti-Stokes Raman scattering microscopy with a photonic crystal fiber based light source," Opt. Lett. **28**, 1123-1125 (2003).
62. H. Kano and H. Hamaguchi, "Femtosecond coherent anti-Stokes Raman scattering spectroscopy using supercontinuum generated from a photonic crystal fiber," Appl. Phys. Lett. **85**, 4298-4300 (2004).
63. H. Kano and H. Hamaguchi, "Ultrabroadband (> 2500 cm^{-1}) multiplex coherent anti-Stokes Raman scattering microspectroscopy using a supercontinuum generated from a photonic crystal fiber," Appl. Phys. Lett. **86**, (2005).
64. H. Kano and H. Hamaguchi, "Near-infrared coherent anti-Stokes Raman scattering microscopy using supercontinuum generated from a photonic crystal fiber," Appl. Phys. B **80**, 243-246 (2005).
65. E. R. Andresen, V. Birkedal, J. Thogersen, and S. R. Keiding, "Tunable light source for coherent anti-Stokes Raman scattering microspectroscopy based on the soliton self-frequency shift," Opt. Express **31**, 1328-1330 (2006).
66. H. Kano and H. Hamaguchi, "Dispersion-compensated supercontinuum generation for ultrabroadband multiplex coherent anti-Stokes Raman scattering spectroscopy," J. Raman Spectrosc. **37**, 411-415 (2006).
67. H. Kano and H. O. Hamaguchi, "In-vivo multi-nonlinear optical imaging of a living cell using a supercontinuum light source generated from a photonic crystal fiber," Opt. Express **14**, 2798-2804 (2006).
68. H. Kano and H. O. Hamaguchi, "Three-dimensional vibrational imaging of a microcrystalline J-aggregate using supercontinuum-based ultra-broadband multiplex coherent anti-stokes Raman scattering microscopy," J. Phys. Chem. B **110**, 3120-3126 (2006).
69. H. Wang, T. B. Huff, and J. X. Cheng, "Coherent anti-Stokes Raman scattering imaging with a laser source delivered by a photonic crystal fiber," Opt. Lett. **31**, 1417-1419 (2006).
70. S. Murugkar, C. Brideau, A. Ridsdale, M. Naji, P. K. Stys, and H. Anis, "Coherent anti-Stokes Raman scattering microscopy using photonic crystal fiber with two closely lying zero dispersion wavelengths," Opt. Express **15**, 14028-14037 (2007).
71. M. Okuno, H. Kano, P. Leproux, V. Couderc, and H. O. Hamaguchi, "Ultrabroadband (>2000 cm^{-1}) multiplex coherent anti-Stokes Raman scattering

spectroscopy using a subnanosecond supercontinuum light source," Opt. Lett. **32**, 3050-3052 (2007).
72. K. B. Shi, P. Li, and Z. W. Liu, "Broadband coherent anti-Stokes Raman scattering spectroscopy in supercontinuum optical trap," Appl. Phys. Lett. **90**, (2007).
73. M. Okuno, H. Kano, P. Leproux, V. Couderc, and H. O. Hamaguchi, "Ultrabroadband multiplex CARS microspectroscopy and imaging using a subnanosecond supercontinuum light source in the deep near infrared," Opt. Lett. **33**, 923-925 (2008).
74. K. Tada and N. Karasawa, "Broadband Coherent Anti-Stokes Raman Scattering Spectroscopy Using Pulse-Shaper-Controlled Variable-Wavelength Soliton Pulses from a Photonic Crystal Fiber," Jpn. J. Appl. Phys. **47**, 8825-8828 (2008).
75. A. F. Pegoraro, A. Ridsdale, D. J. Moffatt, Y. Jia, J. P. Pezacki, and A. Stolow, "Optimally chirped multimodal CARS microscopy based on a single Ti:sapphire oscillator," Opt. Express **17**, 2984-2996 (2009).
76. K. Tada and N. Karasawa, "Broadband coherent anti-Stokes Raman scattering spectroscopy using soliton pulse trains from a photonic crystal fiber," Opt. Commun. **282**, 3948-3952 (2009).
77. G. W. Wurpel, H. A. Rinia, and M. Muller, "Imaging orientational order and lipid density in multilamellar vesicles with multiplex CARS microscopy," J. Microsc. **218**, 37-45 (2005).
78. G. W. Wurpel, J. M. Schins, and M. Muller, "Chemical specificity in three-dimensional imaging with multiplex coherent anti-Stokes Raman scattering microscopy," Opt. Lett. **27**, 1093-1095 (2002).
79. E. M. Vartiainen, H. A. Rinia, M. Muller, and M. Bonn, "Direct extraction of Raman line-shapes from congested CARS spectra," Opt. Express **14**, 3622-3630 (2006).
80. H. A. Rinia, M. Bonn, M. Muller, and E. M. Vartiainen, "Quantitative CARS spectroscopy using the maximum entropy method: The main lipid phase transition," Chemphyschem **8**, 279-287 (2007).
81. M. D. Duncan, J. Reintjes, and T. J. Manuccia, "Imaging biological compounds using the coherent anti-Stokes Raman scattering microscope," Opt. Eng. **24**, 4 (1985).
82. I. W. Schie, T. Weeks, G. P. McNerney, S. Fore, J. K. Sampson, S. Wachsmann-Hogiu, J. C. Rutledge, and T. Huser, "Simultaneous forward and epi-CARS microscopy with a single detector by time-correlated single photon counting," Opt. Express **16**, 2168-2175 (2008).
83. A. Y. Chikishev, G. W. Lucassen, N. I. Koroteev, C. Otto, and J. Greve, "Polarization sensitive coherent anti-Stokes Raman scattering spectroscopy of the amide I band of proteins in solutions," Biophys. J. **63**, 976-985 (1992).
84. A. Y. Chikishev, N. I. Koroteev, C. Otto, and J. Greve, "Polarization-sensitive CARS of the amide I band of pure and liganded chymotrypsin," J. Raman Spectrosc. **27**, 893-896 (1996).

85. A. Pott, T. Doerk, J. Uhlenbusch, J. Ehlbeck, J. Hoschele, and J. Steinwandel, "Polarization-sensitive coherent anti-Stokes Raman scattering applied to the detection of NO in a microwave discharge for reduction of NO," J. Phys. D **31**, 2485-2498 (1998).
86. M. Nissum, J. M. Funk, and W. Kiefer, "Polarization-sensitive resonance CARS spectroscopy of magnesium octaethylporphine," J. Raman Spectrosc. **30**, 605-610 (1999).
87. Y. Saito, T. Ishibashi, and H. Hamaguchi, "Polarization-resolved coherent anti-Stokes Raman scattering (CARS) spectroscopy: a new probe of molecular symmetry through accurate determination of the Raman depolarization ratio," J. Raman Spectrosc. **31**, 725-730 (2000).
88. P. P. Aung, K. M. Cosert, L. R. Weisel, T. F. Schulz, M. W. Gealy, and D. J. Ulness, "Effects of beam polarization on coherent anti-Stokes Raman scattering using noisy light," J. Raman Spectrosc. **36**, 409-419 (2005).
89. L. R. Weisel, T. Ta, E. C. Booth, and D. J. Ulness, "Polarization coherent anti-stokes Raman scattering using noisy light," J. Raman Spectrosc. **38**, 11-20 (2007).
90. J. Koster and S. Schlucker, "Polarization-sensitive CARS spectroscopy on free-base porphyrins: coproporphyrin I tetramethyl ester," J. Raman Spectrosc. **39**, 942-952 (2008).
91. J. M. Funk and A. Materny, "Analysis of the third-order susceptibilities of triplet excited molecules using nanosecond time-resolved resonance CARS," J. Raman Spectrosc. **29**, 1071-1078 (1998).
92. M. Schenk, A. Thumann, T. Seeger, and A. Leipertz, "Pure rotational coherent anti-Stokes Raman scattering: comparison of evaluation techniques for determining single-shot simultaneous temperature and relative N2 O2 concentration," Appl. Opt. **37**, 5659-5671 (1998).
93. M. Karavitis, R. Zadoyan, and V. A. Apkarian, "Time resolved coherent anti-Stokes Raman scattering of I-2 isolated in matrix argon: Vibrational dynamics on the ground electronic state," J. Chem. Phys. **114**, 4131-4140 (2001).
94. A. Volkmer, L. D. Book, and X. S. Xie, "Time-resolved coherent anti-Stokes Raman scattering microscopy: Imaging based on Raman free induction decay," Appl. Phys. Lett. **80**, 1505-1507 (2002).
95. J. M. Funk, C. Eichhorn, W. Kiefer, and A. Materny, "Nanosecond time-resolved resonance CARS spectroscopy of triplet excited polycyclic aromatic compounds," Spectrosc. Lett. **36**, 1-23 (2003).
96. T. Kiviniemi, J. Aumanen, P. Myllyperkio, V. A. Apkarian, and M. Pettersson, "Time-resolved coherent anti-Stokes Raman-scattering measurements of I-2 in solid Kr: Vibrational dephasing on the ground electronic state at 2.6-32 K," J. Chem. Phys. **123**, (2005).
97. S. Roy, T. R. Meyer, and J. R. Gord, "Time-resolved dynamics of resonant and nonresonant broadband picosecond coherent anti-Stokes Raman scattering signals," Appl. Phys. Lett. **87**, (2005).

98. M. Schenk, T. Seeger, and A. Leipertz, "Time-resolved CO_2 thermometry for pressures as great as 5 MPa by use of pure rotational coherent anti-Stokes Raman scattering," Appl. Opt. **44**, 6526-6536 (2005).
99. S. Oguchi, A. Matsuda, K. Kondo, and K. G. Nakamura, "Time-resolved coherent anti-Stokes Raman scattering of cyclohexane under shock compression," Jpn. J. Appl. Phys., Part 1 **45**, 5817-5820 (2006).
100. D. A. Sidorov-Biryukov, E. E. Serebryannikov, and A. M. Zheltikov, "Time-resolved coherent anti-Stokes Raman scattering with a femtosecond soliton output of a photonic-crystal fiber," Opt. Lett. **31**, 2323-2325 (2006).
101. B. von Vacano and M. Motzkus, "Time-resolved two color single-beam CARS employing supercontinuum and femtosecond pulse shaping," Opt. Commun. **264**, 488-493 (2006).
102. S. Postma, A. C. van Rhijn, J. P. Korterik, P. Gross, J. L. Herek, and H. L. Offerhaus, "Application of spectral phase shaping to high resolution CARS spectroscopy," Opt. Express **16**, 7985-7996 (2008).
103. A. C. W. van Rhijn, S. Postma, J. P. Korterik, J. L. Herek, and H. L. Offerhaus, "Chemically selective imaging by spectral phase shaping for broadband CARS around 3000 cm^{-1}," J. Opt. Soc. Am B **26**, 559-563 (2009).
104. V. V. Krishnamachari and E. O. Potma, "Imaging chemical interfaces perpendicular to the optical axis with focus-engineered coherent anti-Stokes Raman scattering microscopy," Chem. Phys. **341**, 81-88 (2007).
105. V. V. Krishnamachari and E. O. Potma, "Focus-engineered coherent anti-Stokes Raman scattering microscopy: a numerical investigation," J. Opt. Soc. Am A **24**, 1138-1147 (2007).
106. C. Vinegoni, J. Bredfeldt, D. Marks, and S. Boppart, "Nonlinear optical contrast enhancement for optical coherence tomography," Opt. Express **12**, 331-341 (2004).
107. E. O. Potma, C. L. Evans, and X. S. Xie, "Heterodyne coherent anti-Stokes Raman scattering (CARS) imaging," Opt. Lett. **31**, 241-243 (2006).
108. A. Nikolaenko, V. V. Krishnamachari, and E. O. Potma, "Interferometric switching of coherent anti-Stokes Raman scattering signals in microscopy," Phys. Rev. A **79**, (2009).
109. D. L. Marks, C. Vinegoni, J. S. Bredfeldt, and S. A. Boppart, "Interferometric differentiation between resonant coherent anti-Stokes Raman scattering and nonresonant four-wave-mixing processes," Appl. Phys. Lett. **85**, 5787-5789 (2004).
110. D. L. Marks and S. A. Boppart, "Nonlinear interferometric vibrational imaging," Phys. Rev. Lett. **92**, 123905 (2004).
111. E. S. Lee, J. Y. Lee, and Y. S. Yoo, "Nonlinear optical interference of two successive coherent anti-Stokes Raman scattering signals for biological imaging applications," J. Biomed. Opt. **12**, (2007).
112. M. Cui, M. Joffre, J. Skodack, and J. P. Ogilvie, "Interferometric Fourier transform coherent anti-Stokes Raman scattering," Opt. Express **14**, 8448-8458 (2006).

113. I. Toytman, K. Cohn, T. Smith, D. Simanovskii, and D. Palanker, "Wide-field coherent anti-Stokes Raman scattering microscopy with non-phase-matching illumination," Opt. Lett. **32**, 1941-1943 (2007).
114. C. Heinrich, S. Bernet, and M. Ritsch-Marte, "Wide-field coherent anti-Stokes Raman scattering microscopy," Appl. Phys. Lett. **84**, 816-818 (2004).
115. X. Nan, J. X. Cheng, and X. S. Xie, "Vibrational imaging of lipid droplets in live fibroblast cells with coherent anti-Stokes Raman scattering microscopy," J. Lipid Res. **44**, 2202-2208 (2003).
116. C. L. Evans, E. O. Potma, and X. S. Xie, "Coherent anti-stokes raman scattering spectral interferometry: determination of the real and imaginary components of nonlinear susceptibility chi(3) for vibrational microscopy," Opt. Lett. **29**, 2923-2925 (2004).
117. C. Heinrich, A. Hofer, A. Ritsch, C. Ciardi, S. Bernet, and M. Ritsch-Marte, "Selective imaging of saturated and unsaturated lipids by wide-field CARS microscopy," Opt. Express **16**, 2699-2708 (2008).
118. D. Pestov, M. H. Zhi, Z. E. Sariyanni, N. G. Kalugin, A. Kolomenskii, R. Murawski, Y. V. Rostovtsev, V. A. Sautenkov, A. V. Sokolov, and M. O. Scully, "Femtosecond CARS of methanol-water mixtures," J. Raman Spectrosc. **37**, 392-396 (2006).
119. E. Potma, W. P. de Boeij, P. J. van Haastert, and D. A. Wiersma, "Real-time visualization of intracellular hydrodynamics in single living cells," Proc. Natl. Acad. Sci. U. S. A. **98**, 1577-1582 (2001).
120. J. X. Cheng, S. Pautot, D. A. Weitz, and X. S. Xie, "Ordering of water molecules between phospholipid bilayers visualized by coherent anti-Stokes Raman scattering microscopy," Proc. Natl. Acad. Sci. U. S. A. **100**, 9826-9830 (2003).
121. X. Nan, E. O. Potma, and X. S. Xie, "Nonperturbative chemical imaging of organelle transport in living cells with coherent anti-stokes Raman scattering microscopy," Biophys. J. **91**, 728-735 (2006).
122. F. Lu, W. Zheng, and Z. Huang, "Elliptically polarized coherent anti-Stokes Raman scattering microscopy," Opt. Lett. **33**, 2842-2844 (2008).
123. H. A. Rinia, K. N. Burger, M. Bonn, and M. Muller, "Quantitative label-free imaging of lipid composition and packing of individual cellular lipid droplets using multiplex CARS microscopy," Biophys. J. **95**, 4908-4914 (2008).
124. I. Robinson, M. A. Ochsenkuhn, C. J. Campbell, G. Giraud, W. J. Hossack, J. Arlt, and J. Crain, "Intracellular imaging of host-pathogen interactions using combined CARS and two-photon fluorescence microscopies," J. Biophoton. (2009).
125. D. C. Kennedy, R. K. Lyn, and J. P. Pezacki, "Cellular lipid metabolism is influenced by the coordination environment of copper," J. Am. Chem. Soc. **131**, 2444-2445 (2009).
126. X. S. Xie, J. Yu, and W. Y. Yang, "Living cells as test tubes," Science **312**, 228-230 (2006).

127. M. Hirata, S. M. Akbar, N. Horiike, and M. Onji, "Noninvasive diagnosis of the degree of hepatic fibrosis using ultrasonography in patients with chronic liver disease due to hepatitis C virus," Eur. J. Clin. Invest. **31**, 528-535 (2001).
128. S. O. Konorov, C. H. Glover, J. M. Piret, J. Bryan, H. G. Schulze, M. W. Blades, and R. F. Turner, "In situ analysis of living embryonic stem cells by coherent anti-stokes Raman microscopy," Anal. Chem. **79**, 7221-7225 (2007).
129. S. Murugkar, C. L. Evans, X. S. Xie, and H. Anis, "Chemically specific imaging of cryptosporidium oocysts using coherent anti-Stokes Raman scattering (CARS) microscopy," J. Microsc. **233**, 244-250 (2009).
130. Y. Fu, T. B. Huff, H. W. Wang, H. Wang, and J. X. Cheng, "Ex vivo and in vivo imaging of myelin fibers in mouse brain by coherent anti-Stokes Raman scattering microscopy," Opt. Express **16**, 19396-19409 (2008).
131. Y. Fu, W. Sun, Y. Shi, R. Shi, and J. X. Cheng, "Glutamate excitotoxicity inflicts paranodal myelin splitting and retraction," PLoS One **4**, e6705 (2009).
132. Y. Fu, T. M. Talavage, and J. X. Cheng, "New imaging techniques in the diagnosis of multiple sclerosis," Expert. Opin. Med. Diagn. **2**, 1055-1065 (2008).
133. Y. Fu, H. Wang, T. B. Huff, R. Shi, and J. X. Cheng, "Coherent anti-Stokes Raman scattering imaging of myelin degradation reveals a calcium-dependent pathway in lyso-PtdCho-induced demyelination," J. Neurosci. Res. **85**, 2870-2881 (2007).
134. Y. Fu, H. Wang, R. Shi, and J. X. Cheng, "Second harmonic and sum frequency generation imaging of fibrous astroglial filaments in ex vivo spinal tissues," Biophys. J. **92**, 3251-3259 (2007).
135. Y. Fu, H. F. Wang, R. Y. Shi, and J. X. Cheng, "Noninvasive molecular imaging of intact myelin sheath by coherent anti-stokes raman scattering microscopy," Am. Lab. **39**, 12-14 (2007).
136. F. P. Henry, D. Cote, M. A. Randolph, E. A. Rust, R. W. Redmond, I. E. Kochevar, C. P. Lin, and J. M. Winograd, "Real-time in vivo assessment of the nerve microenvironment with coherent anti-Stokes Raman scattering microscopy," Plast. Reconstr. Surg. **123**, 123S-130S (2009).
137. T. B. Huff and J. X. Cheng, "In vivo coherent anti-Stokes Raman scattering imaging of sciatic nerve tissue," J. Microsc. **225**, 175-182 (2007).
138. A. P. Kennedy, J. Sutcliffe, and J. X. Cheng, "Molecular composition and orientation in myelin figures characterized by coherent anti-stokes Raman scattering microscopy," Langmuir **21**, 6478-6486 (2005).
139. H. Wang, Y. Fu, P. Zickmund, R. Shi, and J. X. Cheng, "Coherent anti-stokes Raman scattering imaging of axonal myelin in live spinal tissues," Biophys. J. **89**, 581-591 (2005).
140. H. Chen, H. Wang, M. N. Slipchenko, Y. Jung, Y. Shi, J. Zhu, K. K. Buhman, and J. X. Cheng, "A multimodal platform for nonlinear optical microscopy and microspectroscopy," Opt. Express **17**, 1282-1290 (2009).
141. T. Hellerer, C. Axang, C. Brackmann, P. Hillertz, M. Pilon, and A. Enejder, "Monitoring of lipid storage in Caenorhabditis elegans using coherent

anti-Stokes Raman scattering (CARS) microscopy," Proc. Natl. Acad. Sci. U. S. A. **104**, 14658-14663 (2007).
142. T. T. Le, H. M. Duren, M. N. Slipchenko, C. D. Hu, and J. X. Cheng, "Label-free quantitative analysis of lipid metabolism in living caenorhabditis elegans," J. Lipid Res. (2009).
143. Y. M. Wu, H. C. Chen, W. T. Chang, J. W. Jhan, H. L. Lin, and I. Liau, "Quantitative Assessment of Hepatic Fat of Intact Liver Tissues with Coherent Anti-Stokes Raman Scattering Microscopy," Anal. Chem. **81**, 1496-1504 (2009).
144. M. Zimmerley, C. Y. Lin, D. C. Oertel, J. M. Marsh, J. L. Ward, and E. O. Potma, "Quantitative detection of chemical compounds in human hair with coherent anti-Stokes Raman scattering microscopy," J. Biomed. Opt. **14**, 044019 (2009).
145. M. Windbergs, M. Jurna, H. L. Offerhaus, J. L. Herek, P. Kleinebudde, and C. J. Strachan, "Chemical Imaging of Oral Solid Dosage Forms and Changes upon Dissolution Using Coherent Anti-Stokes Raman Scattering Microscopy," Anal. Chem. **81**, 2085-2091 (2009).
146. A. Dogariu, A. Goltsov, and M. O. Scully, "Real-time monitoring of blood using coherent anti-Stokes Raman spectroscopy," J. Biomed. Opt. **13**, 054004 (2008).
147. C. L. Evans, X. Xu, S. Kesari, X. S. Xie, S. T. Wong, and G. S. Young, "Chemically-selective imaging of brain structures with CARS microscopy," Opt. Express **15**, 12076-12087 (2007).
148. T. T. Le, T. B. Huff, and J. X. Cheng, "Coherent anti-Stokes Raman scattering imaging of lipids in cancer metastasis," BMC Cancer **9**, (2009).
149. P. Xu, E. Gullotti, L. Tong, C. B. Highley, D. R. Errabelli, T. Hasan, J. X. Cheng, D. S. Kohane, and Y. Yeo, "Intracellular drug delivery by poly(lactic-co-glycolic acid) nanoparticles, revisited," Mol. Pharmacol. **6**, 190-201 (2009).
150. E. Kang, H. Wang, I. K. Kwon, J. Robinson, K. Park, and J. X. Cheng, "In situ visualization of paclitaxel distribution and release by coherent anti-Stokes Raman scattering microscopy," Anal. Chem. **78**, 8036-8043 (2006).
151. E. Kang, H. Wang, I. K. Kwon, Y. H. Song, K. Kamath, K. M. Miller, J. Barry, J. X. Cheng, and K. Park, "Application of coherent anti-Stokes Raman scattering microscopy to image the changes in a paclitaxel-poly(styrene-b-isobutylene-b-styrene) matrix pre- and post-drug elution," J. Biomed. Mater. Res. A **87A**, 913-920 (2008).
152. J. Moger, B. D. Johnston, and C. R. Tyler, "Imaging metal oxide nanoparticles in biological structures with CARS microscopy," Opt. Express **16**, 3408-3419 (2008).
153. Y. Jung, H. Chen, L. Tong, and J. X. Cheng, "Imaging Gold Nanorods by Plasmon-Resonance-Enhanced Four Wave Mixing," J. Phys. Chem. C **113**, 2657-2663 (2009).

154. I. Baltog, M. Baibarac, and S. Lefrant, "Coherent anti-Stokes Raman scattering on single-walled carbon nanotube thin films excited through surface plasmons," Phys. Rev. B **72**, 12 (2005).
155. I. Baltog, M. Baibarac, and S. Lefrant, "Coherent anti-Stokes Raman scattering on single-walled carbon nanotubes and copper phthalocyanine thin films excited through surface plasmons," J. Opt. A **7**, 632-639 (2005).
156. I. Baltog, M. Baibarac, L. Mihut, and S. Lefrant, "Abnormal anti-Stokes Raman spectra of single walled carbon nanotubes raised from coherent anti-Stokes Raman scattering and optical cooling processes," Dig. J. Nanomater. Biostruct. **2**, 185-198 (2007).
157. S. Lefrant, J. P. Buisson, J. Y. Mevellec, L. Baltog, and M. Baibarac, "Single-beam pumped coherent anti-Stokes Raman scattering on carbon nanotubes," Phys. Status Solidi B **245**, 2221-2224 (2008).
158. H. Wang, T. B. Huff, Y. Fu, K. Y. Jia, and J. X. Cheng, "Increasing the imaging depth of coherent anti-Stokes Raman scattering microscopy with a miniature microscope objective," Opt. Lett. **32**, 2212-2214 (2007).
159. M. Zimmerley, R. A. McClure, B. Choi, and E. O. Potma, "Following dimethyl sulfoxide skin optical clearing dynamics with quantitative nonlinear multimodal microscopy," Appl. Opt. **48**, D79-87 (2009).
160. H. W. Wang, T. T. Le, and J. X. Cheng, "Label-free imaging of arterial cells and extracellular matrix using a multimodal CARS microscope," Opt. Commun. **281**, 1813-1822 (2008).
161. T. T. Le, I. M. Langohr, M. J. Locker, M. Sturek, and J. X. Cheng, "Label-free molecular imaging of atherosclerotic lesions using multimodal nonlinear optical microscopy," J. Biomed. Opt. **12**, 054007 (2007).
162. H. W. Wang, I. M. Langohr, M. Sturek, and J. X. Cheng, "Imaging and Quantitative Analysis of Atherosclerotic Lesions by CARS-Based Multimodal Nonlinear Optical Microscopy," Atertio. Thromb. Vasc. Biol. **29**, 1342-1348 (2009).
163. J. Mansfield, J. Yu, D. Attenburrow, J. Moger, U. Tirlapur, J. Urban, Z. Cui, and P. Winlove, "The elastin network: its relationship with collagen and cells in articular cartilage as visualized by multiphoton microscopy," J. Anat. 10 (2009).
164. C. P. Pfeffer, B. R. Olsen, F. Ganikhanov, and F. Legare, "Multimodal nonlinear optical imaging of collagen arrays," J. Struct. Biol. **164**, 140-145 (2008).
165. Z. Knittl, *Optics of thin films* (Wiley, London, 1976).
166. E. Frumker, D. Oron, D. Mandelik, and Y. Silberberg, "Femtosecond pulse-shape modulation at kilohertz rates," Opt. Lett. **29**, 890-892 (2004).
167. B. A. Neuschwander-Tetri, "Nonalcoholic steatohepatitis," Clin. Liver Dis. **2**, 149-173 (1998).
168. N. Assy, K. Kaita, D. Mymin, C. Levy, B. Rosser, and G. Minuk, "Fatty infiltration of liver in hyperlipidemic patients," Dig. Dis. Sci. **45**, 1929-1934 (2000).

169. J. M. Clark, F. L. Brancati, and A. M. Diehl, "Nonalcoholic fatty liver disease," Gastroenterol. **122**, 1649-1657 (2002).
170. S. A. Harrison and B. A. Neuschwander-Tetri, "Nonalcoholic fatty liver disease and nonalcoholic steatohepatitis," Clin. Liver Dis. **8**, 19 (2004).
171. G. Bedogni, S. Bellentani, L. Miglioli, F. Masutti, M. Passalacqua, A. Castiglione, and C. Tiribelli, "The Fatty Liver Index: a simple and accurate predictor of hepatic steatosis in the general population," BMC Gastroenterol. **6**, 33 (2006).
172. G. Marchesini and M. Babini, "Nonalcoholic fatty liver disease and the metabolic syndrome," Minerva Cardioangiol. **54**, 229-239 (2006).
173. E. Bjornsson and P. Angulo, "Non-alcoholic fatty liver disease," Scand. J. Gastroenterol. **42**, 1023-1030 (2007).
174. B. A. Neuschwander-Tetri, "Fatty liver and the metabolic syndrome," Curr. Opin. Gastroenterol. **23**, 193-198 (2007).
175. N. H. Afdhal and D. Nunes, "Evaluation of liver fibrosis: a concise review," Am. J. Gastroenterol. **99**, 1160-1174 (2004).
176. S. L. Friedman, "Liver fibrosis -- from bench to bedside," J. Hepatol. **38 Suppl 1**, S38-53 (2003).
177. R. Bataller and D. A. Brenner, "Liver fibrosis," J. Clin. Invest. **115**, 209-218 (2005).
178. J. McHutchison, T. Poynard, and N. Afdhal, "Fibrosis as an end point for clinical trials in liver disease: a report of the international fibrosis group," Clinical Gastroenterology and Hepatology **4**, 1214-1220 (2006).
179. J. Jiao, S. L. Friedman, and C. Aloman, "Hepatic fibrosis," Curr. Opin. Gastroenterol. **25**, 223-229 (2009).
180. A. Wieckowska and A. E. Feldstein, "Diagnosis of nonalcoholic fatty liver disease: invasive versus noninvasive," Semin. Liver Dis. **28**, 386-395 (2008).
181. P. Mishra and Z. M. Younossi, "Abdominal ultrasound for diagnosis of nonalcoholic fatty liver disease (NAFLD)," Am. J. Gastroenterol. **102**, 2716-2717 (2007).
182. A. Wieckowska, A. J. McCullough, and A. E. Feldstein, "Noninvasive diagnosis and monitoring of nonalcoholic steatohepatitis: present and future," Hepatology **46**, 582-589 (2007).
183. G. J. Cheng, F. Shan, A. Freyer, and T. Guo, "Compact 50-Hz terawatt Ti : sapphire laser for x-ray and nonlinear optical spectroscopy," Appl. Opt. **41**, 5148-5154 (2002).
184. F. Lu, W. Zheng, and Z. W. Huang, "Phase-controlled polarization coherent anti-Stokes Raman scattering microscopy for high-sensitivity and high-contrast molecular imaging," J. Opt. Soc. Am B **25**, 1907-1913 (2008).
185. H. F. Wang, L. P. Shi, B. Lukyanchuk, C. Sheppard, and C. T. Chong, "Creation of a needle of longitudinally polarized light in vacuum using binary optics," Nat. Photon. **2**, 501-505 (2008).

186. L. Novotny, M. R. Beversluis, K. S. Youngworth, and T. G. Brown, "Longitudinal field modes probed by single molecules," Phys. Rev. Lett. **86**, 5251-5254 (2001).
187. E. Y. S. Yew and C. J. R. Sheppard, "Second harmonic generation polarization microscopy with tightly focused linearly and radially polarized beams," Opt. Commun. **275**, 453-457 (2007).
188. S. Y. Yang and Q. W. Zhan, "Third-harmonic generation microscopy with tightly focused radial polarization," J. Opt. **10**, (2008).
189. J. Lin, H. F. Wang, W. Zheng, F. Lu, C. Sheppard, and Z. W. Huang, "Numerical study of effects of light polarization, scatterer sizes and orientations on near-field coherent anti-Stokes Raman scattering microscopy," Opt. Express **17**, 2423-2434 (2009).
190. R. J. Luebbers and J. Beggs, "FDTD calculation of wide-band antenna gain and efficiency," IEEE Trans. Antennas. Propag. **40**, 1403-1407 (1992).
191. K. S. Youngworth and T. G. Brown, "Focusing of high numerical aperture cylindrical-vector beams," Opt. Express **7**, 77-87 (2000).
192. J. Lin, F. Lu, H. Wang, W. Zheng, C. J. Sheppard, and Z. Huang, "Improved contrast radially polarized coherent anti-Stokes Raman scattering microscopy using annular aperture detection," Appl. Phys. Lett. **95**, 133703 (2009).
193. M. Stalder and M. Schadt, "Linearly polarized light with axial symmetry generated by liquid-crystal polarization converters," Opt. Lett. **21**, 1948-1950 (1996).
194. B. H. Jia, X. S. Gan, and M. Gu, "Direct measurement of a radially polarized focused evanescent field facilitated by a single LCD," Opt. Express **13**, 6821-6827 (2005).
195. D. W. McCamant, P. Kukura, S. Yoon, and R. A. Mathies, "Femtosecond broadband stimulated Raman spectroscopy: Apparatus and methods," Rev. Sci. Instrum. **75**, 4971-4980 (2004).
196. H. Miyoshi, C. Rust, P. J. Roberts, L. J. Burgart, and G. J. Gores, "Hepatocyte apoptosis after bile duct ligation in the mouse involves Fas," Gastroenterol. **117**, 669-677 (1999).
197. C. Weiler-Normann, J. Herkel, and A. W. Lohse, "Mouse models of liver fibrosis," Z. Gastroenterol. **45**, 43-50 (2007).
198. W. Sun, S. Chang, D. C. Tai, N. Tan, G. Xiao, H. Tang, and H. Yu, "Nonlinear optical microscopy: use of second harmonic generation and two-photon microscopy for automated quantitative liver fibrosis studies," J. Biomed. Opt. **13**, 064010 (2008).
199. E. Brown, T. McKee, E. diTomaso, A. Pluen, B. Seed, Y. Boucher, and R. K. Jain, "Dynamic imaging of collagen and its modulation in tumors in vivo using second-harmonic generation," Nat. Med. **9**, 796-800 (2003).
200. P. Nandakumar, A. Kovalev, and A. Volkmer, "Vibrational imaging based on stimulated Raman scattering microscopy," New J. Phys. **11**, (2009).
201. C. W. Freudiger, W. Min, B. G. Saar, S. Lu, G. R. Holtom, C. W. He, J. C. Tsai, J. X. Kang, and X. S. Xie, "Label-Free Biomedical Imaging with High

Sensitivity by Stimulated Raman Scattering Microscopy," Science **322**, 1857-1861 (2008).

202. F. Legare, C. L. Evans, F. Ganikhanov, and X. S. Xie, "Towards CARS endoscopy," Opt. Express **14**, 4427-4432 (2006).